UNIVERSIDAD NACIONAL AUTONOMA

DE MEXICO

FACULTAD DE CIENCIAS

DIVISION DE ESTUDIOS DE POSGRADO

MICROESTRUCTURAS Y EYECCIONES COLIMADAS EN NEBULOSAS FOTOIONIZADAS

T E S I S

QUE PARA OBTENER EL GRADO ACADEMICO DE

DOCTOR EN CIENCIAS (ASTRONOMIA)

PRESENTA

LUIS LOPEZ MARTIN

POSGRADO EN CIENCIAS
(ASTRONOMIA)

DIRECTOR DE TESIS : DR. ALEJANDRO C. RAGA RASMUSSEN

2000

Microestructuras y Eyecciones Colimadas en Nebulosas Fotoionizadas

Luis López Martín

Índice General

Lista de figuras

Índice de Tablas

AGRADECIMIENTOS

En primer lugar, quiero agradecerle a mi director de tesis, Alejandro Raga, por haber dirigido este trabajo; por su apoyo incondicional en todo momento, tanto profesional como personal; por haberme introducido en el mundo de las simulaciones cuando yo me creía un observador nato; por darme aliento en los momentos más difíciles; por creer en mi capacidad más que yo mismo; por ayudarme a que este proyecto saliera y por ser mi amigo.

A Silvia Torres, por haber creído en mí; por asesorarme durante mi maestría; por haberme hecho conocer el maravilloso mundo de las nebulosas planetarias; por todo su apoyo y por ayudarme a entender que "la vida es dura"....

Al Instituto de Astronomía de la UNAM por darme la oprtunidad de "reencontrarme" con la astronomía y por ser un lugar tan agradable donde hacer mi posgrado. A DGEP por haberme apoyado con la beca para mi doctorado, y al SNI y algunos proyectos de CONACyT que me ayudaron a sobrevivir durante mi maestría.

A mi comité asesor: Alejandro Raga, Salvador Curiel, Miriam Peña y Margarita Rosado por haberme apoyado semestre tras semestre y confiar en mi trabajo. A los sinodales : José Franco, José Alberto López, Susana Lizano, Alejandro Raga, Yolanda Gómez, Salvador Curiel y ,Wolfgang Steffen, por su paciencia conmigo y sus amables y acertados comentarios.

A Beto López y Roberto Vázquez por ayudarme en este trabajo de tesis, por haber compartido conmigo su extenso conocimiento sobre la morfología de las nebulosas planetarias, y por todo el apoyo brindado en mis estancias en el Instituto de Astronomía en Ensenada. A Luis Felipe Miranda por haberme motivado para seguir en esto de la astronomía cuando estudiaba mi carrera en Madrid y por su valiosa ayuda en el trabajo de tesis.

A Lorena Arias por haber compartido conmigo casi todas mis temporadas de observación en San Pedro Mártir y por haberme enseñado tantas cosas sobre el funcionamiento del telescopio y sus instrumentos (los del telescopio..). Siempre recordaré el : *"tu no te preocupes..."*

A todos mis compañeros del Instituto de Astronomía por haberme hecho sentir en familia estando tan lejos de mi casa; por soportar mis neuras y constantes cambios de

humor; por acompañarme en las fiestas y tratar de seguirme el paso con mi música de aerobics.

A Puri, por ser tan especial y haber compartido conmigo tantos momentos maravillosos; por "arrastrarme" a hacer la especialidad de astrofísica cuando estaba a punto de desertar, por haberme enseñado tantas cosas de la vida y sobre todo por haber estado siempre a mi lado. Gracias.

A todo el personal del telescopio en San Pedro Mártir, por su apoyo en las temporadas de observación, sus buenos consejos y su cálida compañía.

A la gente del Instituto de Astronomía de Ensenada por todo el apoyo brindado en mis "intensas y productivas" visitas; por darme acceso a todos los recursos necesarios (sobre todo el Century..... ya saben que no conduzco "standards"..) y por esas carnes asadas que tanto se extrañan en el D.F.

A la gente del Instituto de Astronomía de Morelia por la amabilidad con la que me han tratado en todo momento y por la estancia tan placentera y productiva que tuve el privilegio de gozar en el transcurso de mi tesis.

A todos los que en este momento se me olviden que seguramente serán muchos y sabrán disculpar la omisión.

A mis padres por haber aceptado, entendido y apoyado todas mis decisiones. Por haberme hecho como soy y quererme en todo momento. A mi hermana porque siempre me ha demostrado su amor y respeto.

A Carlos, por haberme acompañado en estos años y haber estado siempre a mi lado apoyándome y deleitandome con su maravillosa presencia.

RESUMEN

El presente trabajo ha sido enfocado a determinar y entender el origen y evolución de estructuras e inhomogeneidades que presentan las nebulosas fotoionizadas. Así mismo, se ha tratado de analizar, tanto desde el punto de vista teórico como a través de un estudio cinemático, el origen y evolución de eyecciones colimadas que observamos en nebulosas planetarias (NP, o PN por su acrónimo en inglés) y en objetos Herbig-Haro (HH) inmersos en regiones HII. Los resultados principales de este trabajo son los siguientes :

(a) Se discute el origen de la emisión de los glóbulos neutros que se observan en la nebulosa planetaria de la Hélice, los cuales son denominados comunmente en la literatura "nudos cometarios". Presentamos un modelo analítico de flujo fotoevaporado para estos glóbulos, tanto para sus "cabezas" como para sus "colas", que explica las estructuras observadas en imágenes ópticas de esta nebulosa planetaria. Con este modelo analítico podemos determinar algunos parámetros de la NP y el cociente entre el flujo ionizante de la estrella central y el flujo difuso nebular.

(b) Desarrollamos un modelo analítico para la descripción de la evolución del frente de ionización que atraviesa un chorro neutro eyectado por una estrella jóven que emerge dentro de un campo de radiación ionizante. Se analizan las características del paso de un frente de ionización tipo R y tipo D, así como sus implicaciones dinámicas en el chorro neutro y las propiedades que se espera poder observar.

(c) Se presentan observaciones espectroscópicas de rendija larga[1] de un objeto HH (HH 444, en la región de σ Orionis) embebido en una región fotoionizada. Se comparan los diagramas posición-velocidad observados con los predichos por modelos numéricos obtenidos con el código hidrodinámico "yguazú" (Raga et al. 1999). A través de estas comparaciones es posible inferir algunos parámetros de la eyección del material, y verificar que es posible reproducir las observaciones con modelos hidrodinámicos de chorros.

---

[1]Obtenidas en el telescopio de San Pedro Mártir con el Espectrómetro *echelle* de Manchester en el 2.1 m.

(d) Reportamos observaciones de imagen directa tomadas en los filtros Hα, [N II], [S II] y [O III] [2], en las que se detectan por primera vez estructuras de choques de proa, así como de unas condensaciones que parecen trazar arcos alrededor del nucleo bipolar de la nebulosa planetaria M 2-48.

(e) Presentamos un estudio cinemático detallado de las estructuras encontradas en la NP M 2-48 analizando los diagramas posición-velocidad que se obtienen mediante la espectroscopía de rendija larga[3]. A través de este análisis proponemos la existencia de un par de choques de proa simétricos (separados unos 4'), así como la presencia de un par de arcos en expansión lenta.

---

[2]Obtenidas en el telescopio de San Pedro Mártir con el PUMA en el modo de imagen directa en el 2.1 m.

[3]Obtenida en el telescopio de San Pedro Mártir con el Espectrómetro *echelle* de Manchester en el 2.1 m.

Parte I

Introducción

Capítulo 1

Estructuras en nebulosas fotoionizadas

1.1 Conceptos generales.

Las nebulosas fotoionizadas son una variedad de objetos astronómicos que están constituidos por una fuente central que posee un campo de radiación con fotones de energía suficiente para fotoionizar a la envolvente de gas que rodea la fuente. Dentro de la categoría de nebulosa fotoionizada encontramos dos tipos de objetos: las nebulosas planetarias (NP) y las regionies H II. En las nebulosas planetarias la fuente central es una estrella evolucionada de masa intermedia que expulsa e ioniza una envolvente de gas que se expande en el medio interestelar, mientras que en las regiones H II la fuente central ionizante es una estrella jóven y masiva (o un grupo de ellas) que ioniza una nube de gas circundante.

Nuestro conocimiento sobre la formación de nebulosas planetarias se ha visto modificado en los últimos años debido fundamentalmente a dos factores, por un lado el hecho de que la mayoría de las NP no presentan simetría esférica, y por otro, los flujos áltamente colimados que se observan cada vez en un número mayor de NP (Miranda & Solf 1992, López et al. 1995, López et al 1997, Bryce et al. 1997, O'Connor et al. 2000, Vázquez et al. 2000). Estos flujos llegan a alcanzar velocidades de expansión de varios cientos de km s^{-1} (López et al. 1995). Por otro lado, existen evidencias en algunos objetos de eyecciones múltiples y episódicas que nos hacen modificar nuestra concepción sobre la evolución de los objetos post-AGB. Estos objetos son estrellas que salieron de la secuencia principal y pasaron por la etapa de la rama asintótica de gigantes (AGB).

Las estrellas jóvenes, que nacen en núcleos de nubes moleculares densas, a menudo generan chorros altamente supersónicos y vientos que dan lugar a objetos Herbig-Haro

(HH). Estos son detectables en longitudes de onda ópticas, en líneas de emisión en el cercano y lejano infrarrojo de hidrógeno molecular, [Fe II] y [O I], y también en longitudes de onda de radio. Los objetos HH son identificados por su emisión en las líneas prohibidas de [S II], [O I], [C II], [C I] y por presentar cocientes altos de estas líneas respecto de Hα o Hβ (Solf, Böhm & Raga 1986, Böhm, Raga & Solf 1986) . A pesar de que se piensa que los objetos HH se forman en los primeros cientos de miles de años de la vida de los objetos estelares jóvenes (YSO), la mayoría de las fuentes están altamente obscurecidas por los núcleos de las nubes y ambientes circunestelares en los que se forman.

Los objetos HH son, en general, nebulosas excitadas colisionalmente, generados por flujos de material eyectado por YSO que trazan choques, ya sea por la interacción con el medio ambiente de la nube formando las llamadas *superficies de trabajo terminales,* o bien, por la interacción de material eyectado a diferentes velocidades formando las llamadas *superficies de trabajo internas.*

En algunas ocasiones encontramos objetos HH embebidos en regiones fotoionizadas (Reipurth et al. 1998, O'Dell et al. 2000), de manera que la emisión que observamos proviene por un lado de la ionización colisional producida en los choques, y por otro lado de la fotoionización debida al campo de radiación ionizante (López-Martín et al. 2000).

En este trabajo se estudian las condiciones físicas de algunas microestructuras y eyecciones colimadas en nebulosas fotoionizadas. Para este estudio se han utilizado en algunos casos modelos analíticos, en otros, se ha recurrido a cálculos numéricos utilizando el código hidrodinámico "yguazú" (Raga et al. 1999). En el caso de las eyecciones colimadas además se han hecho estudios comparativos con observaciones espectroscópicas de los objetos que se analizan en este trabajo.

La estructura del trabajo es la siguiente: En la seción 1.2 se describen las microestructuras que se observan en las nebulosas planetarias y se especula sobre los mecanismos posibles que las originan. Las eyecciones colimadas en nebulosas fotoionizadas son descritas en las secciones 1.3 y 1.4. Las eyecciones que se producen en el interior de las regiones H II por estrellas jóvenes de baja masa, embebidas en la region HII, tienen un interés especial, pués nos sitúan en unas condiciones sin precedentes para el estudio de la fotoionización del material neutro eyectado, permitiendo inferir propiedades de las condiciones de la eyección. El estudio de las eyecciones en nebulosas planetarias nos puede ayudar a entender con más detalle los procesos de eyección de la envolvente de la estrella central.

En el Capítulo 2 se discute acerca de la presencia de glóbulos neutros en la nebulosa de la Hélice y se analiza el origen de la emisión, tanto en las cabezas como en las colas de estos nudos cometarios. Presentamos un modelo analítico para las cabezas siguiendo el planteamiento de Cantó et al. 1998, en el que se propone que la fotoevaporación en la cabeza es debida a la incidencia del campo de radiación ionizante de la estrella central.

Para la cola cometaria, nosotros proponemos que el material neutro que queda en la sombra de esta radiación de la estrella central es ionizado por los fotones del campo difuso nebular. Utilizando las imágenes públicas de esta nebulosa del archivo del Hubble Space Telescope, aplicamos nuestro modelo a la emisión de estos nudos cometarios. Los resultados de este trabajo se encuentran en el artículo titulado "Photoevaporating flows from the cometary knots of the Helix nebula (NGC 7293)", que ha sido aceptado en Astrophysical Journal, y se espera aparezca en el número del 10 de febrero del 2001. Este trabajo se realizó en colaboración con Alejandro Raga, Will Henney, Garrelt Mellema y Jorge Cantó y constituye el Capítulo 3 de esta tesis. Se presenta el esquema teórico de la fotoionización de material neutro eyectado por una estrella jóven en presencia de un campo de radiación ionizante en el Capítulo 4. En el Capítulo 5 s Se presentan las expresiones analíticas que describen el paso del frente de ionización (FI) por el material neutro y se obtienen resultados numéricos de la posición de este FI y se comparan con las posiciones predichas por la teoría analítica. Además se discuten los efectos dinámicos del paso de un FI tipo R y tipo D. Este trabajo está desarrollado en el artículo titulado "The emergence of a neutral Herbig-Haro object into a photoionized nebula", que se construyó en colaboración de Alex Raga, Luc Binette, José Alberto López, Jorge Cantó, Jane Arthur, Garrelt Mellema, Wolfgang Steffen y Pierre Ferruit. El artículo fue publicado en la revista MNRAS (314, 681).

Una vez desarrollada la teoría de la fotoionización uno espera poder verificar las predicciones con observaciones. De esto se ocupa precisamente el Capítulo 6, en el que se presenta el análisis cinemático realizado para el objeto HH 444. Los detalles sobre este análisisis y la comparación con resultados numéricos están expuestos en el artículo titulado "The structure and kinematics of the HH 444 photoionized jet in the σ Orionis region", que está a punto de ser enviado a una revista con arbitraje internacional y que constituye el Capítulo 7de la tesis. En este artículo se ha colaborado con Alejandro Raga en la parte de las simulaciones numéricas, y con José Alberto López y John Meaburn, quienes realizaron las observaciones en el telescopio de 2.1 m de San Pedro Mártir, Baja Califronia, México, con el espectrómetro *echelle* de Manchester.

La descripción de las motivaciones que nos llevan a analizar las eyecciones colimadas en NP es presentado en el Capítulo 8, donde nos enfocamos al caso de la NP M 2-48. Las observaciones de este objeto las realizamos Lorena Arias y yo en el telescopio de 2.1 m de San Pedro Mártir, Baja Califronia, México, utilizando el PUMA en el modo de imagen directa. Estas observaciones muestran por primera vez estructuras externas al núcleo bipolar. Estas estructuras fueron reportadas en el artículo "Bow-shocks and possible Jet-shell interaction in the Planetary Nebula M 2-48", que fue publicado en la revista Astronomy and Astrophysics (357, 1031). Este artículo se presenta en el Capítulo 9 y contó con la colaboración de Roberto Vázquez, Luis Felipe Miranda, César Esteban, José María

Torrelles, Lorena Arias y Alejandro Raga. Dado el interés que despiertan las estructuras observadas en esta NP, se realizó un estudio cinemático del objeto. Una visión general de la estructura de la nebulosa se presenta en el capítulo 10. Las observaciones de espectroscopía de alta resolución de este objeto fueron llevadas a cabo por José Alberto López y John Meaburn en el telescopio de 2.1 m de San Pedro Mártir, Baja Califronia, México con el espectrómetro *echelle* de Manchester. También contamos con espectroscopía de baja resolución que fue tomada por Roberto Vázquez, Lorenzo Olguín y Roberto Cook. El análisis de la cinemática y de las propiedes físicas de la nebulosa está en proceso y sólamente contamos con resultados preeliminares, con los que estamos preparando un artículo para ser enviado a revista con arbitraje internacional. En este artículo están colaborando César Esteban, Roberto Vázquez, Alejandro Raga, José Alberto López, Luis Felipe Miranda, Jose María Torrelles, Loreznao Olguín y John Meaburn, y está presentado en el Capítulo 11. El Capítulo 12 resume los resultados obtenidos de este trabajo de análisis de estructuras en nebulosas fotoionizadas.

1.2 Microestructuras en nebulosas planetarias

La concepción de NP como una envolvente esférica en expansión isotrópica en un medio homogéneo ha quedado relegada a idealizaciones propuestas en los libros de texto. En los últimos años, el avance en las técnicas de observación ha dado un gran impulso al estudio de la morfología óptica de las NPs. Cada vez son más numerosas las imágenes de NPs en las que encontramos diferentes tipos de asimetrías, bipolaridades, envolventes múltiples y pequeñas estructuras con morfologías diversas (Vázquez et al. 2000, Balick et al. 1998, O'Dell et al. 1997, López et al. 1995, Balick et al. 1994, Miranda & Solf 1992). Algunas de estas microestructuras se han denominado FLIERs[1] (ver Figuras 1.1, 1.2 y 1.3) y se encuentra que tienen las siguientes caraterísticas:

a) bajo grado de ionización respecto al gas adyacente,

b) velocidades supersónicas relativas a la velocidad del sonido del gas que las rodea (unos 50 kms^{-1}, y hasta 500 km s^{-1} en el caso de los *ansae*),

c) en general, aparecen como pares cuyas velocidades son del mismo valor y signo opuesto respecto a la velocidad sistémica de la nebulosa,

d) menores edades cinemáticas que las capas de gas que los rodean, del orden de 10^3 años,

e) aparente intensificación de nitrógeno relativo al hidrógeno (en factores de 2 a 5),

f) masas típicas del orden de 10^{-4} a 10^{-5} $\text{M}_\odot$,

g) tamaños pequeños, en al menos una dimensión, del orden de 10^{15} a 10^{16} cm,

h) mucha mayor energía cinética que térmica.

No se ha encontrado hasta el momento un modelo simple que sea capaz de reproducir de forma natural todas estas propiedades observadas en los FLIERs. La distribución simétrica en las que los observamos y sus edades cinemáticas relativamente cortas, sugieren que los FLIERs sean fenómenos recientes.

Algunas de estas microestructuras a veces son marginalmente detectables o incluso indetectables en imágenes directas tomadas en los filtros Hα+[N II] y [O III]. Parecen ser más comunes en las NP elípticas (se han encontrado en aproximadamente la mitad de ellas). Corradi et al. (1996) proponen una técnica de división de imágenes para poder

---

[1]Fast Low-Ionization Emission Regions

FIGURA 1.1: Imagen de NGC 7662 tomada del archivo público del Space Telescope Science Institute, Baltimore, EE. UU. (HTTP://WWW.STSCI.EDU).

encontrar estas estructuras de baja ionización en nebulosas planetarias y otras regiones H II. Esta técnica tiene la característica de eliminar la mayoría de los efectos que son debidos a variaciones de densidad, mientras que es sensible a aquellos efectos debidos a cambios de ionización/excitación. Por otro lado las observaciones parecen sugerir que los FLIERs tienen densidades más altas que las del gas que los rodean, de manera que se hace necesario utilizar alguna técnica que nos elimine los efectos de la variación de la densidad en los cambios en la intensidad de las líneas. Podríamos dividir estas microestructuras morfológicamente en dos grandes grupos:

- **Nudos** : Los podemos encontrar en pares, en posiciones aproximadamente opuestas sobre la dirección radial, o también en grupos, con simetría puntual o sin ella; e incluso en condensaciones aisladas.

- **Estructuras** *como-chorros* : Son estructuras alargadas, delgadas y colimadas, con cocientes altos de su largo-ancho. Siempre las encontramos orientadas a lo largo de la dirección radial que apunta hacia la estrella central, y en general tienen una contraparte en el lado opuesto de la nebulosa.

Generalmente encontramos estas estructuras en las regiones menos brillantes de la nebulosa, como en las envolventes, halos, e incluso separados del cuerpo principal de la nebulosa. Esto
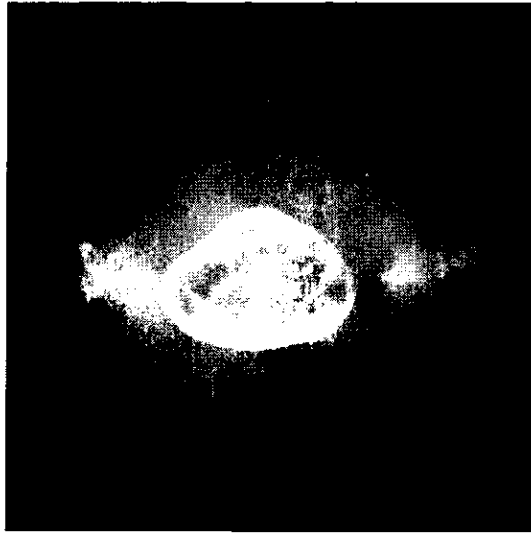
FIGURA 1.2: Imagen de NGC 6826 tomada del archivo público del Space Telescope Science Institute, Baltimore, EE. UU. (HTTP://WWW.STSCI.EDU).

se debe principalmente a un efecto de selección, pués los nudos o estructuras *como-chorros* que se encuentren en las zonas más brillantes de la nebulosa son más difíciles de detectar.

Balick et al. (1998) encuentran que una gran parte de los FLIERs tienen morfologías de *cabeza-cola*, con las colas apuntando hacia afuera del núcleo. También establecen la presencia de gradientes de ionización, el cual decrece con la distancia a la estrella central. Estos gradientes son consistentes con la presencia de un frente de ionización atrapado en nudos neutros de densidades $\approx 10^4$ cm^{-3}. Para explicar la naturaleza física de estos nudos se han propuesto la siguiente serie de mecanismos :

- **Inestabilidades en el borde.** Algunas microestructuras que se encuentran en la periferia de NP elípticas pueden ser inestabilidades que se forman en el lugar donde el frente de ionización (FI) pasa y rompe el borde de la envolvente densa y se acelera (Breitschwerdt & Kahn 1990).

- *Balas* **estelares.** El intenso enriquecimiento de nitrógeno (a veces hasta en un factor de 5) en los FLIERs, sus velocidades supersónicas, y su relativamente corta edad cinemática sugieren que podrían ser *balas* supersónicas eyectadas por la fuente central.

- *Balas* **nebulares.** Se considera también la posibilidad de que los FLIERs se formen dentro o cerca de la envolvente debido a la interacción de vientos.

Figura 1.3: Imagen de NGC 7009 tomada del archivo público del Space Telescope Science Institute, Baltimore, EE. UU. (HTTP://WWW.STSCI.EDU).

- **Flujos fotoevaporados de nudos neutros.** Los FLIERs también podrían ser nudos de gas neutro que son fotoevaporados por el campo de radiación ionizante de la estrella central y por el campo de radiación difuso nebular (López-Martín et al. 2001, Mellema et al. 1998, Cantó et al. 1998).

- *Rockets* **Oort-Spitzer.** Este mecanismo propone que los nudos neutros serían acelerados debido a la pérdida de masa debida a la fotoevaporación (Mellema et al. 1998, Oort & Spitzer 1955). Se produciría un aumento de la velocidad radial conforme la pérdida de masa aumenta. De esta forma, los nudos con velocidades radiales más altas serían observables por poco tiempo.

- **Modelo MHD** Un campo magnético toroidal congelado en el gas del viento de la nebulosa planetaria, si se considera que la estrella central está rotando, es capaz de formar flujos colimados en los que se podrían formar los nudos (Różyczka & Franco 1996).

- "Estancamiento" de chorros Este modelo explica la formación de FLIERs sobre el eje de simetría del viento bipolar estelar. Los nudos se forman en la zona de "estancamiento" del viento estelar donde hay una reducción del momento del flujo. Los nudos "estancados" se condensan del gas chocado del medio que los rodea, cuando el

material del medio interestelar no puede fluir más allá sobre el eje de simetría y se comprime formando un nudo denso en la seción cóncava del choque de proa formado. Esta concavidad es debida a la disminución del momento del flujo del vientop estelar bipolar.

También se encuentran microestructuras con emisión en líneas de bajo grado de ionización y morfologías similares a las descritas anteriormente, pero cuyas velocidades no siempre son mayores que la envolvente en expansión; en algunas ocasiones estas microestructuras se mueven con velocidades similares a las envolventes e incluso a veces son más lentas.

En los Capítulos 2 y 3 vamos a analizar en detalle las microestructuras de la nebulosa planetaria de la Hélice (NGC 7293).
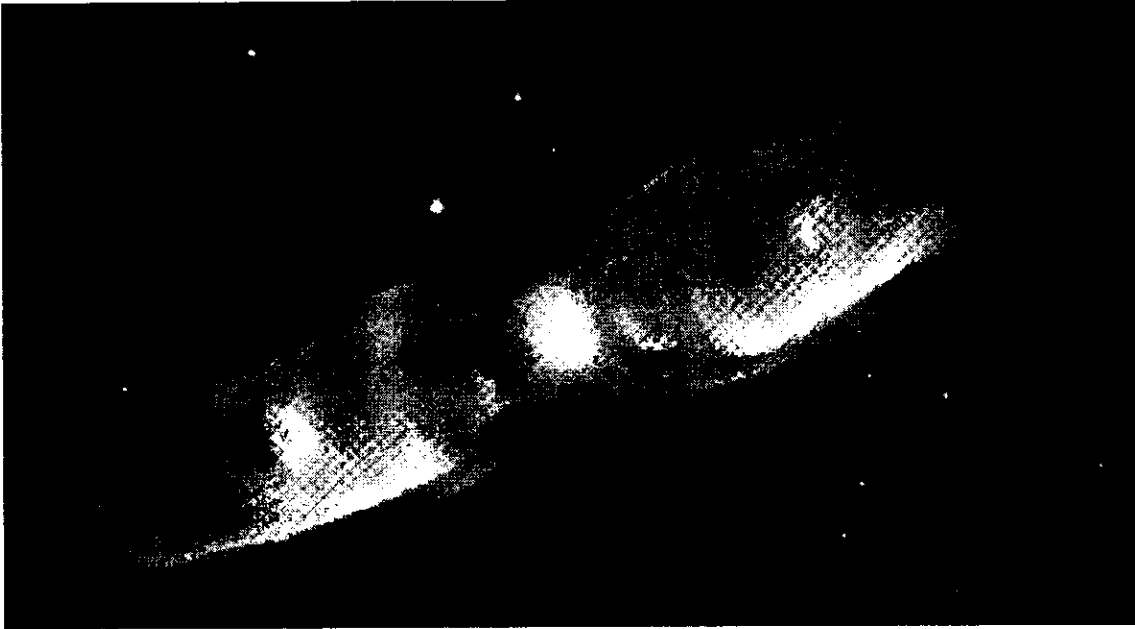
Figura   1.4: Imagen de la NP bipolar M 2-9 tomada del archivo público del Space Telescope Science Institute, Baltimore, EE. UU. (HTTP://WWW.STSCI.EDU), en la que se puede observar la colimación de los vientos asociados con la nebulosa.

1.3   Eyecciones colimadas en nebulosas planetarias

Las NPs muestran una gran variedad de morfologías, desde las esféricas y elípticas, hasta las formas axisimétricas más complicadas e incluso irregulares. En cambio, las envolventes circunestelares de la mayoría de las estrellas AGB se observan con simetría esférica. Para explicar estas morofologías deberíamos entender la teoría de la evolución estelar post-secuencia principal como la transformación de una gigante roja en la AGB en una NP no esférica. El modelo de "vientos estelares en interacción" (Kwok, Purton & Fitzgerald 1978) nos dice que el viento estelar ionizado y rápido (con velocidades ≥ 1000 kms^{-1}), interacciona con una envolvente circunestelar AGB que es más densa en el ecuador. Este modelo es capaz de explicar cualitativamente la presencia de algunas de las estructuras observadas en NPs. Sin embargo, no es capaz de explicar dos cosas, primero, el origen de las asimetrías en la envolvente circunestelar (la cual es tomada como un hecho en el modelo), y segundo, la presencia de estructuras con simetría puntual (SP).

Para explicar las asimetrías observadas en las envolventes circunestelares se han pro-

puesto varios mecanismos como son la rotación estelar, campos magnéticos internos o externos a la estrella (Różyczka & Franco 1996, García-Segura 1997, García-Segura & López 2000) y la presencia de sistemas binarios (Soker & Livio 1989, Reyes-Ruíz & López 2000). Se piensa que el fenómeno físico que está generando estas morfologías nebulares es de naturaleza transitoria, y que se debe estar produciendo en las etapas iniciales de la formación de la NP.

No se ha encontrado una correlación clara de la morfología nebular con la velocidad de expansión nebular, ni con la masa de gas ionizado o neutro en la nebulosa, ni con el ritmo de pérdida de masa de la progenitora AGB.

Se han detectado NPs con flujos múltiples y estructuras multipolares. En estos casos se ha sugerido que chorros episódicos, bipolares y rotantes (BRETs [2]) sean los responsables de las morfologías observadas (López et al. 1993, López et al. 1995). Sin embargo, se piensa que el papel de estos BRETs es secundario, pués se supone que generan las estrucutras de SP dentro de una nebulosa no esférica preexistente, cuya no esfericidad podría ser debida a la interacción de vientos. Algunos autores proponen un mecanismo de dos pasos para la formación de estas estructuras, con un flujo colimado de alta velocidad (de algunos cientos de km s^{-1}) que se genera en las últimas etapas de la fase AGB (o al principio de la fase post-AGB) interaccionando con una envolvente producida por la pérdida de masa de la fase AGB que se supone esféricamente simétrica. En este esquema se propone que la variedad de estructuras observadas y sus simetrías se pueden explicar en términos del cambio temporal de las propiedades (flujo de masa, ángulo de apertura y dirección) de los flujos colimados de alta velocidad.

Se piensa que las desviaciones de la estructura de SP se pueden deber a dos procesos : por desviaciones de la simetría bipolar de los chorros, o por desviaciones de la simetría en la envolvente de la progenitora AGB. Estas desviaciones claramente producirían estructuras nebulares irregulares como las observadas en algunas NPs. Sin embargo, cada vez hay más pruebas de que los vientos AGB son esféricamente simétricos (Sahai et al. 1998a, Sahai et al. 1998b), de manera que las asimetrías en el viento serían posteriores a esta etapa evolutiva.

En cualquier caso, queda incierto el mecanismo de producción de los flujos colimados. Uno de los mecanismos que se ha propuesto para la generación de estos flujos colimados es la presencia de un sistema binario (Soker & Livio 1989). Por otro lado simulaciones numéricas magnetohidrodinámicas han mostrado que el viento de una estrella aislada es capaz de ser colimado por un intenso campo magnético toroidal, y que la precesión del eje de rotación estelar (por el efecto de una compañera) puede cambiar la dirección de

---

[2]Bipolar Rotating Episodic Jets

estos flujos (García-Segura 1997, García-Segura & López 2000). Es en este sentido en el
que se hace importante tener la máxima información posible de estos objetos para poder
aumentar nuestro conocimiento acerca de estos flujos colimados (a través de las imágenes
directas y de su cinemática) que nos pueda revelar pistas acerca de su formación. En los
Capítulos 9 y 11 analizamos la morfología y la cinemática de la NP bipolar M 2-48 con
esta finalidad.

1.4   Eyecciones colimadas en regiones H II

La formación de estrellas de tipo solar es un proceso gradual durante el cual hay una acre-
ción de masa de un disco denso y nubes que las envuelven. En esta acreción se produce una
liberación de momento angular que parece ser la responsable de la producción de chorros
a lo largo del eje polar de la estrella jóven. Estos chorros de gas que son eyectados con
velocidades superiores a las del sonido del medio circundante, interactúan con él generando
choques de proa característicos de los objetos Herbig-Haro (HH). Recientemente, se han
detectado una serie de chorros embebidos en regiones fotoionizadas (Reipurth et al. 1998,
O'Dell & Bally 2000). Desde un punto de vista teórico este escenario nos presenta una
oportunidad excelente para poder estudiar tanto la dinámica de los chorros como su ioni-
zación externa. Además, estos chorros nos ofrecen la oportunidad de poder avanzar en
nuestro entendimiento de los chorros HH ya que, mientras en los chorros estándares, (que
son prácticamente neutros), sólo podemos observar regiones limitadas que son excitadas
por choques, en los chorros HH fotoionizados la totalidad del haz del chorro es fotoionizado
y puede ser observado directamente (Reipurth et al. 1998, López-Martín et al. 2000).

En general, estas fuentes estelares tienen líneas de emisión de Hα brillantes, y sus
espectros sugieren que son estrellas T Tauri. Estas estrellas probablemente tienen discos
pequeños, quizá menores que 1$''$ de diámetro, que requieren de técnicas de observación de
subsegundos de arco para ser detectados. El mecanismo de aceleración del material podría
ser el resultado de la acreción de masa en un sistema binario con alta excentricidad, de
manera que en el paso por el periastro las fuerzas de marea se intensificarían provocando
esta aceleración de material del chorro que observamos.

En ausencia de agentes externos sería de esperar que los chorros muy jóvenes fueran si-
métricos. Las asimetrías observadas en la mayoría de los chorros más conocidos es atribuida
a un fuerte obscurecimiento del lóbulo que se aleja de nosotros debido a la alta extinción
del material circunestelar. En muchos casos, estudios en el infrarrojo han revelado la pre-
sencia de estos "chorros simétricos". Sin embargo, en el caso de los chorros fotoionizados
esta explicación no es satisfactoria pués no se encuentran asociados con regiones extendidas
de alta extinción.

Si los chorros son fotoionizados, se pueden determinar de las observaciones algunos parámetros con mayor precisión que en los chorros estándares excitados por choques. En el resto de los chorros estelares, estos parámetros han sido determinados a través de modelos de los choques que los hacen visibles.

Parte II

Microestructuras en nebulosas planetarias

Capítulo 2

Microestructuras en la nebulosa de la Hélice

2.1 Introducción general

La nebulosa de la Hélice (NGC 7293, P K36 − 57°1) es una de las NPs más cercanas, más grandes sobre el plano del cielo y más evolucionadas que conocemos (ver Figura 2.1). Tiene un radio angular de $\approx 6'$ que corresponde a unos 0.37 pc (a una distancia de 213 pc, Harris et al. 1998). En esta nebulosa se observan una serie de glóbulos neutros, todos ellos con una morfología muy similar. O'Dell & Handron (1996) detectan 313 nudos, y calculan que debe haber unos 3500 detectables en toda la nebulosa. Se encontró una buena alineación con la dirección radial hacia la estrella central. Se estima que la masa del núcleo neutro es de aproximadamente 1.5×10^{-5} M$_\odot$. Estos glóbulos neutros fueron reportados por primera vez por Vorontzov-Velyaminov (1968) utilizando el término de "filamentos" para describirlos.

En la actualidad, mediante observaciones con mejor resolución espacial se observa que el término "nudo cometario" (NC) da una mejor idea de su morfología, ya que se componen de una "cabeza" y una "cola" de morfología similar a la que presentan los cometas en el sistema solar. Los tamaños de estos NCs son del orden de 7″ (podemos encontrar una discusión un poco más detallada a este respecto en la sección 3.4.1 del Capítulo 3). El hecho de que no se encuentren NCs en la región más interna de la nebulosa es un argumento que nos permite suponer los NCs confinados en un disco ancho más que en una distribución esférica.

Las observaciones realizadas por O'Dell & Handron (1996) fueron sumamente importantes (ver Figuras 2.1 y 2.2), mostrando una multitud de nudos de forma altamente simétrica.
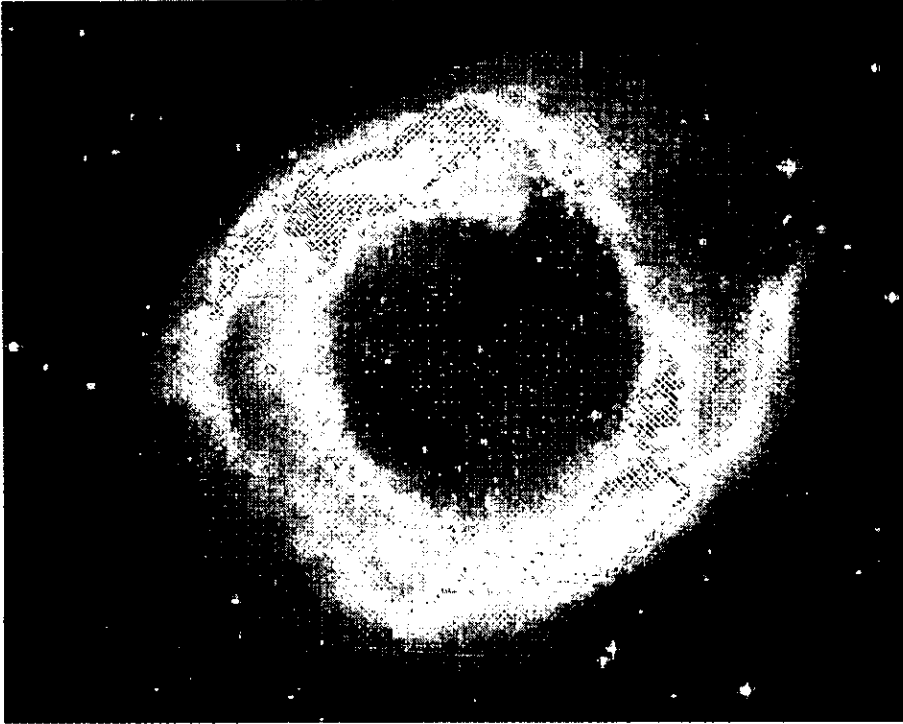
FIGURA 2.1: Imagen de NGC 7293 tomada del archivo público del Space Telescope Science Institute, Baltimore, EE. UU. (HTTP://WWW.STSCI.EDU), en la que se puede apreciar la estructura general de la nebulosa planetaria. En la parte superior de la figura podemos apreciar la posición de la WFPC utilizada en las observaciones de O'dell & Handron (1996).

Por otro lado Meaburn et al. (1998) han determinado la cinemática de un grupo de nudos cometarios brillantes de la nebulosa encontrando una expansión global del sistema de los NCs a una velocidad de unos $14\ \mathrm{km\ s^{-1}}$ (que es unos $17\ \mathrm{km\ s^{-1}}$ más lenta que la velocidad de expansión del gas que los rodea).

A través de observaciones en longitudes de onda de radio se encuentra una buena correlación entre la posición de los NCs y la emisión detectada en CO. En las imágenes ópticas no se encuentran NCs en la parte más interna y cercana a la estrella central, pero empiezan a ser muy numerosos cuando nos vamos acercando al anillo externo de la nebulosa. Al aproximarnos más al cuerpo principal de este anillo empieza a disminuir el número de NCs detectados , pero se piensa que esto es debido a que no se detectan frente a la emisión brillante de este anillo.
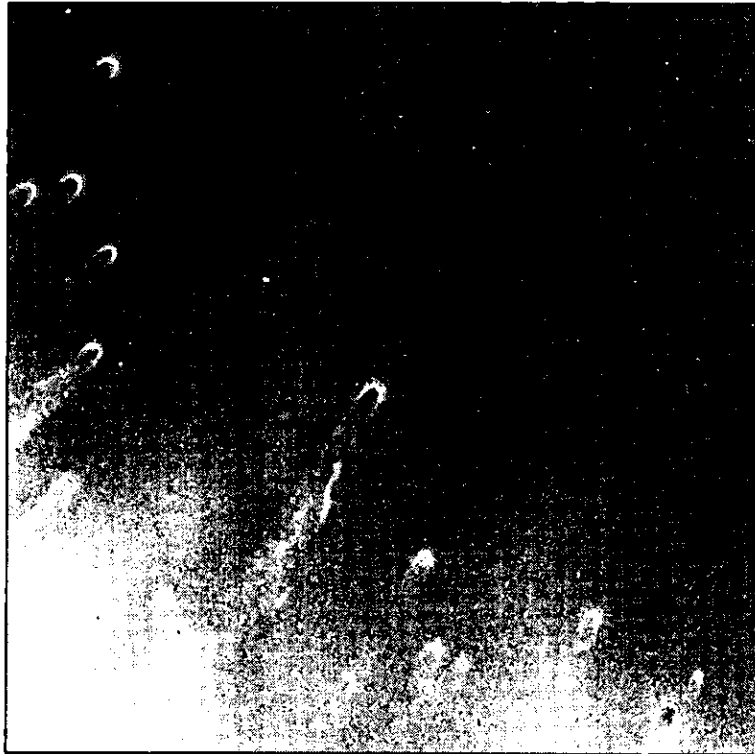
FIGURA 2.2: Imagen en Hα tomada del archivo público del Space Telescope Science Institute, Baltimore, EE. UU. (HTTP://WWW.STSCl.EDU), en la que se muestra uno de los campos observados por la WFPC en el que podemos observar en detalle algunos nudos cometarios.

Es muy importante encontrar cual es el origen de estos NCs para poder comprender mejor los procesos físicos que se están llevando a cabo en esta etapa evolutiva estelar. Para ello se han propuesto varios mecanismos :

- **Inestabilidades en el paso del frente de ionización** : Se propone que los nudos cometarios son el producto de inestabilidades en el cuerpo principal de la NP misma. Podrían originiarse como inestabilidades Rayleigh-Taylor (RT) en las primeras etapas de la evolución de la NP cuando la luminosidad de la estrella es alta y la zona ionizada de la NP está rodeada de una envolvente neutra.

- **Inestabilidades aceleradas por un viento estelar** : Se piensa que la interacción

entre un viento estelar de alta pérdida de masa y baja velocidad y un viento de
una fase posterior de baja pérdida de masa y alta velocidad de la estrella central
es la responsable de una gran parte de las morfologías observadas en las NPs. La
superficie de los choques formados por la interacción del "viento rápido" con el "viento
lento" eyectado previamente puede estar sujeta a inestabilidades R-T como propone
Capriotti (1973) para el frente de ionización principal de la nebulosa.

- **Nudos primordiales** Otra posibilidad es que los nudos cometarios tengan su origen
  en la etapa de formacion de la estrella central presente.

En la actualidad se está tratando de explicar el origen de la emisión de estos nudos co-
metarios. Se parte de la idea de que el material neutro es fotoionizado por el campo de
radiación ionizante de la estrella central (la "cabeza"). Se ha propuesto que las "colas" son
simplemente parte del material arrancado en las "cabezas" y que es arrastrado en el movi-
miento de éstas. Este escenario no explica satisfactoriamente la emisión observada. Para
solucionar este problema, nosotros estamos proponiendo un modelo analítico en el que las
"cabezas" se modelan como un viento fotoevaporado del nudo neutro, que es ionizado por
la radiación estelar ionizante, siguiendo e l formalismo propuesto por Cantó et al. 1998, y
nosotros proponemos que la emisión de las "colas" se puede modelar como un flujo fotoe-
vaporado del material neutro que queda en la sombra (al que no le llega radiación de la
estrella central), el cual es ionizado por la radiación difusa de la nebulosa. En el Capítulo
3 se describe en detalle este modelo.

Otro aspecto que ha sido analizado es la búsqueda de una correlación de alguna pro-
piedad física de los nudos cometarios y su distancia a la estrella central. En el Capítulo 3
se analiza esta posibiliad, así como otros aspectos relacionados con el campo difuso de la
nebulosa ionizada.

Capítulo 3

Photoevaporating flows from the cometary knots of the Helix Nebula (NGC 7293)

L. López-Martín[1], A. C. Raga[1],
G. Mellema[2], W. J. Henney[3] & J. Cantó[1]

[1]*Instituto de Astronomía, UNAM, Ap. 70-264, 04510 D. F., México*
[2]*Stockholm Observatory, SE-133 36, Saltsjöbaden, Sweden*
[3]*Instituto de Astronomía, UNAM, J. J. Tablada 1006, 58090 Morelia, Michoacán, México*

3.1 Abstract

We explain the Hα emission of the cometary knots in the Helix Nebula (NGC 7293) with an analytical model that describes the emission of the head of the globules as a photoevaporated flow produced by the incident ionizing radiation of the central star. We compare these models with the Hα emission obtained from the HST (*Hubble Space Telescope*) archival images of the Helix Nebula. From a comparison of the Hα emission with the predictions of the analytical model we obtain a rate of ionizing photons from the central star of about 5×10^{45} s^{-1}, which is consistent with estimates based on the total Hβ flux of the nebula.

We also model the tails of the cometary knots as a photoevaporated wind from a neutral shadow region produced by the diffuse ionizing photon field of the nebula. A comparison with the HST images allows us to obtain a direct determination of the value of the diffuse ionizing flux. We compare the ratio of diffuse to direct stellar flux as a function of radius inside an HII region with those obtained from the observational data through the analytical tail and head wind model. The agreement of this model with the values determined from the observations of the knots is excellent.

Key words: ISM: structure — planetary nebulae: individual (NGC 7293) — stars: AGB and post-AGB

3.2   Introduction

The small scale structure of the Planetary Nebula (PN) known as the Helix Nebula (NGC 7293, PK 36-57°1) is characterized by many thousands of small knots. These knots (which were first reported by Vorontsov–Velyaminov 1968) have a cometary shape, with their tails pointing away from the central source. Groundbased work (Meaburn et al. 1992, 1996, 1998) and Wide Field and Planetary Camera HST observations (O'Dell & Handron 1996; O'Dell & Burkert 1997; Burkert & O'Dell 1998) revealed a multitude of spatially resolved knots, about 3500, with highly symmetric appearance. The knots have also been detected in CO (Huggins et al. 1992) and, at least outside the main nebula, in C I (Young et al. 1997).

This PN is one of the closest to us with a parallax distance of 213 pc (Harris et al. 1997). Other methods have been applied to determine the distance to this PN, giving values ranging from 120 to 400 pc. Optical images show a complicated morphology characterized by a helical structure in Hα and [N II] and a more elliptical shape in [O III]. The deprojection of these images has proven to be difficult, with suggestions of both elliptical/toroidal shapes and bipolar ones (Meaburn & White 1982) being made. O'Dell (1998) has suggested that the ionized region is a disk.

The central star is very hot and has a low luminosity, indicating that it is well down the cooling track of its post-AGB evolution. The temperature of the central star of the Helix has been measured by the Hβ Zanstra method to be $\simeq 1.2 \times 10^5$ K (Górny, Stasińska & Tylenda 1997).

The high effective temperature combined with the fairly low luminosity and the large size of the PN , about 0.5 pc in diameter at a distance of 213 pc, leads to a complicated ionization structure with co-existing regions of high and low ionization character (O'Dell 1998; Henry, Kwitter & Dufour 1999). The low luminosity of the star also implies a very low

density wind, making it virtually undetectable. However, with its expected high velocity ($v_\infty \simeq 6000$ km s^{-1} if radiation driven) it could still have a dynamical effect on the PN structure.

The measured densities in the nebula are low, about 60 cm^{-3} (O'Dell 1998), in contrast with the densities derived for the neutral/molecular globules, $n_{knot} \sim 10^6$ cm^{-3} (O'Dell & Handron 1996). This leads to the curious result that a substantial fraction of the mass of the PN is in the form of these neutral globules. The aspherical shape of the PN is also found in the distribution of the knots and in the large scale CO emission. Meaburn et al. (1998) have shown that the knots follow the same velocity distribution as the CO, although at a lower typical expansion velocity. Young et al. (1999) found the deprojected expansion velocities of the knots and the CO ring to be 19 and 29 km s^{-1}, respectively.

Some other authors have treated the photoevaporation of clumps in an ionizing radiation field. Bertoldi & McKee (1990) developed an approximate analytic theory of the evolution of a photoevaporating cloud exposed to the ionizing radiation of a newly formed star, finding an equilibrium cometary cloud configuration. Johnstone, Hollenbach & Bally (1998) modelled the photoevaporation of dense clumps of gas by an external source of ultraviolet radiation including thermal and dynamical effects. Mellema et al. (1998) study the evolution of dense neutral clumps located in the outer parts of a planetary nebula (like the Helix nebula).

3.3 · Analytical model for the photoevaporated flux of the cometary knots

Let us discuss a simple, analytical model for cometary knots embedded in a Planetary Nebula (PN). First, we derive some expressions that relate the ionizing stellar flux and the particle flux of the photoevaporated wind in a similar way to Mellema et al. (1998) to find the Hα emission for the cometary heads. Cantó et al. (1998) proposed the idea of the tails as neutral shadow regions behind the clumps, and studied the complex time-evolution of the resulting flow. In this paper, we model the tails behind the Helix clumps as a cylinder of neutral material being photoionized by the diffuse ionizing flux of the nebula.

3.3.1 A model for the cometary head

Let us consider the problem of a hemispherical, neutral knot of radius R_h which is being photoionized by the radiative field emitted by the central star of the ionized nebula. A schematic diagram of this configuration is shown in Figure 3.1.
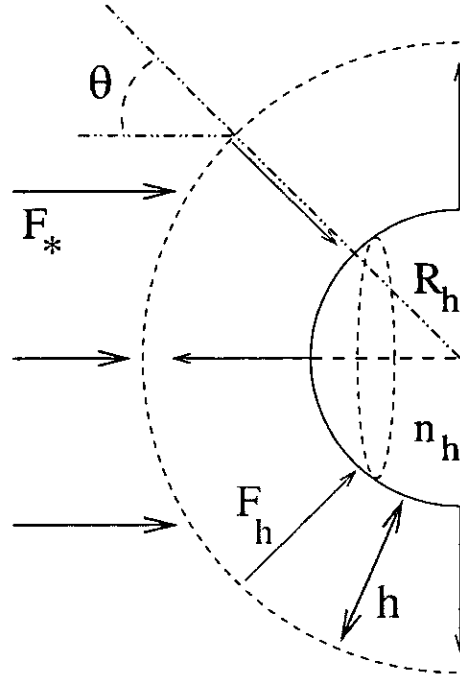
FIGURA 3.1: Schematic diagram of the cometary head. F_h is the incident flux at the surface of the neutral knot, and R_h and n_h are the radius and the density of the neutral knot (respectively).

A fraction of the stellar flux arrives at the knot surface, photoionizing the neutral knot material and feeding a photoevaporated flow. The remaining ionizing photons are absorbed in this photoevaporated flow. The neutral knot is being photoevaporated, but we consider a quasi-steady state in which the radius of the knot R_h is almost constant with time. The incident flux at the knot surface is :

$$F_h(\theta) = n_h(\theta) \, v(R_h) \,, \tag{3.1}$$

where F_h is the flux of ionizing photons incident normal to the knot surface (per unit area and time), n_h and $v(R_h)$ are the density and the velocity of the photoevaporated wind at the knot surface . We note that the rate of photoionizations depends on the angle of incidence θ (see Figure 3.2), having a maximum value in the front of the cometary head.

In order to obtain the density profile, we consider the conservation of particles in the photoevaporated wind :

$$R^2 n(R, \theta) v(R) = R_h^2 n_h(\theta) v(R_h) \,, \tag{3.2}$$

where R is the radius directed outwards from the knot.

We assume that the ionization front is thin compared with the effective thickness h of the ionized flow and that h in turn is small compared with R_h. In this case, if all diffuse photons are absorbed "on-the-spot", the photoionization balance is given by

$$F_\star \, \cos(\theta) \simeq F_h(\theta) + h_h^2(\theta) \, \alpha_B \,, \tag{3.3}$$

where α_B is the case B recombination coefficient of hydrogen, which is assumed to be constant with position. The flow thickness h is defined by :

$$h \equiv \omega \, R_h \,, \tag{3.4}$$

where the parameter ω is defined through the relation :

$$\omega_h^2 \, R_h \equiv \int_{R_h}^\infty n^2(r) \, dr \,. \tag{3.5}$$

This parameter ω depends on the density profile of the photoevaporated wind. For a D-critical ionization front ($v(R_h) = c_i$, where c_i is the isothermal sound speed of the ionized gas), $\omega \simeq 0.1$ (Henney & Arthur 1998). From equations (3.1-3.5) we then obtain a relation between the ionizing flux from the central star $F_\star$, and the incident flux at the knot surface $F_h(\theta)$:

$$F_\star \, \cos(\theta) \simeq F_h(\theta) + F_h^2(\theta) \, \frac{\omega \, R_h \, \alpha_B}{c_i^2} \,, \tag{3.6}$$

The term on the left is the ionizing stellar flux as a function of the angle of incidence, the first term on the right is the incident ionizing flux on the knot surface that produces the photoionizations of the neutral material and the second term is the flux absorbed in the photoevaporated wind. If we define :

$$\xi_h \equiv \frac{c_i^2}{R_h \, \omega \, \alpha_B} \,, \tag{3.7}$$

equation (3.6) can be written as :

$$F_\star \, \cos(\theta) \simeq F_h(\theta) + \frac{F_h^2(\theta)}{\xi_h} \,, \tag{3.8}$$

We can see from equation (3.8) that it is possible to find the incident flux $F_h(\theta)$ as a function of the ionizing flux $F_\star$ solving the quadratic equation to obtain :

$$F_h(\theta) \simeq \frac{\xi_h}{2} \left[\left(\frac{4 \ F_\star \ \cos(\theta)}{\xi_h} + 1 \right)^{1/2} - 1 \right] . \qquad (3.9)$$

We find two different limiting situations :

If $\xi_h/cos(\theta) << F_\star$ we have the *"Recombination Dominated Regime "* in which the fluxes are related by the expression :

$$F_h(\theta) \approx \sqrt{\xi_h \ F_\star \ \cos(\theta)} , \qquad (3.10)$$

In this case, an important fraction of the ionizing flux is absorbed in the photoevaporated wind and only a small fraction of the stellar flux arrives at the knot surface. The recombinations in the column beyond R_h mainly balance the stellar flux.

If $\xi_h/cos(\theta) >> F_\star$ we have the *"Flux Dominated Regime "*, in which :

$$F_h(\theta) \approx F_\star \ \cos(\theta) , \qquad (3.11)$$

In this regime almost all the stellar flux arrives at the knot surface and there is no absorption in the photoevaporated flow. The particle flux at R_h is roughly equal to the stellar flux.

In order to compute the total rate of Hα photons emitted by the head of a cometary knot, assuming $\omega \ll 1$ we have to evaluate the integral :

$$S_{H\alpha} \simeq \int_0^{\pi/2} 2 \ \pi \ R_h^2 \ \alpha_{H\alpha} \ n_h^2(\theta) \ \sin(\theta) \ \omega \ R_h \ d\theta , \qquad (3.12)$$

where $\alpha_{H\alpha}$ is the effective Hα recombination coefficient.

Taking into account the angular dependence of the density profile we can integrate (3.12) to obtain the Hα emission of the cometary heads :

$$S_{H\alpha} \simeq \pi R_h^2 \frac{\alpha_{H\alpha}}{\alpha_B} F_\star \left\{ 1 + \frac{\xi_h}{F_\star} - \frac{\xi_h^2}{6F_\star^2} \left[\left(1 + \frac{4F_\star}{\xi_h} \right)^{3/2} - 1 \right] \right\} . \qquad (3.13)$$

The term in curly brackets is the fraction of incident ionizing photons that are absorbed in the photoevaporating flow before reaching the ionization front. It is only this fraction of the incident photons that are reprocessed into Hα radiation. If we know the size of the knot R_h and the Hα emission $S_{H\alpha}$ we can use equation (3.13) to estimate the stellar flux.

3.3.2   A model for the cometary tail

For the cometary tail, we consider the problem of a cylinder of neutral material behind the cometary head being photoionized by the diffuse flux of the nebula. A schematic diagram
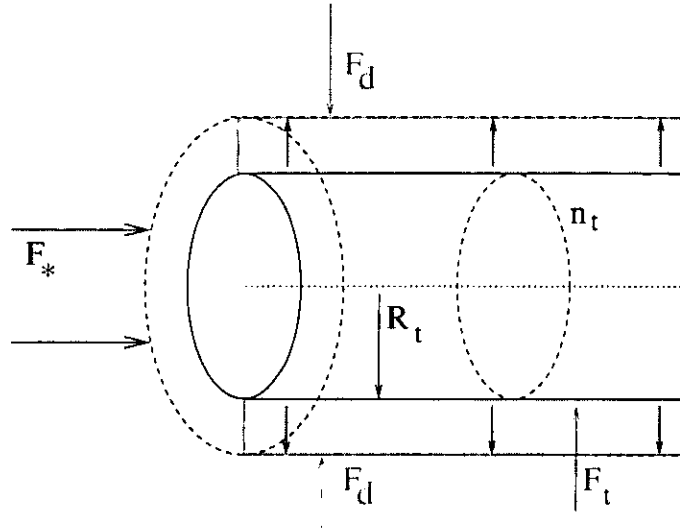
FIGURA 3.2: F_t is the incident flux at the surface of the neutral cylinder, F_d is the diffuse flux (produced by the surrounding nebula), and R_t and n_t are the radius and the density of the neutral tail (respectively).

of this configuration is shown in Figure 3.2. If we assume that the radius of the cometary head is much smaller than the distance to the source we can consider the shadow region to have polar symmetry. This cylindrical shadow does not receive direct stellar radiation. We therefore have :

$$F_d = F_t + \omega \ R_t \ n_t^2 \ \alpha_B \,, \tag{3.14}$$

where F_d is the diffuse ionizing flux of the surroundings, F_t is the incident flux at the tail surface and the second term on the right represents the absorptions in the photoevaporated wind of the cometary tail.

The incident flux at the neutral surface of the tail is related to the density n_t at the base of the cylindrical wind through :

$$F_t = n_t \ c_i \,, \tag{3.15}$$

Defining the parameter :

$$\xi_t \equiv \frac{c_i^2}{\omega \ \alpha_B \ R_t} \,, \tag{3.16}$$

and subsituting equations (3.15-3.16) in (3.14) one obtains :

$$F_d = F_t + \frac{F_t^2}{\xi_t} \, . \tag{3.17}$$

In order to obtain the total number of Hα photons emitted by the tails of the cometary knots, we assume that the Hα emitting region has a cylindrical section with a thickness $h \equiv \omega \, R_t$. The number of Hα photons emitted per unit time and per unit length of this cylinder is :

$$\frac{S_{H\alpha}}{\Delta l} = 2 \, \pi \, R_t \, \omega \, R_t \, n_t^2 \, \alpha_{H\alpha} \, , \tag{3.18}$$

and as a function of the parameter ξ_t the Hα emission is :

$$\frac{S_{H\alpha}}{\Delta l} = 2 \, \pi \, R_t \, \frac{\alpha_{H\alpha}}{\alpha_B} \, \frac{F_t^2}{\xi_t} \, , \tag{3.19}$$

where Δl is a unit of length along the cylindrical tail. If we combine equations (3.17) and (3.19) we can calculate the diffuse ionizing flux as a function of the Hα emission per unit length and the radius of the cylinder :

$$F_d = \frac{S_{H\alpha}/\Delta l}{2 \, \pi \, R_t} \, \frac{\alpha_B}{\alpha_{H\alpha}} + \left[\frac{S_{H\alpha}/\Delta l}{2 \, \pi \, R_t} \, \frac{\alpha_B}{\alpha_{H\alpha}} \, \xi_t \right]^{1/2} \, . \tag{3.20}$$

3.3.3   Diffuse ionizing field inside an H II region

As well as the radial ionizing radiation field from the Helix central star, there will also be a diffuse ionizing radiation field, principally due to ground level recombinations of hydrogen in the nebula, plus smaller contributions from helium recombinations and the scattering of stellar radiation by dust grains. For the purposes of calculating the properties of the knot tails, the important quantity is the lateral flux of the diffuse field, which is the flux incident on the surface of an opaque, radially aligned, thin cylinder.

In the "on-the spot" (OTS) approximation, in which all diffuse ionizing photons are assumed to be reabsorbed by neutral H very close to their point of emission, the diffuse flux, F_d, across any opaque surface is related to the stellar flux, F_*, at the same position by (Henney 2000)

$$\beta_{OTS} \equiv \frac{F_d}{F_*} = \frac{\alpha_1}{4\alpha_B \kappa} \, , \tag{3.21}$$

where α_1 and α_B are, respectively, the H recombination rates to the ground level and to all excited levels and $\kappa = \bar{\sigma}_d / \bar{\sigma}_*$, where $\bar{\sigma}_d$ is the mean photoionization cross-section averaged
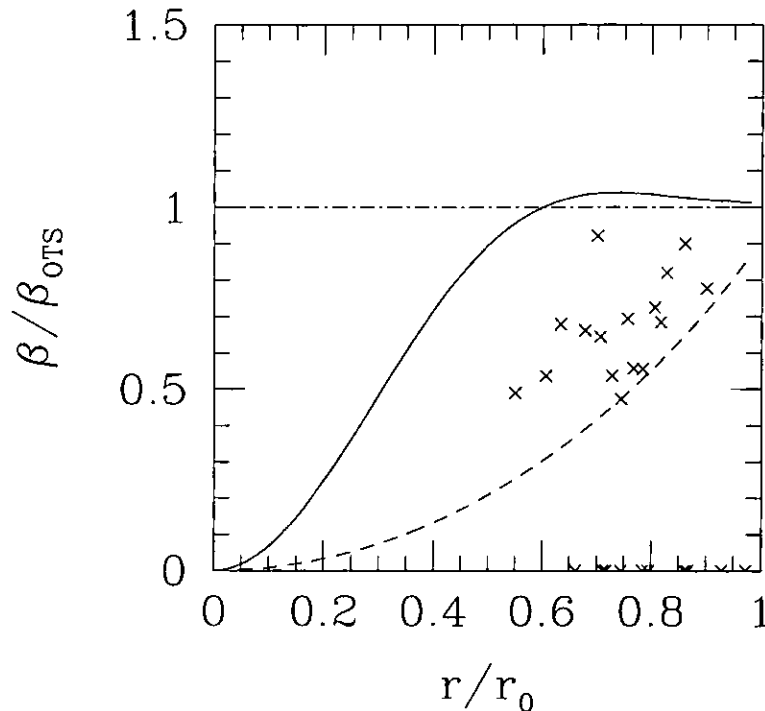
FIGURA 3.3: Comparison of the Henney (2000) models to the observed values of the diffuse to direct flux ratio (crosses) as a function of the distance from the ionization front. The upper horizontal line is the OTS value and the solid line and dashed line give the variation of β across the nebula for the filled-sphere and hollow-shell case, respectively.

over the diffuse ionizing spectrum and $\bar{\sigma}_*$ is the same quantity averaged over the stellar spectrum. Henney (2000) presents detailed calculations, in which the OTS assumption is relaxed, for the lateral diffuse flux in two simplified geometries: a classical filled-sphere homogeneous Strömgren H II region, and a hollow cavity H II region with the ionized gas concentrated in a thin spherical shell. It is found that in both cases the value of $\beta(= \frac{F_d}{F_*})$ is much smaller than β_{OTS} at small radii. It is because at small radii, F_* gets huge (r^{-2}) but F_d, which is proportional to the recombination rate times a path length, plateaus to a more or less constant value. In the thin-shell case, β remains at a low value throughout the interior of the cavity, only becoming comparable to β_{OTS} at the position of the shell. In the filled-sphere case, on the other hand, for the relatively high values of κ appropriate for the Helix knots (see below), β rises to $\simeq \beta_{OTS}$ at a fractional radius of $\simeq 0.5$ and is roughly constant thereafter.

The stellar ionizing radiation field is much harder than the diffuse field, while the photoionization cross-section declines rapidly with frequency above the ionization threshold. Hence, the ratio of mean cross-sections, κ, for the diffuse and stellar fields is larger than unity. Including the H and He^0 recombination spectrum gives $\bar{\sigma}_d \simeq 0.75\sigma_0$, where σ_0 is the threshold cross-section and He/H = 0.13 (O'Dell 1998; Henry, Kwitter & Dufour 1999) has been assumed.

The temperature of the central star of the Helix has been measured by the Hβ Zanstra method to be $\simeq 1.2 \times 10^5$ K (Górny, Stasińska & Tylenda 1997). A further constraint on the stellar spectrum is the observation (O'Dell 1998) that the He^{++} zone in the nebula is roughly half the radius of the He$^+$ zone, implying that roughly 10% of the ionizing photons have frequencies higher than the He$^+$ ionization limit. Model atmospheres for compact hot stars (Rauch 1997) that are consistent with these constraints have photon spectra $L_\nu/h\nu$ that are flat or rising between the H and He$^+$ ionization limits, implying a value of $\bar{\sigma}_* \simeq 0.17\sigma_0$.

Hence, $\kappa \simeq 4.5$ is appropriate for the Helix knots, which implies $\beta_{\text{OTS}} \simeq 0.033$ for an assumed electron temperature of 10^4 K. The true situation in the Helix nebula is probably intermediate between the filled-sphere and the hollow-shell case. Although O'Dell (1998) finds that the electron density is roughly constant with radius throughout the nebula, the central high-ionization "hole" has a higher temperature and hence a lower emissivity of diffuse ionizing photons. Furthermore, the geometry is more disk-like than spherical, which would tend to reduce the intensity of the diffuse field.

The radial dependence of β in the two limiting cases is shown in Figure 3.3. This is compared with the observational data in section 3.4.3.

3.4   Properties of the cometary knots

We have used the HST images from the data archive at the Space Telescope Science Institute to obtain the Hα emission from the cometary knots in the Helix Nebula. These images are flux-calibrated using the coefficients given in O'Dell & Doi 1999. The f656n and f658n filters were selected to isolate the Hα and [NII] emission at 658.4 nm.

Several methods have been used in order to obtain the distance to this PN (Cahn & Kaler 1971; Daub 1982; Cahn, Kaler & Stanghellini 1992; Harris et al 1997), leading to distances ranging from 120 to 400 pc. We use the value of 213 pc determined by Harris et al. (1997) from trigonometric parallax.

The comparison between the models and the observations is done for 26 knots, chosen for being relatively well isolated, and covering a range of distances to the central star.
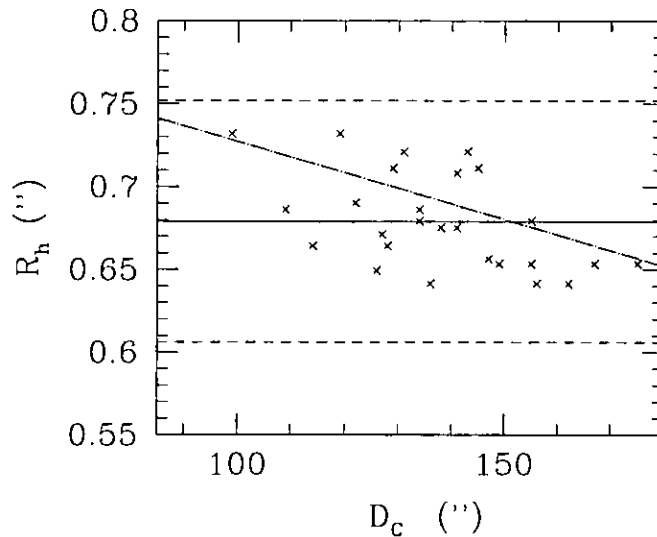
FIGURA 3.4: The angular radii of the knots as a function of projected angular distance to the central star. The crosses indicate the angular sizes determined for individual knots. The horizontal, continuous line indicates the mean value of knot radius, and the dashed horizontal lines give the value of the dispersion from the mean value. The oblique dotted line gives the best fit to the observed data.

3.4.1   Sizes of the knots

In order to determine the sizes of the knots, we carry out aperture photometry with a series of circular diaphragms (centred on the knots) of increasing angular radius. If one plots the flux within the aperture versus radius, for large enough radii the flux has to increase as the square of the radius (due to the presence of the bright, surrounding nebular environment). From a logarithmic plot it is then straightforward to determine the radius $R_{ext} = R_h + \omega R_h$ (see equations 3.4-3.5 and Figure 3.1) at which the quadratic flux vs. radius dependence first appears. In this way one then determines the value of the radius R_h of the neutral clump.

Applying this method to the 26 chosen knots we find that there is no correlation between the size of the knots and their distance to the central star (see Figure 3.4). However, this could be a result of the fact that we only have a few knots, and that these knots are not necessarily representative of the true distribution of knot sizes (as they were chosen so as to be well isolated, see above). We calculate a mean radius for the knots of $< R_h > = (0.68 \pm 0.07)$ ".

3.4.2   Hα intensities of the cometary heads

Subtracting the background from the fluxes determined with the aperture photometry, we obtain the Hα fluxes emitted by the knots. One can then use equation (3.13) to calculate the stellar ionizing flux at the position of the successive knots as a function of distance from the central star.

Column 4 of Table 3.1 gives the resulting Hα photon production rates $S_{H\alpha}$ of the knots, using values for $\omega = 0.1$ and $c_i = 10$ km s^{-1} (therefore $\xi_h \simeq 1.79 \times 10^{10}$ cm^{-2} s^{-1} for a knot with the mean radius $< R_h > = 0.68$ "). Figure 3.5 shows $S_{H\alpha}$ vs. D_h (where D_h is the projected distance between the source and the clumps).

Figure 3.5 also shows the $S_{H\alpha}$ vs. D_h predicted from equation (3.13) for different values of S_* ($= 4\pi D_h{}^2 F_*$). The predicted curves should represent upper envelopes of the observed points, as the real distances between the clumps and the source are larger than the observed, projected distances. From a comparison of the predicted curves with the values measured for the clumps, we see that the observations can best be fitted with a stellar ionizing photon rate of

$$S_* \approx 5 \times 10^{45} \text{ s}^{-1}. \tag{3.22}$$

If the knots were distributed isotropically around the central star, then the median knot would have a true distance $\simeq 1.15$ times greater than its projected distance. However, the lower envelope of the observed knot brightness distribution suggests that all knots lie within $\pm 45°$ of the plane of the sky, consistent with a ring-like spatial distribution.

According to Osterbrock (1989) S_* can be derived from the Hβ luminosity :

$$S_* = \frac{\alpha_B}{\alpha_{H\beta}^{\text{eff}}} \frac{L(H\beta)}{h\nu_{H\beta}}. \tag{3.23}$$

If we use the value of the Hβ luminosity of the Helix Nebula obtained by O'Dell (1998) we have a value for the stellar ionizing photon rate of 5.25×10^{45} s^{-1}. As we can see the match with our fit is excellent.

TABLA 3.1: Location and fluxes of the cometary knots

α_{2000}[a]	δ_{2000}[a]	R_h ($''$)	$S_{H\alpha}$[b] (s^{-1})	$S_{H\alpha}$[c] ($cm^{-1}\ s^{-1}$)	F_* ($cm^{-2}\ s^{-1}$)	F_d ($cm^{-2}\ s^{-1}$)	F_d/F_*
429	-860	0.73	10.84×10^{39}	2.96×10^{22}	1.02×10^{10}	1.67×10^{8}	1.63×10^{-2}
433	-853	0.69	5.16×10^{39}	1.60×10^{22}	7.21×10^{9}	1.29×10^{8}	1.79×10^{-2}
431	-844	0.66	4.67×10^{39}	2.53×10^{22}	7.53×10^{9}	1.70×10^{8}	2.26×10^{-2}
440	-848	0.73	4.30×10^{39}	–	5.93×10^{9}	–	–
452	-901	0.69	3.44×10^{39}	1.54×10^{22}	5.74×10^{9}	1.27×10^{8}	2.20×10^{-2}
428	-827	0.65	2.52×10^{39}	2.25×10^{22}	5.31×10^{9}	1.63×10^{8}	3.07×10^{-2}
459	-905	0.67	3.36×10^{39}	1.61×10^{22}	6.22×10^{9}	1.33×10^{8}	2.15×10^{-2}
413	-818	0.66	3.39×10^{39}	–	6.27×10^{9}	–	–
425	-822	0.71	3.67×10^{39}	–	5.93×10^{9}	–	–
352	-815	0.72	7.05×10^{39}	2.51×10^{22}	8.68×10^{9}	1.56×10^{8}	1.79×10^{-2}
410	-808	0.68	3.79×10^{39}	–	6.67×10^{9}	–	–
474	-931	0.69	6.11×10^{39}	1.52×10^{22}	7.99×10^{9}	1.26×10^{8}	1.58×10^{-2}
473	-919	0.64	2.55×10^{39}	1.53×10^{22}	5.89×10^{9}	1.36×10^{8}	2.31×10^{-2}
378	-800	0.67	4.26×10^{39}	1.58×10^{22}	7.13×10^{9}	1.32×10^{8}	1.86×10^{-2}
354	-804	0.71	5.14×10^{39}	1.81×10^{22}	7.21×10^{9}	1.33×10^{8}	1.85×10^{-2}
465	-853	0.67	2.35×10^{39}	–	5.10×10^{9}	–	–
480	-925	0.72	2.45×10^{39}	–	4.73×10^{9}	–	–
351	-802	0.71	5.32×10^{39}	3.16×10^{22}	7.35×10^{9}	1.78×10^{8}	2.41×10^{-2}
398	-752	0.66	3.22×10^{39}	1.68×10^{22}	6.06×10^{9}	1.38×10^{8}	2.28×10^{-2}
386	-750	0.65	3.31×10^{39}	1.78×10^{22}	6.17×10^{9}	1.68×10^{8}	2.73×10^{-2}
360	-751	0.68	2.79×10^{39}	2.62×10^{22}	5.61×10^{9}	1.68×10^{8}	3.00×10^{-2}
352	-750	0.65	3.94×10^{39}	–	6.82×10^{9}	–	–
389	-742	0.64	2.74×10^{39}	–	6.11×10^{9}	–	–
363	-740	0.64	3.19×10^{39}	2.45×10^{22}	6.67×10^{9}	1.73×10^{8}	2.59×10^{-2}
494	-911	0.65	2.77×10^{39}	–	5.55×10^{9}	–	–
372	-725	0.65	3.19×10^{39}	–	6.06×10^{9}	–	–

[a]System proposed by O'Dell & Burkert idnetifying a knot by its right ascension in units of $0^s.1$ (column 1) and by its declination in units of $1''$ (column 2)

[b]Hα production rate of the cometary head

[c]Hα production rate of the cometary tail
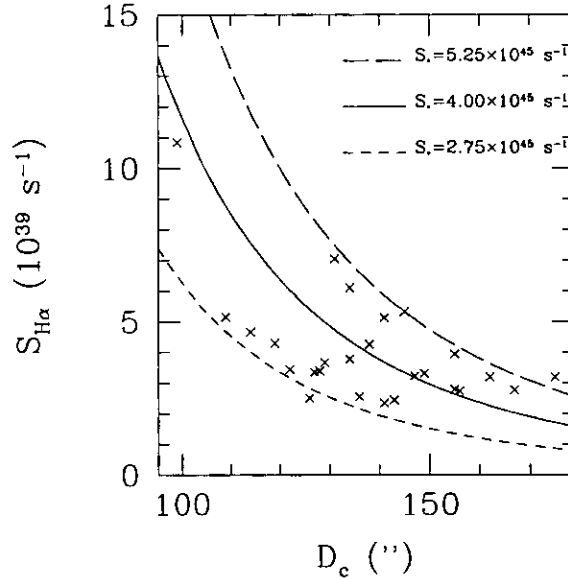
FIGURA 3.5: Model fits to the Hα photon rates observed for the knots (as a function of distance from the central star) obtained for different stellar ionizing photon rates. The predicted curves should represent upper envelopes of the observed points.

3.4.3   Hα intensities of the tails

In order to obtain the Hα emission from the tails we integrate the observed emission over a rectangular area covering the region in which the tails are clearly detected. We also integrate the emission in two small adjacent rectangular areas in order to determine the intensity of the nebular background, which we subtract from the emission of the box containing the cometary tail.

Knowing the Hα emission we can then calculate the diffuse flux with equation (3.20) for the 26 chosen knots. In this way we calculate the diffuse flux for different distances to the central star (see column 7 of Table 3.1). As we have also computed the direct stellar flux from the emission of the heads of the knots (section 3.4.2), we can then calculate the diffuse-to-direct stellar flux ratios, and compare these values with the ones predicted from

the (Henney 2000) models described in section 3.3.3. This comparison is shown in Figure 3.3, where we see that the observed points fall into the region between the curves delimited by the two models, indicating that the case of the Helix nebula is intermediate between the homogeneus sphere and the "thin shell" cases.

3.4.4   Knot masses and evaporation rates

From the analysis it is also possible to derive knot masses and evaporation rates. Under the assumption that the knots are accelerating and have an exponential density profile, one can derive their mass by

$$M = \left(1 - \frac{2}{\pi}\right) \frac{16 F_c(0) m c_i}{\pi c_n^2} R_c^3 \,, \tag{3.24}$$

see Mellema et al. (1998), equation (32). In this equation m is the average mass per atom or ion, for which we take 1.3 m_H, R_c is the radius of the clump, and c_n is the isothermal velocity of sound in the neutral gas for which we take 1 km s^{-1} (corresponding to 150 K). Applying this to the measured knots gives an average mass of 9×10^{-6} M$_\odot$ with knot masses ranging from 6×10^{-6} M$_\odot$ to 1.8×10^{-5} M$_\odot$. In the process one has to calculate the fraction of the ionizing flux which actually reaches the heads of the knots, $F_c(0)/F_*$, which comes out to be about 70 to 80%.

The mass range found is very close to the one derived by O'Dell & Handron (1996) and Meaburn et al. (1998) from dust extinction measurements and by Huggins et al. (1992) from CO measurements, showing that the sizes and shapes of the knots are entirely consistent with the photoevaporation model.

The model also allows an estimate of the current mass loss rate from the heads of the knots, which is given by

$$\frac{\mathrm{d}M}{\mathrm{d}t} = -F_c(0) m \pi R_c^2 \,, \tag{3.25}$$

see Mellema et al. (1998), equation (36). This gives an average of -2.2×10^{-9} M$_\odot$ yr^{-1} (ranging between -4.1 and -1.6×10^{-9} M$_\odot$ yr^{-1}).

3.5   Discussion

The results of the previous sections show that our photoevaporation model is entirely successful in explaining the current situation of the cometary knots in the Helix nebula. One could say that we are using the cometary knots as 'probes' for the direct and diffuse UV

radiation in the nebula, under the assumption that both the heads and tails are photo-evaporating. The results from the probes are consistent with the results found by other means.

The question which remains unanswered in this approach is the origin and final fate of the knots. Starting with the their final fate, the photoevaporation models give an estimate of the evaporation time.

The results from Mellema et al. (1998) show that the evaporation time of a knot is given by

$$t_{\text{evap}} = t_* \left(\frac{5}{6} + \frac{\ln(1 + \eta)}{6\eta} \right) , \tag{3.26}$$

with

$$t_* = \frac{48}{\pi} \left(1 - \frac{2}{\pi} \right) \frac{c_i R_c}{c_n^2 \pi} , \tag{3.27}$$

and

$$\eta = \frac{2\alpha_B F_* R_c}{3\pi c_i^2} , \tag{3.28}$$

which applied to the measured knots gives an evaporation time of 1.1 to 1.2×10^4 years. The time for the clumps to move from close to the star to their present position is about 6×10^3 years. In the "Flux Dominated Regime" the evaporation time is $t_{\text{evap}} \approx R_c c_i c_n^2$, so that once a clump starts to shrink by evaporation, the timescale gets shorter and shorter. There is an uncertainty in this number since the sound speed in the neutral gas is not well defined. Probably, the knot has a range of temperatures, depending for instance on how far the molecule dissociating photons penetrate. The evaporation time is inversely proportional to the temperature, the values quoted being valid for 150 K. Huggins et al. (1992) cite a temperature of 25 K for the CO gas in the knots.

One consequence of the photoevaporation is that gas is fed into the region surrounding the knots. Interestingly enough the Helix Nebula seems to be special among PNe in that its 'central cavity' is not empty but is at least partly filled with high ionization gas producing detectable amounts of [OIII] lines, see for example O'Dell (1998) and Henry et al. (1999). The density of this gas is derived to be around 50 cm^{-3}, perhaps less. We conjecture that this material was injected into the cavity by the photoevaporating clouds. Taking a radius of 200″ for the cavity, and assuming a spherical shape (probably an overestimate of the volume and hence of the mass), one finds that the evaporation of 3000 to 5000 knots of about 10^{-5} M$_\odot$ can supply this amount of gas. This equals the mass and current number of knots in the Helix. Possibly the gas filling the central cavity is from already evaporated

knots, or from the current knots. In Mellema et al. (1998) it was shown that 50% of the mass of a photoevaporating clump is lost during the first 'collapse phase'. Since the current knots apparently are in the 'cometary phase' they might easily have already lost half of their initial mass.

The question of the origin of the knots can be divided into two questions: "Why do they have a cometary shape?" and "What physical process is responsible for their existence?". Three models exist to explain their shapes. Dyson et al. (1993) showed that collisions between a supersonic wind and a clump produce short stumpy tails, and that only the interaction between a subsonic wind and a subsonic flow from a clump can produce long, comet–like tails. When applying this theorem to our model we run into the problem that the shapes derived in Dyson et al. (1993) are the shapes of the contact discontinuity between the flow from the clump and the wind, which we do not trace in our photoionization description. The dynamical models in Mellema et al. (1998) contain both the photoionization processes and the interaction of the photoevaporation flow with the environment. In those models the shape of the contact discontinuity is far from comet–like, as predicted by Dyson et al. (1993); but at the same time the contact discontinuity is not a region which produces a lot of emission, as the ionization front outshines it by many factors. However, in that model the environment does not exert any ram pressure on the clump and its photoevaporation flow. If the ram pressure in the environment is high enough it will overwhelm the photoevaporation flow, and dominate the dynamics. Observations show that the environment of the cometary knots has a density of about 50 cm^{-3} and a temperature of perhaps 20,000 K. If the environment is flowing subsonically, this implies pressures of order 10^{-10} dyn cm^{-2}. The photoevaporation pressure is given by $2F_c m c_i$ (see Mellema et al. 1998), which gives values of about 10^{-8} dyn cm^{-2}. Clearly the environment will not be able to overwhelm the photoevaporation flow from the knots.

We cannot rule out the possibility that some time in the past the cometary knots were shaped into their cometary shape through a wind–clump interaction. In fact, below we will argue for such a scenario to explain the origin of the knots.

Cantó et al. (1998) suggested that long tails can be formed behind clumps opaque to ionizing UV photons. The region behind the clump does not see any direct ionizing photons from the star, just the diffuse UV radiation field, which in general leads to denser, partly neutral tails forming behind the clumps. However, these tails will be initially the same density as the environment, fill up and recombine, striving towards pressure equilibrium with the ionized environment. The tails of the Helix knots are overpressured compared to their environment, a situation which does not occur in the scenario put forward in Cantó et al. (1998). The overpressured tails suggest that they were formed under different circumstances from the ones in which they are now.

Burkert & O'Dell (1998) proposed that the knots are shaped by Lyα photon radiation pressure. This was partly motivated by the fact that the evaporation flows appear to have exponential brightness profiles. These autors found that this mechanism does not work in the cometary knots of the Helix nebula. A similar model was proposed for the Proplyds in the Orion nebula (O'Dell 1998). Henney & Arthur (1998) showed that the exponential brightness profiles are *not* inconsistent with photoevaporation flows and that the radiation pressure from Lyα is at least one order of magnitude too low to be significant. Their arguments also hold for the Helix Nebula cometary knots and we will not repeat them here. The conclusion is that none of the three models can explain the origin of the long cometary tails under the current circumstances.

When we consider the origin of the knots there are basically two options, the knots are either primordial or the result of instabilities. Meaburn et al. (1998) and Young et al. (1999) favour the primordial model, the main arguments being that the CO gas outside of the main nebula has a very clumpy distribution, and that the velocity distribution of the cometary knots follows that of the main CO emission, albeit at a lower expansion velocity. Within this model it is possible that the tails were shaped as the knots were run over by the main part of the nebula. During this phase they would be surrounded and eroded by subsonically flowing gas, which according to the Dyson et al. (1993) model would produce long thin tails. Also, the formation of the tails as ionization shadows behind the clumps as proposed by Cantó et al. (1998) would in this case produce long, dense tails. After the main nebular shell has passed by, the knots find themselves fully exposed to the ionizing stellar radiation and the tails to the diffuse UV radiation field and both start photoevaporating, which is the stage in which we see them now.

O'Dell & Handron (1996) prefer the model in which the knots are formed as Rayleigh–Taylor instabilities on the inside of the swept up main nebula, proposed originally by Capriotti (1973). The numerical model of R–T instabilities presented in figure 4 in O'Dell & Burkert (1997) seems to support this model; it shows elongated structures pointing radially to the centre of the nebula. However, the much higher resolution models of Walder & Folini (1998) show the R–T instabilities to be much more chaotic. The fingers in their model need a lot of processing before they look anything like the cometary knots, and one would also expect much more variation in knot properties if they were formed in such instabilities. In all we prefer the first option of primoridal knots.

3.6 Conclusions

In this paper we propose an analytical model for the heads of the cometary globules in the Helix Nebula, in which the emission is assumed to come from a flow which is being

photoevaporated from the surface of a neutral clump. Using the Hα emission obtained from HST images of the Helix Nebula (extracted from the HST archive, see also O'Dell & Handron 1996; O'Dell & Burkert 1997) and the predictions from our analytic model, we can calculate the ionizing stellar photon flux at the positions of the knots.

We find that the knot brightnesses are fully consistent with the ionizing photon luminosity of $S_\star = 5.25 \times 10^{45}$ s^{-1} for the central star, deduced from the total Hβ flux of the nebula. This value, however, is somewhat uncertain as in the present work we have made no attempt to substract the [N II] 6583 flux from the f656n filter. Given the rather strong [N II] emission of some of the Helix Knots, our Hα flux determinations could in some cases lie up to ≈ 30% above the real Hα fluxes of the knots. The angular size of the knots has a value of $< R_h > = (0.68 \pm 0.07)$ ″ (where R_h is the radius of the neutral clump forming the knot, see section 3.4.1). From our small sample of 26 knots, we find no correlation between R_h and distance from the central star (see Figure 3.4).

The photoevaporation model also predicts masses for the knots, which come out fully consistent with observationally derived masses. Their evaporation time is between several thousands to 10^4 years, dependent on the temperature of the neutral gas in the knots.

In this paper we also present a model for the cometary tails as a flow which is being photoevaporated from a neutral, cylindrical "shadow region" behind the neutral clumps which form the knots. This flow is photoevaporated by the impinging diffuse ionizing field, formed in the surrounding nebula. As we have done for the heads of the cometary globules, we compare the emission of the cometary tails with the predictions from our model in order to quantitatively determine the value of the diffuse ionizing photon flux at the positions of the globules.

Knowing the direct stellar radiation and the diffuse flux at different distances from the central star (i.e., at the positions of the cometary globules), we can then calculate the diffuse-to-direct ionizing flux ratio ($F_d/F_\star$) as a function of distance from the central star. We compare the data with simple models for the diffuse ionizing field (Henney 2000) and conclude that the diffuse field is intermediate in magnitude between that expected from a filled and shell-like geometry, which may be due to the disk-like nature of the Helix nebula.

References

[1] Bertoldi, F. & McKee, C. F. 1990, ApJ, 354, 529

[2] Burkert, A. & O'Dell, C. R. 1998, ApJ, 503, 792

[3] Cahn, J. H.& Kaler, J. B. 1971, ApJS, 22, 319

[4] Cahn, J. H., Kaler, J. B. & Stanghellini, L. 1992, A&AS, 94, 399

[5] Cantó, J., Raga, A. C., Steffen, W. & Shapiro, P. 1998, ApJ, 502, 695

[6] Capriotti, E. R. 1973, ApJ, 179, 495

[7] Daub, C. T. 1982, ApJ, 253, 679

[8] Dyson, J. E., Harquist, T. W. & Biro, S. 1993, MNRAS, 261, 430

[9] Górny, S.K., Stasińska, G. & Tylenda, R. 1997, A&A, 318, 256

[10] Harris, H.C., Dahn, C.C., Monet, D.G. & Pier, J.R. 1997, in IAU Symp. 180, Planetary Nebulae, ed. H. Habing (Dordretch : Reidel), 40

[11] Henney, W. J. 2000, in preparation

[12] Henney, W. J. & Arthur, S.J. 1998, AJ, 116, 322

[13] Henry, R.B.C., Kwitter, K.B. & Dufour, R.J. 1999, ApJ, 517, 782

[14] Huggins, P.J., Bachiller, R., Cox, P. & Forveille, T. 1992, ApJ, 401, 43

[15] Johnstone, D., Hollenbach, D. & Bally, J. 1998, ApJ, 499, 758

[16] Meaburn, J., Clayton, C. A., Bryce, M., Walsh, J. R., Holloway, A. J. & Steffen, W. 1998, MNRAS, 294, 201

[17] Meaburn, J., Clayton, C. A., Bryce, M. & Walsh, J. R. 1996, MNRAS, 281, L57

[18] Meaburn, J., Walsh, J. R., Clegg, R. E. S., Walton, N. A., Taylor, D. & Berry, D. S. 1992, MNRAS, 255, 177

[19] Meaburn, J. & White, N.J. 1982, Ap&SS, 82, 423

[20] Mellema, G., Raga, A. C., Cantó, J., Lundqvist, P., Balick, B., Steffen, W. & Noriega-Crespo, A. 1998, A&A, 331, 335

[21] O'Dell, C.R. 1998, AJ, 116, 1346

[22] O'Dell, C. R. 1998, AJ, 115, 263

[23] O'Dell, C. R. & Doi, T. 1999, PASP, 111, 1316

[24] O'Dell, C. R. & Burkert, A. 1997, in IAU Sym p. 180, Planetary Nebulae, ed. H. Habing (Dordretch : Reidel), 332

[25] O'Dell, C. R. & Handron, D. 1996, AJ, 96, 23

[26] Osterbrock, D. E. 1989, Astrophysics of Gaseous Nebulae and Active Galactic Nuclei (Mill Valley : University Science Books)

[27] Rauch, T. 1997, A&A, 320, 237

[28] Vorontsov-Velyaminov, B. A. 1968, in Planetary Nebulae: IAU Symposium 34, eds. D. E. Osterbrock & C. R. O'Dell (Dordrecht:Reidel) 256

[29] Walder, R. & Folini, D. 1998, A&A, 330, L21

[30] Young, K., Cox, P., Huggins, P. J., Forveille, T. & Bachiller, R. 1999, ApJ, 522, 387

[31] Young, K., Cox, P., Huggins, P. J., Forveille, T. & Bachiller, R. 1997, ApJ, 482, L101

Parte III

Eyecciones colimadas en nebulosas fotoionizadas

Capítulo 4

Fotoionización del material eyectado por una estrella jóven

4.1 Chorros fotoionizados por estrellas jóvenes

Los objetos Herbig-Haro (HH) normalmente son identificados por medio de la emisión óptica de los choques de proa que son excitados por colisiones producidas en la interacción de material eyectado por estrellas jóvenes con el medio ambiente.

Presentan un espectro en líneas de emisión bastante rico, con líneas que van desde los átomos neutros (por ejemplo C I, N I, O I) a iones de ionización moderada (por ejemplo S III, O III, Ne III). Los objetos HH se observan la mayoría de las veces, ya sea en el óptico o en el infrarrojo, con estructuras bipolares centradas en estrellas T Tauri. En algunos casos uno de los lóbulos no es detectado en el óptico, y se ha argumentado que esto es debido a la alta extinción del material circunestelar en el que están embebidos.

Los objetos HH "normales" se encuentran embebidos en medios neutros o moleculares, y la emisión que detectamos proviene de las regiones excitadas por choques. Recientemente, se han detectado objetos HH que se encuentran embebidos en regiones fotoionizadas (Reipurth et al. 1998, O'Dell & Bally 2000). Estos objetos son de especial interés pues nos dan la oportunidad de "ver" el haz de material eyectado por la estrella central que es fotoioniado por el campo de radiación ionizante de la region H II en la que se encuentran embebidos.

Vamos a tratar de analizar el efecto de la fotoionización sobre el haz de material eyectado por la estrella jóven. Para ello, supongamos que inicialmente tenemos un chorro de material neutro, al que le está incidiendo lateralmente un campo de radiación ionizante (ver Figura 4.1).
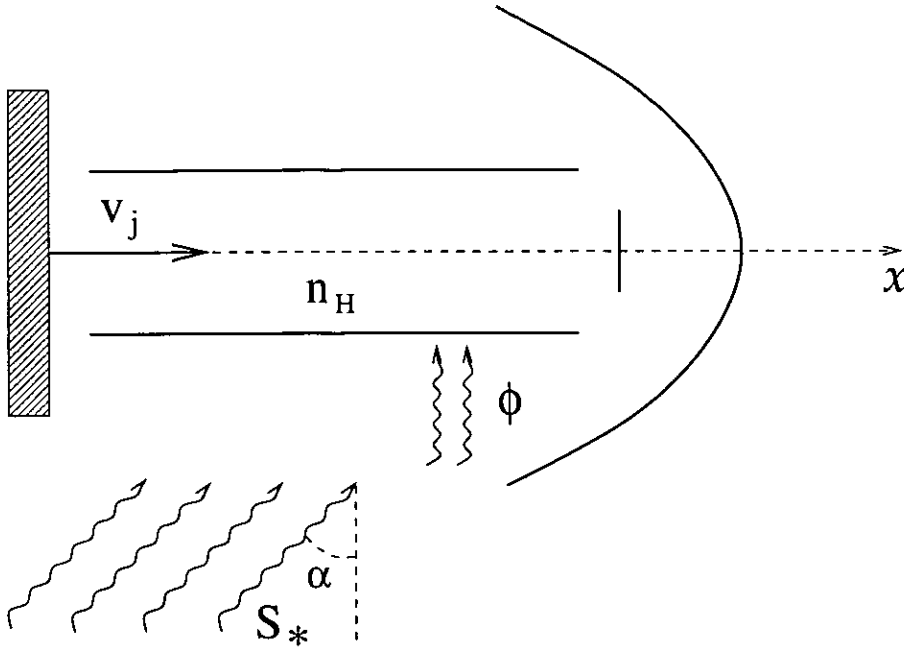
FIGURA 4.1: Esquema de la geometría de un chorro que es fotoionizado lateralmente.

Si suponemos que la fuente emite $S_\star$ fotones ionizantes por segundo, la cantidad de fotoionizaciones por átomo de hidrógeno neutro viene dado por :

$$\Phi = \frac{S_\star}{4\pi D_{\star j}^2} \sigma_{\nu_0} \cos\alpha \, , \tag{4.1}$$

donde $D_{\star j}$ es la distancia de la fuente ionizadora al chorro, σ_{ν_0} es la sección eficaz de fotoionización del hidrógeno, y α es el ángulo que forman la dirección que une la estrella ionizante con el chorro y la dirección normal a la eyección del material.

La evolución temporal de la ionización del gas viene determinada por :

$$\frac{df n_H}{dt} = (1 - f) n_H \Phi - f^2 n_H^2 \alpha_B \, , \tag{4.2}$$

donde α_B es el coeficiente de recombinación radiativa del hidrógeno en el caso B, n_H es el número de átomos de hidrógeno por unidad de volumen y f es la fracción de ionización que está definida como :

$$f = \frac{n_{HII}}{n_H} \, . \tag{4.3}$$

En la ecuación 4.2 hemos supuesto que toda la sección del chorro puede ser descrita con un valor único de f. Este valor representa la fracción de ionización promediado sobre la sección del haz. Despejando de esta expresión 4.2, obtenemos que :

$$dt = \frac{dx}{v_j} = \frac{df}{\Phi - f\Phi - f^2 n_H \alpha_B} \,, \tag{4.4}$$

e integrando obtenemos :

$$\frac{x}{v_j} = \frac{1}{n_H \alpha_B (f_1 - f_0)} \left[\ln \frac{f - f_0}{f - f_1} - \ln \frac{f_0}{f_1} \right] \,, \tag{4.5}$$

donde f_0 y f_1 son las soluciones a la ecuación $f^2 n_H \alpha_B + f\Phi - \Phi = 0$,

$$f_0 = \frac{-\Phi + [\Phi^2 + 4 n_H \alpha_B \Phi]^{1/2}}{2 n_H \alpha_B} \tag{4.6}$$

y

$$f_1 = \frac{-\Phi - [\Phi^2 + 4 n_H \alpha_B \Phi]^{1/2}}{2 n_H \alpha_B} \,. \tag{4.7}$$

Podemos verificar que cuando nos encontramos en la base del jet ($x \to 0$), el material está neutro. Mientras que a mayores distancias de la fuente ($x \to \infty$) la fracción de ionización tiende a f_0, que es el valor en el equilibrio de fotoionización.

Despejando de la expresión 4.5 podemos encontrar la fracción de ionización en cualquier punto del cilindro de material neutro eyectado por la estrella :

$$f(x) = (1 - e^{-\lambda x})/(\frac{1}{f_0} - \frac{e^{-\lambda x}}{f_1}) \,, \tag{4.8}$$

con

$$\lambda = \frac{[\Phi^2 + 4 n_H \alpha_B \Phi]^{1/2}}{v_j} \,. \tag{4.9}$$

Podemos definir una longitud característica :

$$L = \frac{1}{\lambda} = \frac{v_j}{[\Phi^2 + 4 n_H \alpha_B \Phi]^{1/2}} \,, \tag{4.10}$$

Esta longitud característica viene determinada por la velocidad de eyección del material, la densidad, y el campo de radiación de la fuente ionizadora. Si la longitud del chorro es mucho mayor que esta longitud característica, ($l \gg L$), el chorro se encuentra casi totalmente ionizado.
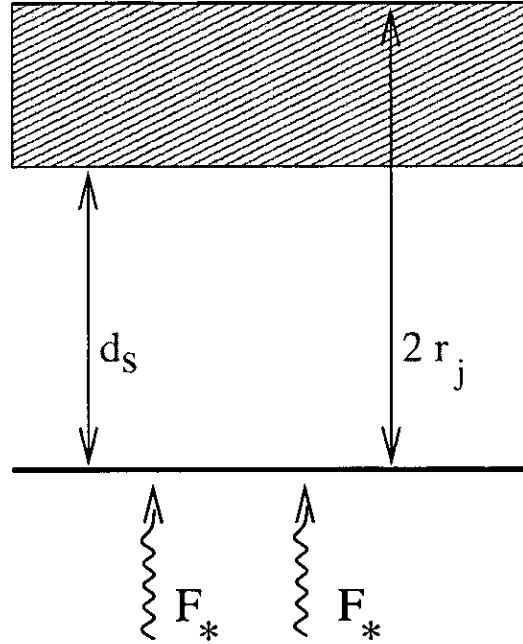
FIGURA 4.2: Sección del material inicialmente neutro fotoionizado por una fuente ionizante externa.

4.2   Posición del frente de ionización

En la sección anterior vimos como encontrar la fracción de ionización en cada punto del cilindro de material neutro eyectado por la estrella jóven, y encontramos en qué punto este haz está totalmente ionizado. Ahora consideraremos un modelo bidimensional, que nos permite encontrar la posición del frente de ionización en el cilindro a diferentes distancias de la fuente central.

Para ello, supongamos que los fotones cuya energía es suficiente para ionizar al hidrógeno están incidiendo perpendicularmente en una sección cilíndrica de material neutro (ver Figura 4.2). Podemos definir una *distancia de Strömgren* en la que se encuentra el frente de ionización dentro del cilindro :

$$d_s = \frac{F_\star}{n_j^2 \alpha_B} , \tag{4.11}$$

donde $F_\star$ es el flujo de fotones ionizantes incidentes de la estrella ionizadora y n_j es la densidad del material en el cilindro. Llamando r_j al radio del chorro, si $d_s < 2r_j$ el frente de ionización está atrapado en el material, mientras que si $d_s \geq 2r_j$, el frente de ionización
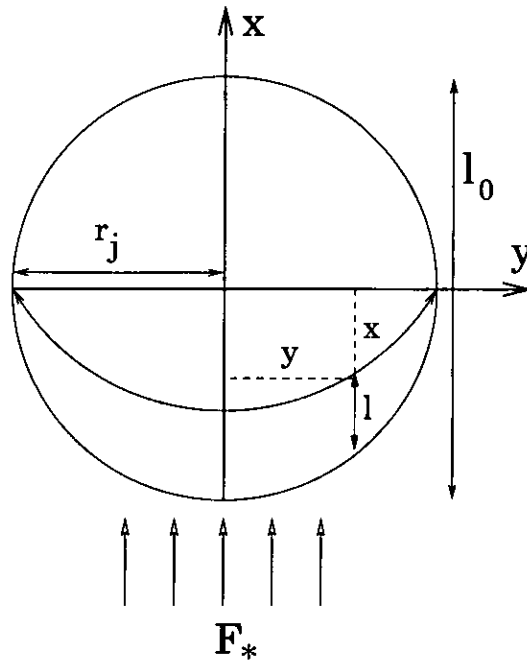
FIGURA 4.3: Esquema de un corte de la sección a una distancia z de la fuente central.

atraviesa completemente el material y tendremos un cilindro de material ionizado.

Esto ocurre si consideramos que el material está en reposo. Ahora bien, si el material está moviéndose respecto de la fuente, el frente de ionización ocupa una posición diferente para diferentes distancias de la fuente central.

Si l(z) es la longitud ionizada medida sobre una sección del cilindro a una distancia z de la fuente (ver figura 4.3), tenemos que :

$$F_\star = n_j \frac{dl(z)}{dt} + n_j^2 \alpha_B l(z) \,. \tag{4.12}$$

El primer término del miembro de la derecha de la expresión anterior representa el flujo de átomos neutros que se ionizan, y el segundo término representa las recombinaciones. Teniendo en cuenta que $v_j = dz/dt$ podemos reescribir 4.12 como

$$v_j \frac{dl(z)}{dz} = \frac{F_\star}{n_j} - n_j \alpha_B l(z) \,, \tag{4.13}$$

La expresión 4.13 se puede integrar para obtener la longitud de la sección ionizada del chorro para diferentes puntos a lo largo del cilindro de material :

$$l(z) = ds \left[1 - e^{-z/d_{rec}} \right] ,\tag{4.14}$$

donde hemos definido la *distancia de recombinación* como :

$$d_{rec} = \frac{v_j}{n_j \alpha_B} .\tag{4.15}$$

Las cooredenadas de la superficie del frente de ionización se pueden relacionar con las coordenadas (x, y, z) por :

$$x(y, z) = l(z) - \sqrt{r_j^2 - y^2} ,\tag{4.16}$$

por lo que podemos obtener la ecuación de la superficie del frente de ionización (normalizando al radio del chorro) :

$$\frac{x(y, z)}{r_j} = \left(\frac{ds}{r_j} \right) \left[1 - e^{z/d_{rec}} \right] - \sqrt{1 - \left(\frac{y}{r_j} \right)^2} .\tag{4.17}$$

En el siguiente capítulo se describe analíticamente como es el paso del frente de ionización por un chorro de material neutro que se encuentra embebido en una región fotoionizada. Se desriben los efectos dinámicos del paso de un frente de ionización tipo R y tipo D. También se presentan simulaciones numéricas realizada con el código hidrodinámico tridimensional "yguazú" para comparar la posición del frente de ionización con respecto a las predicciones analíticas. Finalmente, se analiza el caso del chorro fotoionizado HH 444 que se encuantra embebido en la región de σ Orionis.

Capítulo 5

The emergence of a neutral Herbig-Haro jet into a photoionized nebula

A. C. Raga[1], L. López-Martín[1], L. Binette[1],

J. A. López[2], J. Cantó[1], S. J. Arthur[3],

G. Mellema[4], W. Steffen[5] & P. Ferruit[6]

[1]*Instituto de Astronomía, UNAM, Ap. 70-264, 04510 D. F., México*

[2]*Instituto de Astronomía, UNAM, Ap. 877, 22800 Ensenada, B. C., México*

[3]*Instituto de Astronomía, UNAM, J. J. Tablada 1006, 58090 Morelia, Michoacán, México*

[4]*Stockholm Observatory, SE-133 36, Saltsjöbaden, Sweden*

[5]*Instituto de Astronomía y Meteorología, Universidad de Guadalajara, Avenida Vallarta 2602, 44130 Guadalajara, Jalisco, México*

[6]*Department of Astronomy, University of Maryland, College Park, MD 20742, USA*

5.1 Abstract

Recent observations show the existence of an increasing number of collimated outflows ejected by young, low mass stars which are embedded in H II regions. At distances of a

few tens of astronomical units from the star, at least one lobe of these outflows will be shielded from the ambient ionizing radiation by the compact, high extinction circumstellar disk. Within these shielded regions, the jets are probably mostly neutral, similar to the jets in "normal" Herbig-Haro (HH) objects. At larger distances, these jets emerge into the photoionized nebula, and start to be photoionized by the radiation from the ionizing photon source of the nebula.

In this paper, we model the photoionization of an initially neutral HH jet. This process begins as an ionization front at the side of the jet which is directed towards the ionizing star of the nebula, and progresses into the beam of the jet. There are two possible solutions. In the first solution, the jet beam becomes fully ionized through the passage of an R-type ionization front. In the second solution, the ionization front slows down enough to become a D-type front (or is already a D-type front at the point in which the jet emerges into the photoionized nebula), forming a partially ionized jet beam, with an expanding photoionized region and a compressed neutral region.

We explore these two types of solutions both analytically and numerically, and discuss the observational effects introduced by this jet photoionization process, concentrating in a region of parameter space that straddles the parameters deduced for HH 444 (the jet from V 510 Orionis).

Key words: stars : formation – ISM : jets and outflows – ISM : H II regions – hydrodynamics

5.2   Introduction

Recent observations have drawn attention to the peculiar case of jets ejected from young, low mass stars which are embedded in photoionized regions. Such jets have been observed, for example, in the Orion M 42 nebula (O'Dell et al. 1997), and the Trifid nebula (Rosado et al. 1999). However, the possibly most dramatic observations of jets within photoionized regions is the one of Reipurth et al. (1998), who find a sistem of 4 Herbig-Haro (HH) jets (HH 444, 445, 446 and 447) embedded in the H II region excited by σ Orionis.

The jets observed by Reipurth et al. (1998) display morphological properties that closely resemble those of the "normal" HH objects and their source stars have spectra typical of T Tauri stars (one of them is in fact a known T Tauri star, V 150 Ori). Therefore, we would expect these jets to have physical properties which are very similar to those of the classical HH jets. In particular, they should be mostly neutral close to the source star, where they can be protected from the ionizing radiation by the circumstellar disk. This should be especially true for the HH 444 system, in which the main jet is directed away

from the ionizing star of the H II region (σ Orionis).

However, as the jet travels away from the source, it leaves the high extinction region close to the T Tauri star, and emerges into the direct glare of the radiation produced by the ionizing photon source of the nebula. This impinging radiation photoionizes the side of the jet directed towards the ionizing photon source of the nebula, producing an ionization front that eats into the jet beam as the jet travels away from its source. This theoretical scenario was described by Reipurth et al. (1998).

In the present paper, we develop the theory of the sideways photoionization of an initially neutral jet by an external, impinging ionizing radiation field, concentrating on parameters appropriate for the HH 444 jet (Reipurth et al. 1998). We first describe some simple, analytic considerations about this problem (section 5.3), and then present results from 3D numerical simulations including both the gasdynamics and the radiative transfer (section 5.4). The expected observational properties of the flow are discussed in section 5.5 . Finally, the results are summarized in section 5.6.

Let us point out that there seems to be little doubt that HH 444 is indeed embedded in an H II region (not being a foreground or background object). The main bow shock of HH 444 shows a rather diffuse structure, which is quite different from the very sharp, filamentary structure of other HH bow shocks. This diffuse morphology corresponds to what is to be expected for a bow shock which is being photoionized by an external photon source. We will present detailed models of such photoionized bow shocks in a future paper.

Finally, we would like to point out that a partially similar situation might be found in jets ejected by central stars of Planetary Nebulae (PNe). Such stars might eject mostly neutral jets in a pre-PN stage, and the jets would get photoionized as the star rapidly evolves in the Hertzprung-Russell diagram to much higher effective temperatures (Reyes-Ruiz & López 1999). In future work, we will study this related problem in detail.

5.3   Analytical considerations

5.3.1   The parameters for HH 444

HH 444 is ideally suited to be used as a test case for our theoretical study, as estimates of its physical parameters are available in Reipurth et al. (1998). Following these authors, we assume that the H II region excited by σ Orionis (in which HH 444 is embedded, see above) is at a distance of 400 ± 50 pc. For this distance, we obtain a projected separation between V 510 Ori (the source of the HH 444 jet) and σ Orionis of ≈ 1.73 pc. For the ionizing star (which is actually a multiple star, with the brightest component being an O9.5 star) we assume an effective temperature $T_{eff} = 31000$ K and a total production rate of ionizing

photons $S_* = 10^{48}$ s^{-1}.

The electron density obtained for the knots along the HH 444 jet has values of $\sim$ 300 cm^{-3}, leading Reipurth et al. (1998) to assume a somewhat higher $n_j = 500$ cm^{-3} number density (of atoms and ions) for the base of the jet flow. We also follow Reipurth et al. (1998) in adopting this value.

The observed angular diameter of this jet is of $\approx 1''$, giving a jet radius of $r_j = 3 \times 10^{15}$ cm.

Finally, as there are no proper motion determinations it is not possible to deduce neither the orientation of the jet nor the jet velocity. Again, following Reipurth et al. (1998), we adopt a jet velocity of $v_j = 200$ km s^{-1}, which is consistent with the velocities observed for other HH jets.

5.3.2   Solutions with a R-type front

The most simple solution to the problem of a neutral jet emerging into a region with a strong, photoionizing radiation field is obtained for the case in which the ionization front is a fast, R-type front. In this case, the ionization front produces only a small perturbation in the density and velocity as it propagates across the beam of the jet.

Let us consider a top hat jet with outer radius r_j, number density (of atoms and ions) n_j and velocity v_j independent of the distance z from the jet source. We assume that the external ionizing field impinges from the $-x$ direction, as shown in the schematic diagram of Figure 5.1. We describe the position of the ionization front with a coordinate l, measured parallel to the x-axis, starting from the outer edge of the jet beam (see Figure 5.1). This coordinate is related to the (x, y, z) coordinates of the surface of the ionization front through the simple geometrical relation :

$$x(y,z) = l - \sqrt{r_j{}^2 - y^2}\,. \tag{5.1}$$

The equation of motion for the ionization front can be written as :

$$v_j \frac{dl}{dz} = \frac{F_*}{n_j} - n_j \alpha_B l\,, \tag{5.2}$$

where α_B ($= 2.55 \times 10^{-13}(10^4\mathrm{K}/T_I)^{0.79}$ cm^3 s^{-1}, see Cantó et al. 1998) is the case B recombination coefficient of hydrogen, and F_* is the number of ionizing photons impinging on the side of the jet beam per unit area and time. If the jet is geometrically thin, one can compute F_* for any angle θ between the jet axis and the direction towards the star as :

$$F_* = \frac{S_*}{4\pi D_*{}^2} \sin\theta\,, \tag{5.3}$$
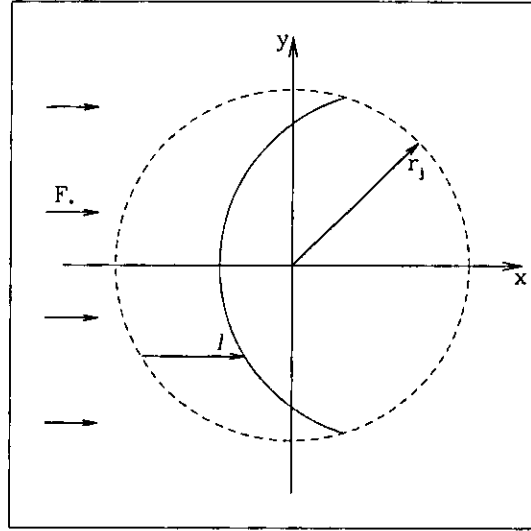
FIGURA 5.1: Schematic diagram showing the circular cross section of the jet (of radius r_j, dashed circle) and the position of the ionization front (solid curve) produced by the incident ionizing photon flux F_*.

where D_* is the distance from the jet cross section to the ionizing photon source, which emits S_* ionizing photons per unit time. Assuming that the jet is far away from the ionizing star (so that D_* and θ can be considered as approximately constant along the jet), equation 5.2 can be integrated and then combined with equation 5.1 to obtain the equation for the surface of the ionization front :

$$\frac{x}{r_j} = \left(\frac{d_s}{r_j}\right)\left[1 - e^{-(z/d_{rec})}\right] - \sqrt{1 - \left(\frac{y}{r_j}\right)^2}. \tag{5.4}$$

Two characteristic distances appear in this equation, the Strömgren distance (associated with the structure of the cross section) :

$$d_s = \frac{F_*}{n_j{}^2 \alpha_B} = 4.36 \times 10^{16}\,\text{cm}\,\left(\frac{500\,\text{cm}^{-3}}{n_j}\right)^2$$

$$\times \left(\frac{S_*}{10^{48}\text{s}^{-1}}\right)\left(\frac{400\,\text{pc}}{D_\odot}\right)^2 \left(\frac{T_I}{10^4\text{K}}\right)^{0.79}\cos^2\phi\,\sin\theta, \tag{5.5}$$

and the distance of recombination (associated with the dependence on distance from the source) :

$$d_{rec} = \frac{v_j}{n_j \alpha_B} = 1.57 \times 10^{17} \, \text{cm}$$

$$\times \left(\frac{500 \, \text{cm}^{-3}}{n_j} \right) \left(\frac{v_j}{200 \, \text{km s}^{-1}} \right) \left(\frac{T_I}{10^4 \text{K}} \right)^{0.79} , \tag{5.6}$$

which we have written normalized to the parameters of HH 444. In equation ??, $D_\odot$ is the distance to the sun, θ is the angle between the jet axis and the direction to the ionizing photon source (see equation 5.3), and ϕ is the angle between the jet axis and the plane of the sky. In both equations 5.4 and 5.3.2, the temperature dependence of the recombination coefficient is reflected in the factor containing the temperature T_I ($\approx 10^4$ K) of the photoionized region of the jet beam.

Assuming that $T_I = 10^4$ K, $\phi = 0$ and $\theta = \pi/2$, we derive $d_s/r_j = 7.27$ (from equation 5.3.2 with the parameters deduced for this object, see section 5.3.1). In order to visualize the topology of the ionization front, in Figure 5.2 we have plotted the (x, y) cross section of the jet for several values of the distance z from the source. In this figure, we show the solutions for $d_s/r_j = 7$, 3 and 1.5 . This model sequence in decreasing d_s/r_j can be viewed as representing three sources of decreasing ionizing flux F_* or, alternatively, jet flows of increasing density n_j. The $d_s/r_j = 7$ model corresponds to the nominal parameters derived for HH 444 (see section 5.3.1). The $d_s/r_j = 3$ and 1.5 values could also correspond to HH 444, e. g. if the density at the base of the jet was higher than estimated (780 or 1100 cm^{-3}, respectively). Alternatively, these two values for d_s/r_j could be obtained for HH 444 by considering an appropriate deprojected direction for the jet axis. The solution for $d_s/r_j = 7$ is very simple, with the ionization front going through the jet at an almost constant rate. In the solution for $d_s/r_j = 3$, the ionization front slows down appreciably as it goes through the cross section of the jet. Finally, for $d_s/r_j = 1.5$, the ionization front becomes "trapped" inside the cross section of the jet (see figure 5.2).

It is easy to show from equation 5.3.2 that all of the solutions for $d_s/r_j < 2$ correspond to ionization fronts that are trapped inside the body of the jet at large distances from the source. However, it is clear that before the ionization front reaches the asymptotic shape for large z (see the bottom diagram of figure 5.2), it will have a transition from R- to D-type. Therefore, the solutions obtained from equation 5.3.2 are not valid for $d_s/r_j < 2$, since for the derivation of this equation it was assumed that we have a fast, R-type front.

We should point out that the calculation of this section also has the implied assumption that the thickness of the ionization front is considerably smaller than the jet diameter. Approximating the thickness of the ionization front as $d_{IF} \approx 10/n_j \sigma_{\nu_0}$ (where σ_{ν_0} is the photoionization cross section of hydrogen at the Lyman limit, see Dyson & Williams
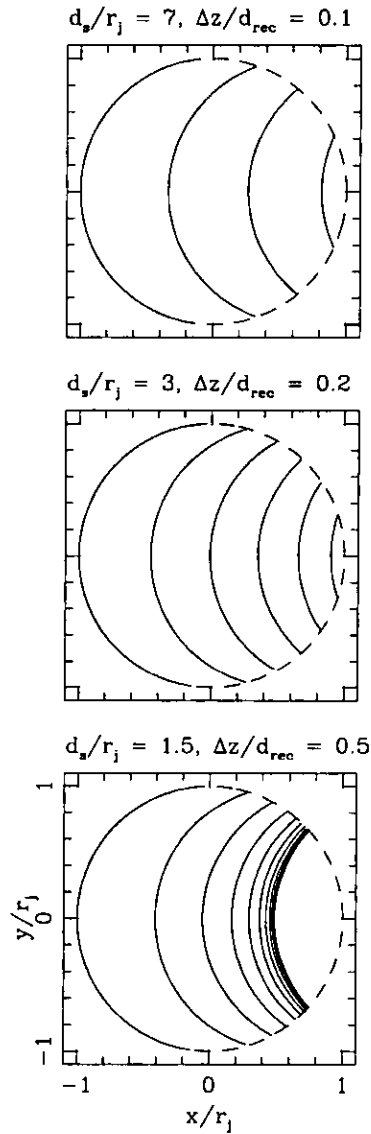
FIGURA 5.2: Solutions for the position of the ionization front obtained (from equation 5.4) for $d_s/r_j = 7$ (top graph), 3 (centre) and 1.5 (bottom) for several values of z/d_{rec}. The dashed lines represent the circular cross section of the jet, and the solid lines show the position of the ionization front for different values of the distance from the jet source along the z-axis (z/d_{rec}=0, 0.1, 0.2 and 0.3 in the top graph; z/d_{rec}=0, 0.2, 0.4, 0.6, 0.8 and 1 in the central graph; z/d_{rec}=0, 0.5, 1, onwards in the bottom graph, showing the convergence to a high z, "trapped ionization front" solution).

1997), we obtain $d_{IF}/(2r_j) \approx 0.05 \times (500\,\mathrm{cm}^{-3}/n_j)$. Therefore, the assumption of a thin ionization front is clearly applicable for the case of HH 444.

We should also mention that we have limited our analysis to the case of a jet beam with constant density and cylindrical radius as a function of distance z from the source. In a more realistic situation, the jet is likely to start broadening with increasing z, resulting in an outwardly decreasing density. However, this broadening will be quite complex, as the photoionized region of the jet is likely to open out more than the neutral region. This will result in a complex jet cross section, an accurate description of which requires a full numerical simulation of the flow (as done in section 5.4).

Finally, we should point out that in the above we have treated the diffuse ionizing radiation in the "on the spot" (case B) approximation. In reality, the diffuse radiation emitted by the surrounding nebula will produce an ionization front surrounding the beam of the jet. This front will possibly be a D-type front due to the fact that the diffuse field has a considerably lower intensity than the one of the direct radiation from the photoionizing source. This photoionization by the diffuse field has been studied in a different context by Cantó et al. (1998), but the results of their work still give a qualitative idea of the effect of the diffuse ionizing radiation for the present flow.

5.3.3   Solutions with a D-type front

In section 5.3.2, we have developed a simple description of a R-type ionization front sweeping across the beam of an initially neutral jet. For the front to be D-type, it has to satisfy the condition :

$$\frac{v_j}{\sqrt{1 + (dz/dl)^2}} < 2\,c_I \,, \tag{5.7}$$

where $c_I \approx 10$ km s^{-1} is the sound speed of the photoionized gas, and l is defined in Figure 5.1 . This equation is strictly valid for the midplane of the jet (i. e., the plane through the centre of the jet, and parallel to the direction of the impinging ionizing photon flux). Combining equations 5.2 and 5.7, one can rewrite the condition for the existence of a D-type front as :

$$l > d_c \equiv d_s - \frac{2\,c_I}{n_j \alpha_B} \,, \tag{5.8}$$

where we have also assumed that the angle between the surface of the ionization front and the flow axis is small (i. e., that $dl/dz \ll 1$). Of course, if we have $d_c > 2r_j$, the ionization front will sweep through the whole jet width as an R-type front. If $d_c < 0$, the ionization front will be D-type already at the point where the jet emerges into the ionizing photon

field. Finally, if $0 < d_c < 2r_j$, the ionization front will initially be R-type, and have a transition to a D-type front at $l = d_c$. For the parameters that we have chosen for HH 444, we obtain $d_c/(2r_j) = 4.42$, indicating that the ionization front is R-type throughout its passage across the jet beam.

If we have a D-type ionization front going through the jet beam, it will have a leading shock which pre-compresses the neutral beam material before it is photoionized. This shock pushes the neutral beam material away from the ionizing photon source. Also, the photoionized material will leave the surface of the ionization front with an approximately sonic velocity in the direction of the photon source. In this way, we would expect to obtain a broadening of the jet along the direction defined by the incident ionizing photon flux.

A similar flow has been studied analytically by Bertoldi & McKee (1990) and by Mellema et al. (1997) for the case of a spherical, neutral cloud which is being photoionized by an external radiative field. In principle, it is possible to apply similar techniques to solve for the evolution of the neutral cross section of the jet. Small modifications would have to be applied to account for the approximately polar symmetry of the photoionized sidewind from the neutral region of the jet beam (as opposed to the approximately spherical geometry of the wind from a neutral clump). We do not go through this exercise in the present paper.

5.4 Numerical simulations

We have computed numerical models of an initially neutral jet emerging into an ionizing radiation field with the new "yguazú" code, which is described in detail by Raga et al. (1999). This 3D code integrates the gasdynamic equations, a rate equation for neutral hydrogen, and the radiative transfer of the ionizing radiation (at the Lyman limit) from an arbitrary number of sources. The radiative cooling is computed with a simple, parametrized approximation to the real, non-equilibrium cooling. For the present application, we only consider the radiation produced by the ionizing star of the H II region. The diffuse ionizing field is treated in the on-the-spot approximation.

We have computed three models, the parameters of which are listed in Table 5.4. The three models have been computed in a uniform, Cartesian grid of $N_x \times N_y \times N_z = 40 \times 40 \times 100$ grid points. We have applied free outflow conditions to allow perturbations to escape both along and across the direction of the jet outflow.

For the three models we have assumed that the jet has an initial top-hat, circular cross section, and that it travels in the $+z$ direction. The ionizing photon source is placed at a position $(x_s, y_s, z_s) = (-1.73\,\mathrm{pc}, 0, 0)$, and is taken to have $S_* = 10^{48}$ s^{-1}, emitting as a black body with $T_{eff} = 31000$ K. It is furthermore assumed that the optical depth (to

TABLA 5.1: Parameters of the numerical models

Model	v_j (km s^{-1})	r_j (10^{15}cm)	n_j (cm^{-3})	n_{env}[a] (cm^{-3})	Δ[b] 10^{14}(cm)
M1	200	3	500	10	2.5
M2	200	3	3000	10	3.5
M3	200	3	3000	10	12.0

[a]density of the undisturbed environment
[b]grid spacing along the three axes

ionizing photons) between the source and the jet is negligible. For the three models, the jet is initially neutral, at a temperature T_j = 1000 K, and the surrounding, undisturbed environment is fully ionized (the temperature and ionization fraction of the environment rapidly adjusting to the photoionization balance with the impinging radiation field).

Model M1 has been computed with the parameters that we have chosen for HH 444 (see section 5.3.1). As discussed in section 5.3.3, for these parameters the jet becomes progressively photoionized by an R-type ionization front. Models M2 and M3 have been computed with a higher initial density, which ensures that the ionization front is D-type starting from the point at which the jet emerges into the photoionizing field.

Figures 5.3 and 5.4 show the flow stratification (on the xz-plane) obtained for model M1 for integration times t = 20 and 40 yr, respectively. In Figure 5.3, we see the oblique ionization front (only partially developed in the z-direction) with its associated temperature and ionization fraction gradients. There is no density jump, confirming the fact that the front is R-type. In Figure 5.4, the ionization front is now fully developed and has reached a steady configuration which is preserved for longer integration times. The jet is fully ionized for $z > 2.2 \times 10^{16}$ cm.

Also shown in Figure 5.4 is the projection on the xz-plane of the shape of the ionization front obtained from equation 5.4. For this comparison, we have computed d_s and d_{rec} (equations 5.3.2- 5.3.2) assuming a temperature T_I = 8000 K, which is characteristic of the ionized region of the jet beam in the numerical simulation (see Figure 5.9). We find that the analytic and numerical positions for the ionization front agree very well. In particular, the distance along the z-axis at which the jet becomes fully ionized in our numerical simulation (2.2 $\times$ 10^{16} cm, see above) is in very good agreement with the analytical one, $z_{fully\ ionized} = r_j d_{rec}/d_s = 2.16 \times 10^{16}$ cm (derived from equation 5.4 for $x = r_j$ and $d_s/r_j \gg 1$).
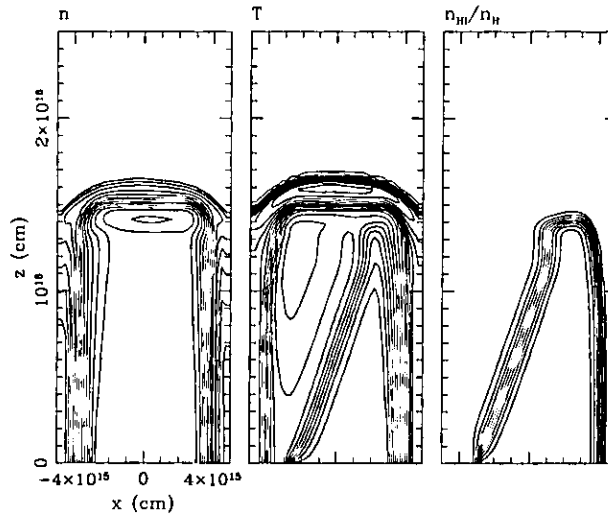
FIGURA 5.3: Number density (of atoms and ions), temperature and neutral hydrogen fraction stratifications obtained for model M1 after a $t = 20$ yr time integration (see the text). The density and temperature stratifications are depicted with $\sqrt{2}$, logarithmic contours, and the neutral fraction is shown with linear contours in steps of 0.1 .

Figure 5.5 shows the cross section of the jet beam at $z = 1.25 \times 10^{16}$ cm for an integration time $t = 40$ yr (by which the jet beam has reached a stationary state within the computational grid). In this figure, we also show a comparison with the analytic shape predicted for the ionization front, again obtaining a good agreement.

Figures 5.6 and 5.7 show the flow stratification (on the xz-plane) obtained for model M2 for integration times $t = 20$ and 50 yr, respectively. In this model, we see a slower penetration rate for the ionization front. Figure 5.8 shows the cross section of the jet beam at $z = 1.75 \times 10^{16}$ cm for an integration time $t = 40$ yr.

The differences and similarities between models M1 and M2 can be clearly seen in Figure 5.9, which shows density, temperature and neutral hydrogen fraction cuts along the $y = 0$ line through the jet cross sections depicted in Figures 5.5 and 5.8 (at $z = 1.25 \times 10^{16}$ cm for model M1 and at $z = 1.75 \times 10^{16}$ cm for model M2, respectively). For both models M1 and M2, we see that the $x > 0$ region of the jet beam is mostly neutral, while the $x < 0$ region has been photoionized. This effect is also seen in the temperature, which has values corresponding to a photoionized gas for $x < 0$, and values close to the initial jet temperature for $x > 0$. The flatter temperature distribution in the ionized region of model M2 reflects the absence of significant departure from photionization equilibrium in
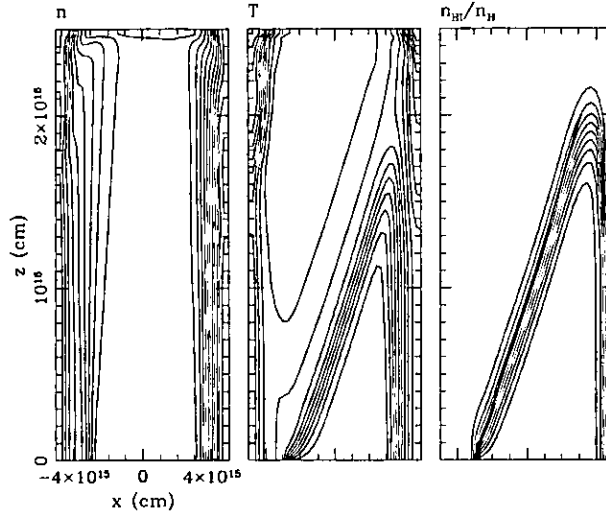
FIGURA 5.4: Number density (of atoms and ions), temperature and neutral hydrogen fraction stratifications obtained for model M1 after a $t = 40$ yr time integration (see the text). The density and temperature stratifications are depicted with $\sqrt{2}$, logarithmic contours, and the neutral fraction is shown with linear contours in steps of 0.1 . In the neutral hydrogen fraction contour map, we also show the shape for the ionization front predicted from the analytic model (thick line, see equations 5.4 - 5.3.2).

this model (the effects of the photon hardening within the ionization front having been neglected, see Raga et al. 1999).

The density stratification, however, shows important differences between models M1 and M2 (see figure 5.9). Model M1 has an almost uniform density across the beam cross section, which is consistent with the fact that the model has an R-type ionization front. The D-type front of model M2, however, produces a pre-compression of the neutral beam material (which appears as the "spike" around $x \approx 0$ in the n vs. x plot), and a decreasing density "photoionized wind" which leaves the surface of the ionization front (i. e., the monotonically decreasing density structure seen for $x < -5 \times 10^{14}$ cm in the top right plot of figure 5.9). We should note that in our low resolution numerical simulation, the D-type front of model M2 and its associated shock are only marginally resolved from each other.

Therefore, there are important dynamical differences between the passages of R-type or D-type fronts. In fact, the passage of a R-type front does not have very important dynamical effects, leaving the jet with density and velocity cross sections which closely resemble the initial cross section of the jet. On the contrary, the passage of a D-type front

FIGURA 5.5: Temperature (logarithmic, $\sqrt{2}$ contours) and neutral hydrogen fraction beam cross sections (linear, step of 0.1 contours) at a distance $z = 1.25 \times 10^{16}$ cm from the source, obtained for model M1 after a $t = 40$ yr time integration (see the text). On the neutral hydrogen fraction cross section, we also show the shape for the ionization front predicted from the analytic model (thick line, see equations 5.4-5.3.2).

FIGURA 5.6: Number density (of atoms and ions), temperature and neutral hydrogen fraction stratifications obtained for model M2 after a $t = 20$ yr time integration (see the text). The density and temperature stratifications are depicted with $\sqrt{2}$, logarithmic contours, and the neutral fraction is shown with linear contours in steps of 0.1 .
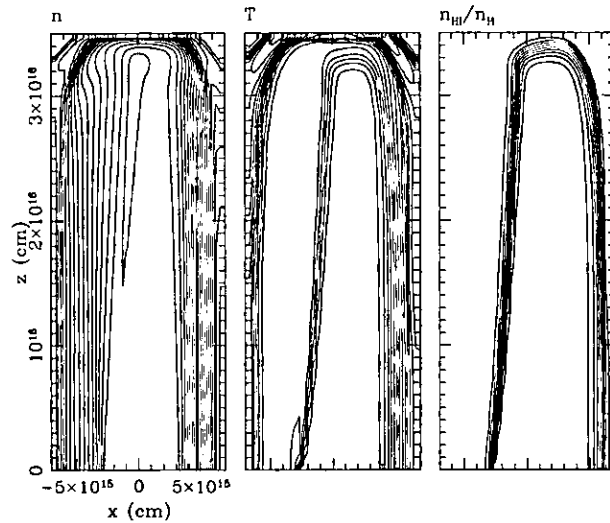
Figura 5.7: Number density (of atoms and ions), temperature and neutral hydrogen fraction stratifications obtained for model M2 after a $t = 50$ yr time integration (see the text). The density and temperature stratifications are depicted with $\sqrt{2}$, logarithmic contours, and the neutral fraction is shown with linear contours in steps of 0.1 .
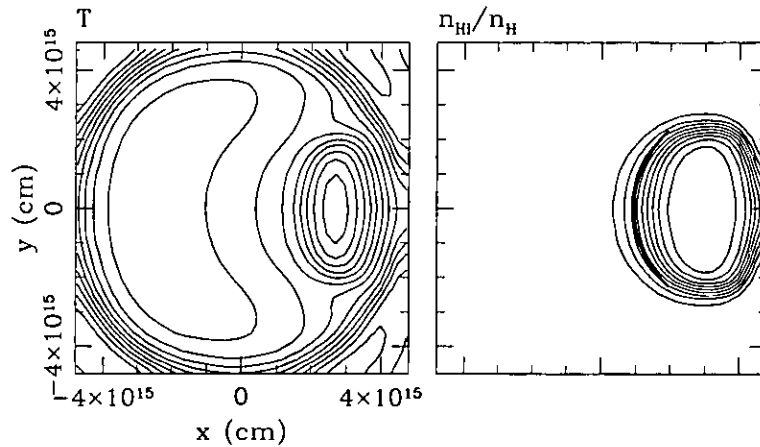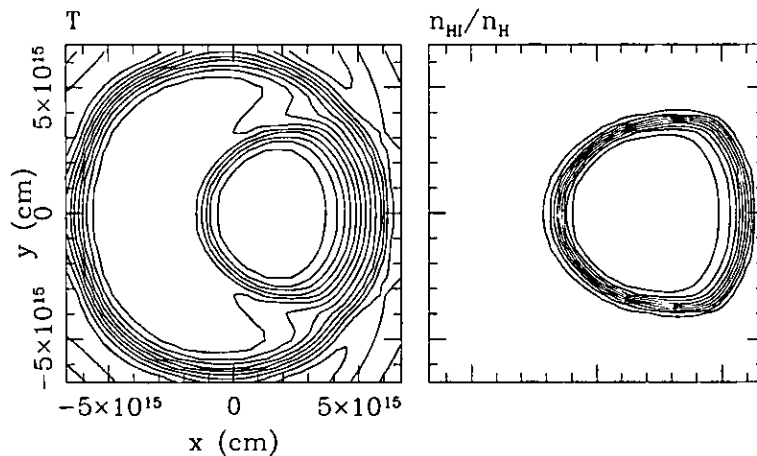

Figura 5.8: Temperature (logarithmic, $\sqrt{2}$ contours) and neutral hydrogen fraction beam cross sections (linear, step of 0.1 contours) at a distance $z = 1.75 \times 10^{16}$ cm from the source, obtained for model M2 after a $t = 50$ yr time integration (see the text).
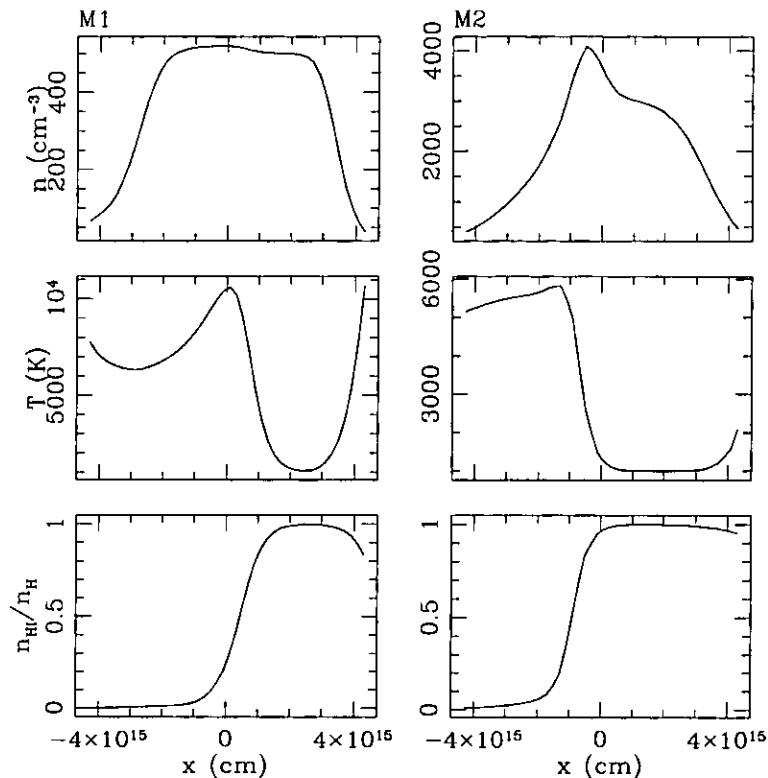
FIGURA 5.9: Temperature and neutral hydrogen fraction cuts along the $(x, 0, 1.25 \times 10^{16}\text{cm})$ line (model M1, left), and cuts along the $(x, 0, 3.0 \times 10^{16}\text{cm})$ line (model M2, right). The differences between the R-type ionization front case (model M1) and the D-type case (model M2) are clearly visible.

does have important dynamical effect, producing a more compressed, neutral region in the side of the jet beam directed away from the incident photon flux (i. e., the $+x$ direction in our simulations). This material is accelerated away from the photon source by the so-called "rocket effect" (see, e. g., the original paper of Oort and Spitzer 1955, and the discussion of section 5.3.3), which is due to the back reaction of the photoionized wind which is ejected towards the photon source. In this way, the passage of a D-type front produces a kind of "bifurcation" of the jet beam, with a lower density, photoionized region of the jet beam expanding towards the photon source, and a higher density, neutral region (which at large enough distances from the source eventually gets photoionized) being pushed away from the photon source.
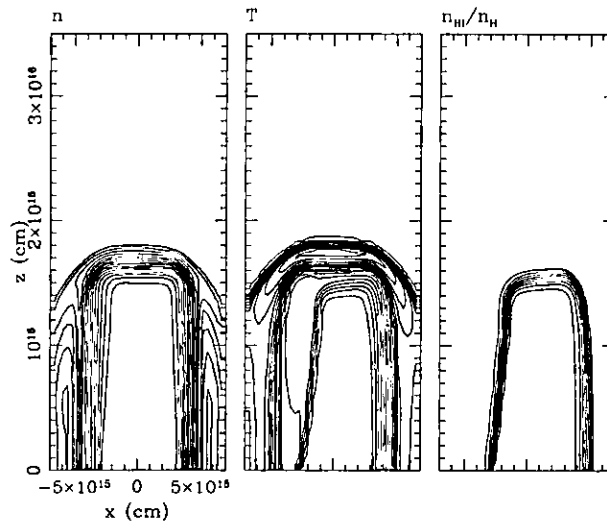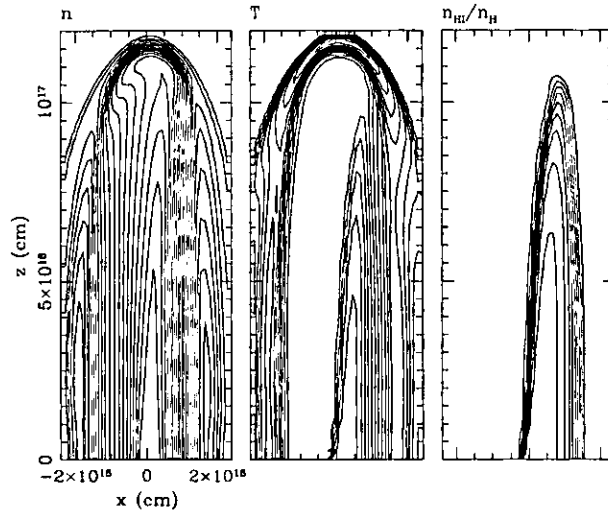
FIGURA 5.10: Number density (of atoms and ions), temperature and neutral hydrogen fraction stratifications obtained for model M3 after a $t = 180$ yr time integration (see the text). The density and temperature stratifications are depicted with $\sqrt{2}$, logarithmic contours, and the neutral fraction is shown with linear contours in steps of 0.1 .

This effect is seen in the stratification obtained from model M3 for a $t = 180$ yr time integration (see figure 5.10). This model has the same parameters as model M2, but has been computed at lower spatial resolution (see Table 5.4). From Figure 5.10, we see that there is a strong modification of the initial cross section of the jet, with the production of a dense, partially neutral core which curves in the $+x$ direction. This curvature of the jet beam should be directly observable.

Finally, we address the issue of the low resolution of our 3D numerical simulations. This could introduce problems particularly in model M2, in which the shock wave associated with the D-type front is not resolved spatially from the ionization front itself. Following the suggestion of the referee, we have computed a "steady jet" simulation for a jet with injection parameters identical to the ones of model M2. In such a simulation, one has to trace the position of the outer boundary of the jet, and impose a pressure condition at this jet beam/environment boundary. The equations of motion for the steady, supersonic region within the jet beam can then be marched in the z-direction with any standard gasdynamic algorithm.

For this purpose, we have modified the adaptive grid Coral code (described in detail by Mellema et al. 1998) in order to treat the steady jet problem. The Coral code includes

a detailed treatment of the ionization state of many ions, and a multi-frequency radiative transfer. With this code we have carried out an integration of the cross section of the jet downstream along the z-axis, assuming that the pressure exerted on the jet beam by the surrounding cocoon is negligible. This simulation is carried out on a 4-level, binary adaptive grid with a maximum spatial resolution of 5.5×10^{13} cm (which is approximately a factor of 6 higher resolution than the one of the 3D model M2). In Figure 5.11, we show the temperature and neutral H cross sections obtained for $z = 1.75 \times 10^{16}$ cm from this steady jet model.

From a comparison of this figure with the corresponding results from the 3D simulation of model M2 (Figure 5.8), we see that the position of the ionization front in both simulations agrees relatively well. The temperature stratification is somewhat different in the two models, since the steady jet calculation includes the hardening of the photons (see above and Mellema et al. 1998), which leads to higher temperatures in the ionized region close to the ionization front. Another difference between the two models is that the 3D simulation shows a more extended neutral region in the $+x$-direction (away from the ionizing photon source). This is a result of the fact that in the 3D simulation part of the cool cocoon left behind by the working surface recombines in the shadow of the jet beam (an effect which is absent in the steady jet model, in which the gasdynamic equations are integrated only for the region within the cross section of the jet beam). Also, the higher numerical diffusion of the low resolution, 3D model results in a broadening of the jet beam, which contributes to the more extended neutral region in the $+x$-direction, as well as to a larger extension in the $\pm y$-directions (see figures 5.8 and 5.11).

This comparison between the high resolution steady jet calculation and our 3D model M2 shows that the resolution of the 3D simulations appears to be adequate for obtaining a qualitatively correct description of the dynamics of a photoionized jet. This result allows us to proceed to study more complex problems in the future (e. g., the photoionization by an external photon source of a jet with "internal working surfaces") for which 3D simulations are clearly necessary.

5.5   Expected observational properties

As described in section 5.4, the passage of a D-type ionization front produces a clear asymmetry in the cross section of the jet beam, with a dense region which is deflected away from the ionizing photon source. This effect should be clearly visible as a side-to-side asymmetry of the region of the jet close to the source (the detection of which would involve a clear spatial resolution of the jet diameter), and as a deflection of the jet at larger distances from the source (with respect to the direction defined by the base of the jet)
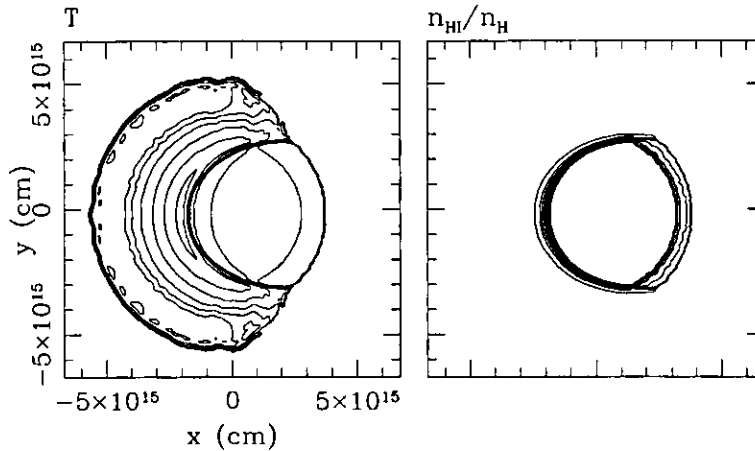
FIGURA   5.11: Temperature (logarithmic, $\sqrt{2}$ contours) and neutral hydrogen fraction beam cross sections (linear, step of 0.1 contours) at a distance $z = 1.75 \times 10^{16}$ cm from the source, obtained from a steady jet model (with zero environmental pressure) with injection parameters identical to the ones of model M2 (see the text).

away from the photon source. The latter effect should be clearly visible in ground based CCD images of the jet.

Interestingly, the HH 444 jet does show a curvature away from the direction pointing outwards from σ Orionis. The angle α between the axis defined by the knots within $\sim 20''$ of V 510 Ori and the line joining this star with condensation H (the "head" of the HH 444 jet, see Reipurth et al. 1998) has a value $\alpha \approx 4°$. It is, however, not possible to estimate the true deflection angle of the jet, as we do not have the information necessary to deproject α. Even though it is tempting to try to interpret the deflection of the HH 444 jet as a result of the existence of a D-type ionization front within the jet, we feel that such an interpretation would be premature, particularly since other HH jets (which are not embedded in H II regions) show comparable deflections.

Even more, from the parameters which have been estimated for HH 444 (see section 5.3.1 and Reipurth et al. 1998) one deduces that HH 444 probably has been photoionized by an R-type ionization front. As discussed in sections 5.3.2 and 5.4, this situation is less interesting from a dynamical point of view, as the ionization front does not alter the jet density and velocity cross sections in a significant way.

However, the passage of an R-type ionization front through the beam of a jet opens an interesting observational possibility. As there is still no conclusive model for the formation

and initial propagation of HH jets, it is not clear what is the "initial" cross section of the observed flows. For example, one could naïvely expect the jet cross section to have higher on-axis densities and/or velocities. It is of course difficult to measure such jet axis to jet limb gradients due to the fact that HH jets generally have subarcsecond diameters. Future spectroscopic observations with the Hubble Space Telescope could detect axis-to-edge gradients, but might have insufficient spectral resolution to settle the matter. As far as we are aware, the only detections of an axis-to-edge radial velocity gradient have been obtained for the somewhat chaotic HH 46/47 jet (which has a beam diameter of a few arcseconds, see Hartigan et al. 1993), and for the jet from DG Tau (obtained at high spatial resolution with the Canada-France-Hawaii telescope by Lavalley et al. 1997).

For a jet which is photoionized by the passage of an R-type front through the jet beam, it would actually be easier to observe a jet axis-to-edge radial velocity gradient in the following way. For example, for the parameters of HH 444, our models predict that the ionization front will have photoionized the full jet beam only at a distance of $\approx 2 \times 10^{16}$ cm away from the source (see Figure 5.4), corresponding to an angular distance of $\approx 3''$. If we put a spectrograph slit along this region, close to the jet source we will only see the emission from the photoionized edge of the jet, and at larger distances from the source the central region of the jet will start to be revealed by the passage of the ionization front. Therefore, if the central region of the jet has a higher velocity than the edges of the jet beam, we would observe an acceleration (in the radial velocity) as we move away from the source along the spectrograph slit. Such an observation could be used to deduce the velocity profile of the jet cross section.

Other interesting observational signatures of the passage of an ionization front through the beam of a jet could be found through an analysis of emission line ratios (which should show contributions from the fully photoionized region of the jet beam, and from the material within the ionization front itself). It will be interesting to attempt to carry out comparisons of low resolution spectra of photoionized jets with future, more detailed models (considering several atoms and ions in order to be able to make detailed predictions of the emission line spectrum).

5.6   Conclusions

In the last few years, increasing observational evidence has been found for the existence of HH jets within photoionized regions. In this paper, we have started to carry out a theoretical study of the properties of such jets.

In particular, we have calculated analytic and numerical models of an initially neutral jet that emerges into the surrounding nebula, and becomes ionized by the radiation from

the ionizing star of the nebula. We find that the impact of the passage of the ionization front through the jet beam on the gasdynamics is very different depending on the nature of the ionization front. A fast, R-type ionization front will have almost no effect on the gasdynamics of the jet, while a slow, D-type ionization front will have important structural and dynamical effects.

From the parameters found for HH 444 (the jet from V 510 Orionis, see Reipurth et al. 1998), we deduce that the ionization front going through this jet is probably R-type. In this situation, the jet velocity cross section is slowly revealed (but not modified) by the passage of the ionization front, so that the central (and possibly faster) region of the jet beam is only visible at distances of the order of a few arcseconds away from the source. This should be observed as a rapid "acceleration" in high resolution, long-slit spectra of this jet.

In future papers, we will present detailed comparisons between theoretical predictions from our models and observations of HH jets embedded in photoionized regions.

References

[1] Bertoldi, R., McKee, C., 1990, ApJ, 354, 735

[2] Cantó, J., Raga, A. C., Steffen, W., Shapiro, P., 1998, ApJ, 502, 695

[3] Dyson, J. E., Williams, D. A., The Physics of the Interstellar Medium (Cambridge Univ. Press), p. 70

[4] Hartigan, P., Morse, J. A., Heathcote, S., Cecil, G., 1993, ApJ, 414, L121

[5] Lavalley, C., Cabrit, S., Dougados, C., Ferruit, P., Bacon, R., 1997, A&A, 327, 671

[6] Mellema, G., Raga, A. C., Cantó, J., Lundqvist, P., Balick, B., Steffen, W., Noriega-Crespo, A., 1998, A&A, 331, 335

[7] O'Dell, C. R., Hartigan, P., Bally, J., Morse, J. A., 1997, AJ, 114, 2016

[8] Oort, J. H., Spitzer, L., 1955, ApJ, 121, 6

[9] Raga, A. C., Mellema, G., Arthur, S. J., Binette, L., Ferruit, P., Steffen, W., 1999, RMxAA, 35, 123

[10] Reipurth, B., Bally, J., Fesen, R. A., Devine, D., 1998, Nature, 396, 343

[11] Reyes-Ruiz, M., López, J. A., 1999, ApJ, 524, 952

[12] Rosado, M., Esteban, C., Lefloch, B., Cernicharo, J., García, R. J., 1999, AJ, 118, 2962

Capítulo 6

Análisis cinemático de HH 444

En los capítulos 4 y 5 analizamos la fotoionización de objetos Herbig-Haro (HH) que se encuentran embebidos en regiones H II. Como vimos, estos objetos nos dan la oportunidad de poder "ver" la base del chorro que es fotoionizada por el campo radiativo de una fuente externa (ver figura 6.1). Desarrollamos analíticamente cómo es el paso del frente de ionización por estos chorros y sus implicaciones dinámicas.

Cuando el chorro emerge de la sombra del disco asociado con la estrella, la radiación ultravioleta de la fuente externa ionizará las partes más externas. En este instante, el chorro consiste en un núcleo neutro y una capa externa ionizada. Debido a la incidencia del campo de radiación ionizante es posible llegar a una situación en que el chorro está totalmente ionizado (ver ecuación 4.10) si el frente de ionización es capaz de atravesar el chorro (ver capítulo 5).

Si el material del chorro es eyectado a velocidad constante, nosotros detectaremos este material a la velocidad proyectada correspondiente sobre la línea de vista. Sin embargo, si la velocidad de eyección del material tiene un cierto perfil a lo largo de una sección de material, lo que tendremos es que, a medida que nos alejamos de la fuente central, estaremos viendo zonas más internas del chorro con distinta velocidad, de manera que veremos reproducido el perfil de velocidad de la eyección del material en el diagrama posición-velocidad. Con un análisis cinemático de la base del chorro podemos detectar este perfil y extraer información sobre parámetros de la eyección del material como la velocidad de eyección, variabilidad temporal o no, etc.

Se ha observado que en algunos de estos chorros fotoionizados se detectan varios nudos a lo largo del eje del chorro (ver figura 6.1). Por analogía con los chorros "normales" en los que se han encontrado movimientos propios de los nudos, uno esperaría que en los chorros fotoionizados, estos nudos también los tuvieran. A través de la cinemática de estos nudos
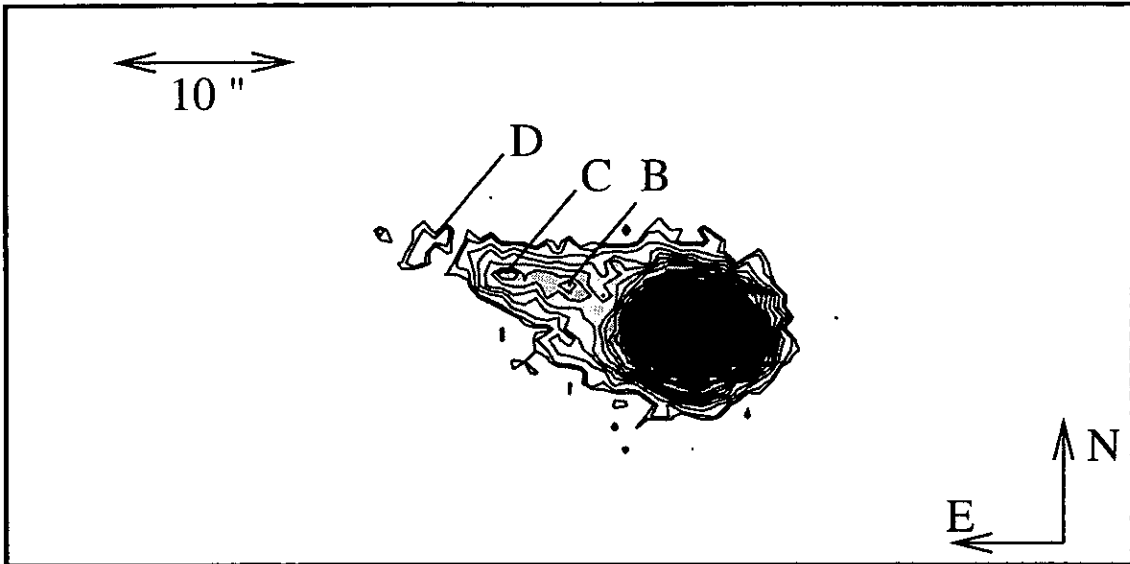
FIGURA 6.1: Detalle de la base del chorro HH 444 de una imagen Hα tomada en el telescopio de 2.1 m del OAN en San Pedro Mártir con PUMA en imagen directa. Sobre la imagen están señalados los nudos B, C y D siguiendo la nomencaltura de Reipurth et al. (1998).

también es posible extraer información sobre las condiciones de la eyección del material.

6.1   Posición de las superficies de trabajo

Un aspecto importante a destacar es la presencia en HH 444 de varias superficies de trabajo localizadas a distancias cada vez mayores de la fuente central (Reipurth et al. 1998). La detección de estas superficies de trabajo sugiere una eyección episódica de material. Un análisis simple de la posición de estas superficies de trabajo nos puede ayudar a estimar los parámetros de la eyección del material.

Podemos imaginar que el proceso de pérdida de masa tiene una dependencia temporal y tratar de encontrar qué variabilidad es la necesaria para producir las características observadas en distintos objetos.

Las diferentes parcelas de material que son eyectadas a distintas velocidades en algún momento se alcanzan unas a otras, generando superficies de trabajo internas. A través de las observaciones uno puede determinar la distancia entre dos superficies de trabajo
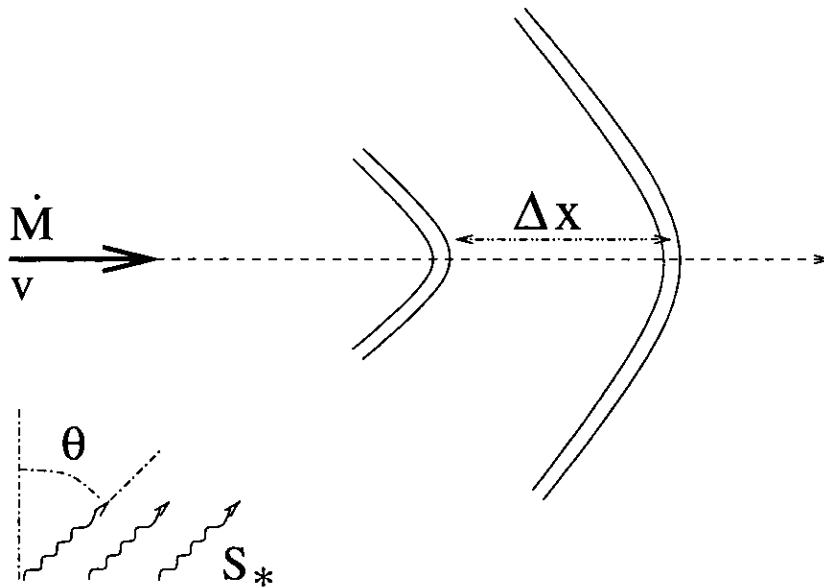
FIGURA 6.2: Esquema de chorro con varias superficies de trabajo

consecutivas, Δx (ver figura 6.2), de forma que si conocemos la velocidad promedio de la eyección del material, v_0, es posible estimar el período de estas eyecciones de masa como :

$$\tau = \frac{\Delta x}{v_0} . \tag{6.1}$$

En principio, no es conocida la forma de la variabilidad de la velocidad de eyección del material que estaría asociada al mecanismo físico que la origina. Supongamos una variación sinusoidal en la velocidad de eyección de material :

$$u_0(t) = v_0 + \Delta v_0 \sin\left(\frac{2\pi t}{\tau}\right) , \tag{6.2}$$

donde u_0 es la velocidad de eyección del material en cada instante, v_0 es la velocidad promedio de la eyección de material, Δv_0 es la amplitud de la variación de la velocidad de eyección, y τ es el periodo de eyección. Si $\Delta v_0 << v_0$, el primer nudo aparece a una distancia de la fuente central :

$$x_c = \frac{v_0^2 \tau}{2\pi \Delta v_o} . \tag{6.3}$$

A través de las observaciones podemos medir la distancia x_c, y si además se ha podido estimar la velocidad promedio del chorro, v_0, podemos utilizar las ecuaciónes 6.1 y 6.3 para establecer el período, τ, y la amplitud Δv_0 de la variabilidad de la velocidad de eyección (ver la ecuación 6.2).

Estos parámetros se han determinado para el objeto HH 444 a través de las imágenes directas y de espectroscopía de alta resolución. Se han utilizado estos parámetros para simular numéricamente como es la evolución temporal de la eyección de material con ayuda del código hidrodinámico "yguazú". Se presentan en el siguiente capítulo los diagramas posición-velocidad que se predicen de las simulaciones numéricas y se comparan con los obtenidos de la espectroscopía de alta resolución obtenida con el Manchester Echelle Spectrograph en el telescopio de 2.1 m del OAN en San Pedro Mártir (Baja California, México).

Con toda esta información, y comparando el diagrama posición-velocidad observado con el predicho por las simulaciones numéricas, determinamos los parámetros característicos de la eyección del material que mejor ajustan, tanto el período como la amplitud de la variabilidad de la eyección.

Así mismo, se observa una disminución en la intensidad de la emisión de Hα al aumentar la distancia de la fuente central, esto es exactamente lo contrario de lo que uno esperaría en la ionización si el material eyectado tuviera densidad uniforme. La explicación de este fenómeno que consideramos más plausible es que el material se eyecta con un cierto ángulo de apertura, de manera que la densidad decaiga al alejarse de la fuente central, y por lo tanto, disminuya la intensidad de la emisión en Hα.

Otro parámetro que hay que tener en cuenta es el ángulo que forman el eje del flujo y el plano del cielo. Con la información cinemática obtenida de la espectroscopía de uno de los choques de proa, podemos determinar la velocidad radial máxima y mínima. Con estos valores podemos utilizar la expresión dada por Hartigan et al. (1987) para determinar esta orientación, suponiendo que el material sobre el que viaja el choque está en reposo.

Con la combinación de todos estos parámetros, presentamos en el siguiente capítulo, tanto el diagrama posición-velocidad observado como el predicho por las simulaciones numéricas, y podemos ver que sí se reproducen las características principales de este chorro fotoionizado.

Capítulo 7

The structure and kinematics of the HH 444 photoionized jet in the σ Orionis region

L. López-Martín[1], A. C. Raga[1],
J. A. López[2] & J. Meaburn[3]

[1]*Instituto de Astronomía, UNAM, Ap. 70-264, 04510 D. F., México*
[2]*Instituto de Astronomía, UNAM, Ap. 877, 22800 Ensenada, B. C., México*
[3]*Astronomy Department, University of Manchester, Chesire SK11 9DL, UK*

in preparation

7.1   Abstract

HH 444 is a stellar jet which is immersed in the H II region photoionized by σ Orionis. Spatially resolved, high spectral resolution observations of the Hα and [N II] λλ6548, 6584 lines have been obtained for this object. These observations reveal for the first time the detailed velocity structure of the stellar jet and its associated bow-shock. The line profiles are modeled with gasdynamic numerical simulations, using a 3D code that also includes the transfer of the ionizing radiation from an external source (i. e., σ Orionis for the case of HH 444). In order to reproduce the observed characteristics of the line profiles, we find that an axially peaked initial velocity profile for the jet and a non-zero initial opening angle

for the flow with a time-variable ejection velocity is required. With these three ingredients we can reproduce the observed "acceleration" of the material along the jet beam, the rapid Hα intensity drop for increasing distances from the source, and the knotty structure of the jet, respectively.

Key words:ISM: jets and outflows — echelle spectroscopy — Hydrodynamics — Shock waves — individual: HH444

7.2   Introduction

The discovery of jets with Herbig-Haro type characteristics in the σ Orionis region (Reipurth et al. 1998) has prompted investigations on the photoionization of a neutral jet by an external source (Raga et al. 2000). Similar cases of HH jets immersed in an H II environment have also been found in the Orion nebula (O'Dell & Bally 2000).

In typical HH jets the emission only comes from the regions of the beam which are excited by shocks whereas the beams of externally photoionized jets are composed mainly of emitting material. This qualitative difference makes the photoionized jets especially interesting, since in these objects we can directly observe most of the material that participates in the outflow. For this reason, studies of the interplay between the jet dynamics and an external photoionization source are a subject of considerable interest.

Raga et al. (2000) carried out analytic and numerical studies of an initially neutral jet which emerges from the circumstellar region into an environment that is being photoionized by an external source. For objects such as those in the σ Orionis region the ionization front simply "unveils" the jet beam, and has no important dynamic effects (as the front is a highly supersonic, R-type front).

In order to further test the physical conditions of photoionized jets, in this paper we present long-slit echelle observations of the HH 444 jet, which was studied with imaging and low resolution spectroscopy by Reipurth et al. (1998). We have obtained spatially resolved, high spectral resolution observations of the Hα and [N II] $\lambda\lambda$6548, 6584 lines, which are described in section 7.3. We then use these observations (together with the previous observational results of Reipurth et al. 1998) to derive the parameters of the HH 444 outflow (section 7.4). Finally, we use these parameters to compute gasdynamic models for this outflow, which we compare directly with the observations (section 7.5).
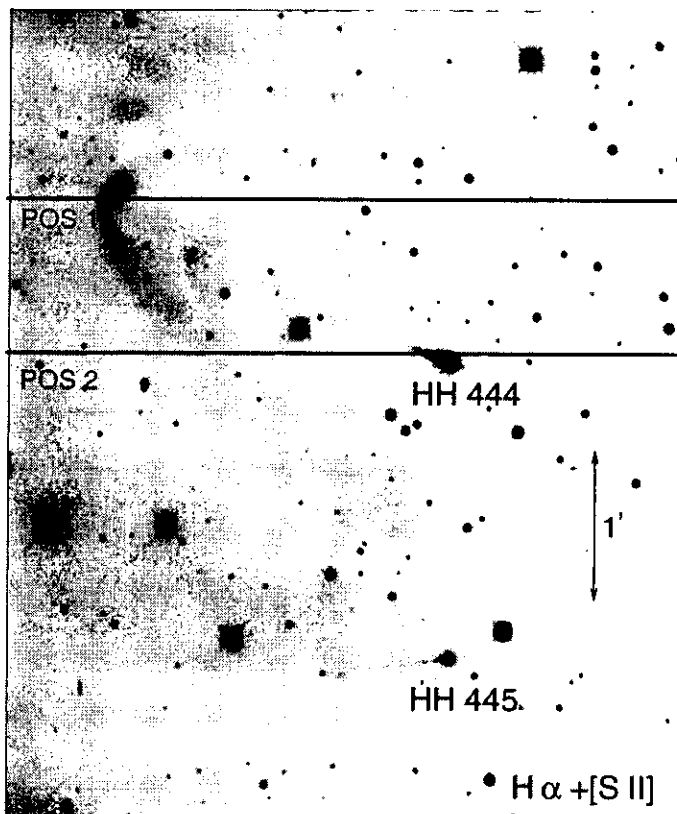
FIGURA 7.1: Image of the region with the HH444 and HH445 jets in the light of Hα + [S II] (Reipurth et al. 1998). The slit positions (POS 1 and POS 2) are marked with the two horizontal lines. North is to the top and East to the left.

7.3 Observations and Results

High resolution, long-slit spectra of the HH 444 outflow were obtained with the Manchester Echelle Spectrograph (MES; Meaburn et al. 1984), at the f/7.9 focus of the 2.1 m telescope of the OAN (the Observatorio Astronómico Nacional, at San Pedro Mártir). This spectrometer has no cross-dispersion. The detector was a Tektronix CCD with 1024 × 1024, 24 μm (0.3 arcsec) square pixels. A 2 × 2 pixel binning was employed in both the spatial and spectral dimensions. For the present observations, a filter of 90 Å bandwidth was used to isolate the Hα and [N II] $\lambda6584$ nebular emission lines. The spectra were calibrated to ± 1 km s^{-1} accuracy using a Th-Ar arc lamp.

Observations with two east-west slit positions were obtained, one covering the base of the jet, and the other one cutting through the main bow shock. The locations of the two slit positions are shown in Figure 7.1 on the Hα + [S II] image of Reipurth et al (1998).

Exposures of 1800 s were taken for each slit position. The "seeing" varied between 1 and 1.5 arcsec during the observations.

The Hα line profiles of the bow shock of the HH 444 jet are shown in Figure 7.2. We see that the line profiles have two peaks, which form two ridges in the position-velocity diagrams. The line emission is detected over a $\sim 15''$ region, and a total radial velocity range of ≈ 100 km s^{-1} is observed, with the more negative radial velocities corresponding to the central region of the bow shock.

The corresponding line profiles for the base of the jet are also shown in Figure 7.2. These position-velocity diagrams reveal a clear velocity gradient, with low radial velocities close to the star and increasingly negative radial velocities at larger distances, peaking at ~ -100 km s^{-1} at $\sim 10''$ to the E of the star. The Hα and [N II] λ6584 intensities first decrease with increasing distances from the source, and then show a rise to a strong peak at $\sim 10''$, where a clear well defined knot is observed along the jet. At larger distances from the source, the jet emission no longer falls along our east-west orientated spectrograph slit (see Figure 7.2).

7.3.1 The parameters for the HH 444

The physical parameters of HH 444 have been estimated by Reipurth et al. (1998). Following these autors, we assume a distance to σ Orionis of 400 ± 50 pc. The projected separation between the source of the HH 444 jet (V 510 Ori) and σ Orionis then has a value of ≈ 1.73 pc.

The ionizing source (σ Orionis) actually is a multiple star with an 09.5 star as the brightest component. We assume for this star an effective temperature $T_{eff} = 31000$ K and a total production rate of ionizing photons $S_\star = 10^{48}$ s^{-1}.

Reipurth et al. (1998) obtain an electron density of ≈ 200 cm^{-3} for the jet beam from the red [S II] line ratio. Following Raga et al. (2000), we assume a somewhat higher $n_j = 500$ cm^{-3} density for the base of the jet. The observed angular diameter of this jet is of ≈ 1 ", corresponding to a $r_j = 3 \times 10^{15}$ cm jet radius.

From the spectrum of the bow-shock of HH 444 (see Figure 7.2) it is possible to estimate the maximum and minumum radial velocity and with them we calculate the orientation angle ϕ between the outflow axis and the plane of the sky (Hartigan et al. 1987), giving a value of $\approx 40°$ assuming that the material is outflowing into a stationary medium. Using this orientation angle and the maximum (i. e., more negative) observed radial velocities,
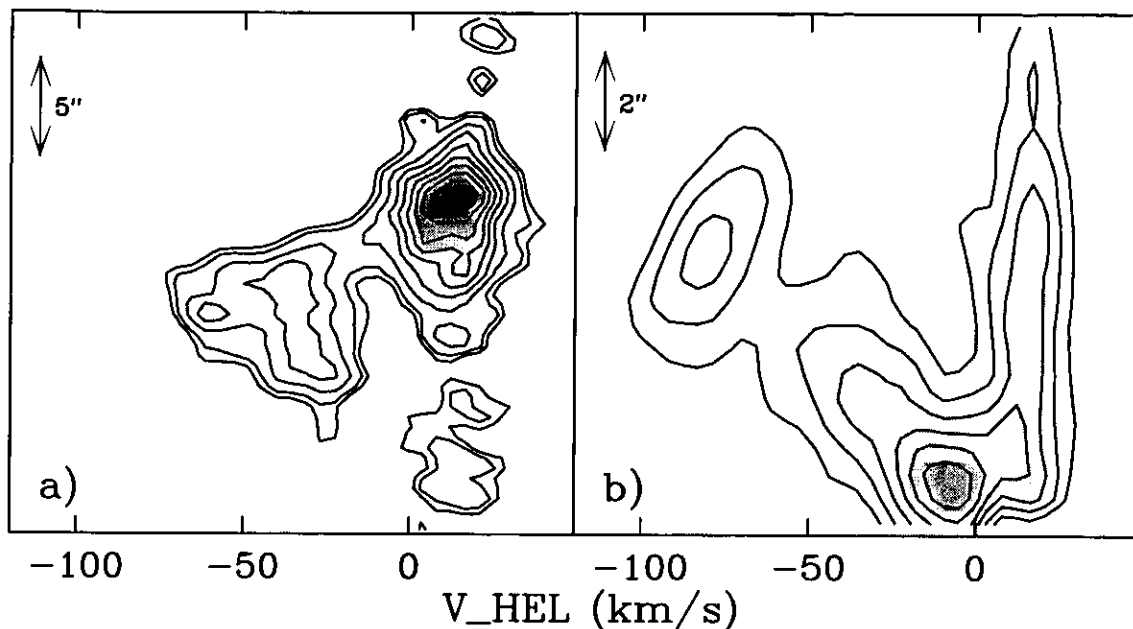
FIGURA 7.2: Contour map, (with linearly spaced contours) of the Hα position-velocity map, a) for the POS1 slit (see Figure 7.1) over the bow-shock of HH 444. Most of the nebular emission from the H II region has been substracted, b) for the POS2 slit (see Figure 7.1) over the base of HH 444. Most of the nebular emission from the H II region and the stellar continuum have been substracted.

we obtain a $v_j = 125$ km s^{-1} jet velocity for HH 444.

7.4 A model for HH 444

We have computed numerical models of an initially neutral jet emerging into an ionizing radiation field with the new "yguazú" code, which is described in detail by Raga et al. (1999). This 3D code integrates the gasdynamic equations, a rate equation for neutral hydrogen, and the radiative transfer of the ionizing radiation (at the Lyman limit). The radiative cooling is computed with a simple, parametrized approximation to the real, non-equilibrium cooling. The models have been computed in a uniform, Cartesian grid of $N_x \times N_y \times N_z = 40 \times 40 \times 100$ grid points. The ionizing photon source is placed at a position $(x_s, y_s, z_s) = (-1.73\,\text{pc}, 0, 0)$. The jet is assumed to be initially neutral, and the surrounding, undisturbed environment is fully ionized. For the jet beam we impose an
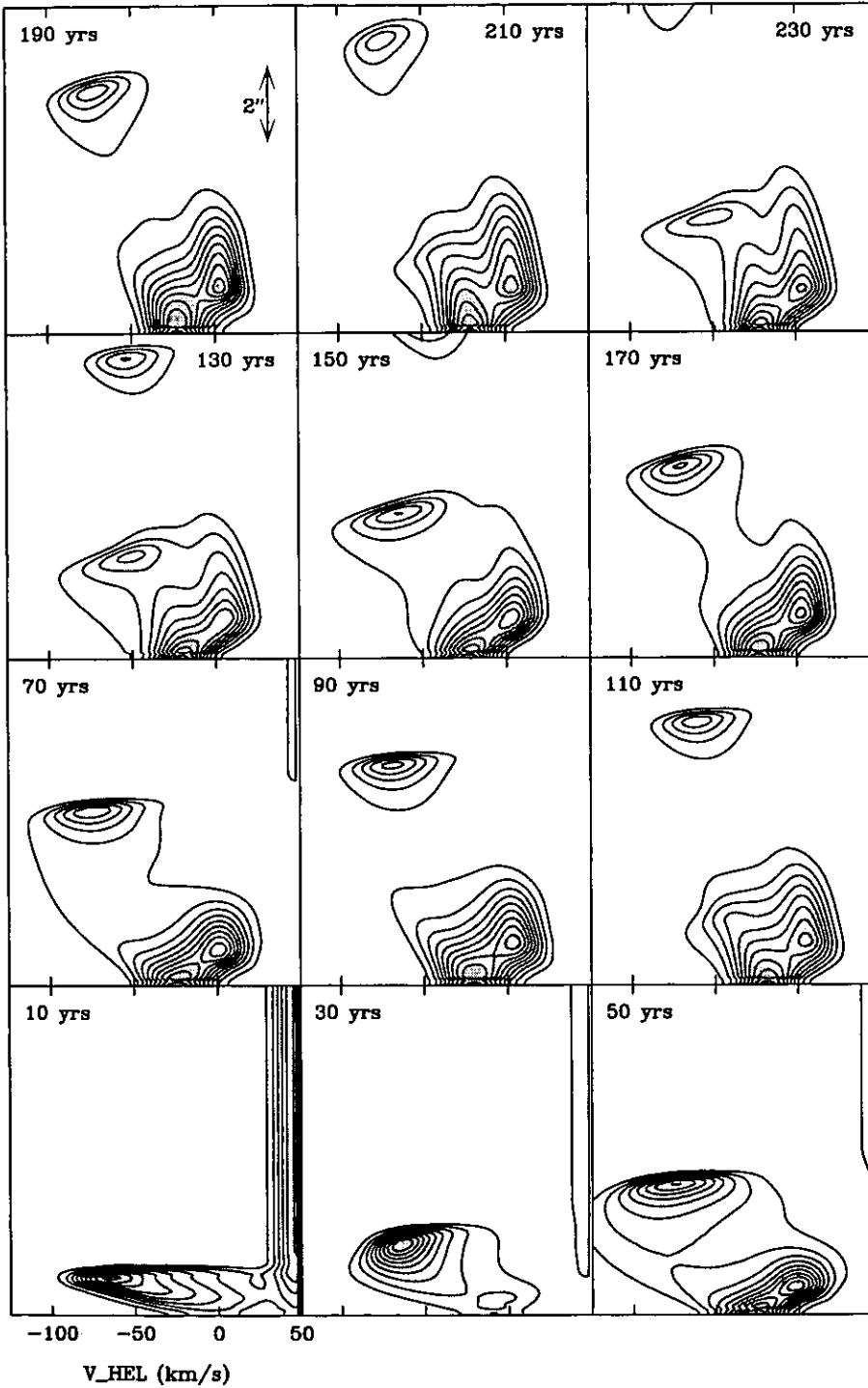
FIGURA 7.3: Time series of the Hα position-velocity diagrams predicted from the model of
HH 444 with a centrally peaked ejection velocity cross section, a time-dependent ejection
velocity and a non zero initial opening angle described in section 7.4. The time series starts
from the bottom of the figure with time intervales marked in each panel.
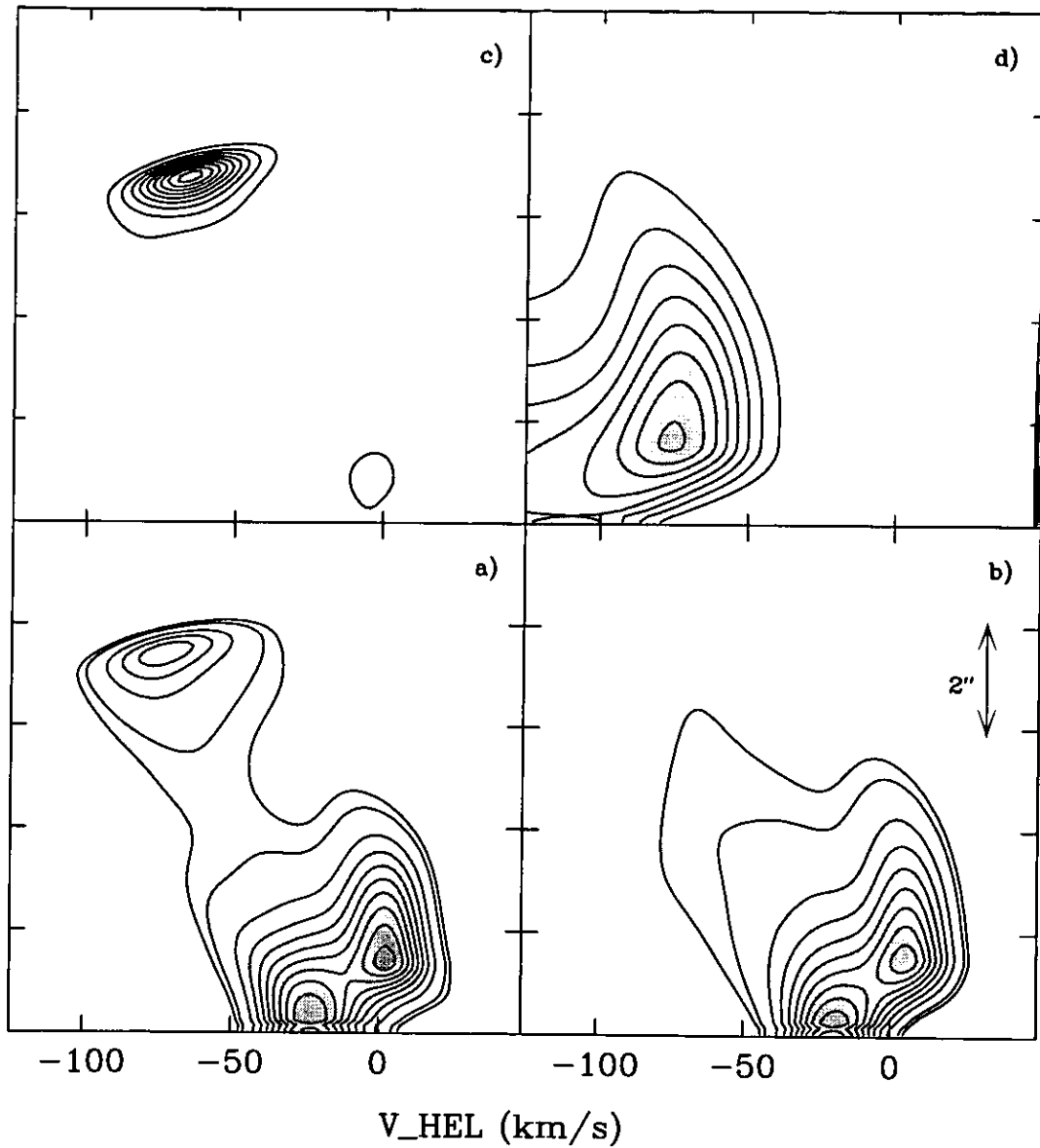
FIGURA 7.4: Contour map, (with lineraly spaced contours) of the Hα position-velocity map, with an integration time of 190 yrs. a) with a centrally peaked ejection velocity cross section, a time-dependent ejection velocity and a non zero initial opening angle, b) with a zero amplitude of the velocity variability, c) with a zero initial opening angle, d) with a top-hat ejection velocity cross section.

initial, top-hat density and temperature profile with $n_j = 500$ cm^{-3} and $T_j = 1000$ K, and for the environment we assume a density $n_{env} = 10$ cm^{-3} and $T_{env} = 10000$ K.

We find that in order to reproduce the observed Hα position-velocity diagram of the HH 444 jet, we need a model with the following ingredients :

A quadratic, centre-to-edge velocity profile, with a maximum on-axis velocity $v_0 = 275$ km s^{-1} and a minimum velocity $v_0 = 10$ km s $^{-1}$ at the edge of the jet beam. This centre-to-edge velocity profile is necessary for reproducing the observed acceleration (with increasing distances from the source) in the Hα position-velocity diagram of the HH 444 jet.

We then modulate the ejection velocity cross section with a sinusoidal time variability of the form :

$$u_0(t) = v_0 \left[1 + 0.3 \, \sin \left(\frac{2\pi t}{100 \, \text{yr}} \right) \right] . \tag{1}$$

This velocity variability produces knots with intensities and positions similar to the ones observed along the HH 444 jet,

We impose an initial full opening angle of 40° for the jet beam. This opening angle is necessary for reproducing the observed drop in the Hα intensity with increasing distance from the source.

In Figure 7.3, we show a time series of the Hα position-velocity diagrams predicted from this model. In order to compute these diagrams, we have assumed an angle of 40° (away from the observer) between the plane of the sky and the outflow axis. From this figure, we see that at different evolutionary times we do obtain structures that resemble the Hα position-velocity diagram of HH 444 (see Figure 7.2). For example, in agreement with the observations we obtain a two spatially extended components : a low velocity component, and a high velocity, accelerating component. We also obtain a third, decelerating component at distances of a few seconds of arc from the source, which corresponds to the emission from the head of the jet (at early times of the simulations) or from an internal working surfaces (at later times). This component is also seen in the observations as the first knot along the HH 444 jet.

In order to test the revelance of the different ingredients of our model, we have also computed models in which we omit some of the features described above. In Figure 7.4, we compare the results from models :

b) a model in which we have set the amplitude of the velocity variability to zero. This

model does produce the low and high (accelerating) velocity components, but does not have the knot observed at $\sim 5''$ from the source in HH 444,

c) a model in which we have set the initial opening angle to zero. In this model, the resulting position-velocity diagram is completely dominated by the emission from the internal working surface, and the base of the jet is barely visible,

d) a model in which we have imposed a top-hat ejection velocity cross section. In this model, the jet emission appears at a more or less constant radial velocity as a function of position, not reproducing at all the acceleration observed in the HH 444 position-velocity diagrams.

Comparison of these models show that a centrally peaked ejection velocity cross section with a time-dependent ejection velocity and a non-zero initial opening angle (panel a) in Figure 7.4) produces the best fit to the observations of the HH 444 jet.

7.5 Conclusions

We have obtained $H\alpha$ position velocity diagrams of the base of the HH 444 jet, and of its main bow shock (see Reipurth & Bally 1998). From the line profiles of the main bow shock, we deduce an orientation angle of 40° between the outflow axis and the plane of the sky.

We also present a first comparison between predictions obtained from a 3D numerical simulation, in which the radiative transfer of the ionizing radiation from σ Orionis is included, and the long-slit spectra of the photoionized HH 444 jet.

In the best-fit model, the jet beam is gradually unveiled by the passage of an oblique ionization front driven by the ionizing radiation from σ Orionis. If we assume that the jet beam has an axially peaked velocity profile, this unveiling produces an acceleration of the emission in the predicted position-velocity diagrams, which we find is in qualitative agreement with the observed acceleration of the position-velocity diagrams of the HH 444 jet.

If we assume that the ejection velocity has a sinusoidal time variability, we produce internal working surfaces along the jet. We find that these internal working surfaces have signatures in the predicted position-velocity diagrams which resemble the line profile of the first emitting knot along the HH 444 jet.

Finally, we find that in order to reproduce the observed decrease in the $H\alpha$ intensity with increasing distances from the source, and the correct relative intensity between the

base of the jet and the first emitting knot, we find that it is necessary to impose an initial opening angle of 40° for the jet beam.

References

[1] Hartigan, P., Raymond, J. & Hartmann, L. 1987, ApJ, 316, 323

[2] López-Martín, L., Raga, A. C., López, J. A. & Meaburn, J. 2000, RMxAC, 9, 230

[3] Meaburn, J., Blundell, B., Carling, R., Gregory, D. E., Keir, D. F., & Wynne, C. G. 1984, MNRAS, 210, 463

[4] O'Dell, C. R. & Bally, 2000. RMxAC, 9, 194

[5] Raga, A. C., Mellema, G., Arthur, S. J., Binette, L., Ferruit, P. & Steffen, W. 1999, RMxAA, 35, 123

[6] Raga, A. C., López-Martín, L., Binette, L., López, J. A., Cantó, J., Arthur, S. J., Mellema, G., Steffen, W. & Ferruit, P. 2000, MNRAS, 314, 681

[7] Raga, A. C., López-Martín, L., López, J. A. & Meaburn, J. 2000, RMxAC, 9, 191

[8] Reipurth, B., Bally, J., Fesen, R. A. & Devine, D. 1998, Nature, 396, 343

Capítulo 8

Eyecciones colimadas en nebulosas planetarias: el caso de M 2-48

8.1 Morfología de nebulosas planetarias

La presencia de flujos altamente colimados en nebulosas planetarias (NPs) es cada vez más frecuente en las observaciones de este tipo de objetos. Algunas veces, simplemente se observan un par de nudos de alta velocidad (como en NGC 7009 o NGC 6826), pero otras veces se observan estructuras más extendidas y más complejas (por ejemplo NGC 6445, ver figura 8.1, KjPn 8, etc.).

En general no podemos decir que haya dos nebulosas planetarias con el mismo aspecto, pero sí hay grupos de ellas que tienen suficientes similitudes como para poder incluirlas en diferentes grupos en una clasificación morfológica. Una de las clasificaciones morfológicas que se ha usado con frecuencia es la propuesta por Stanghellini et al. (1993), que distingue entre elípticas (E) (incluyendo a las esféricas), bipolares (B), de simetría de punto (P), e iregulares (I). Además de esta letra, se le añade una M si tiene múltiples capas, o S si muestra estructuras internas como nudos o filamentos. En algunas ocasiones las morfologías observadas en diferentes filtros (Hα, [N II], [O III], etc.) no coinciden (ver figura 8.1), revelando estas diferencias información sobre los mecanismos generadores de las estructuras.

Además de conocer las diferentes morfologías que pueden presentar los objetos en los diferentes filtros, es importante poder determinar cual es el cociente de intensidad entre las diferentes líneas de emisión nos da información sobre el mecanismo de ionización. De esta forma, cuando encontramos un cociente alto de [S II]/Hα, podemos pensar que estamos detectando regiones de gas chocado. Este gas chocado, en el caso de las nebulosas planetarias,
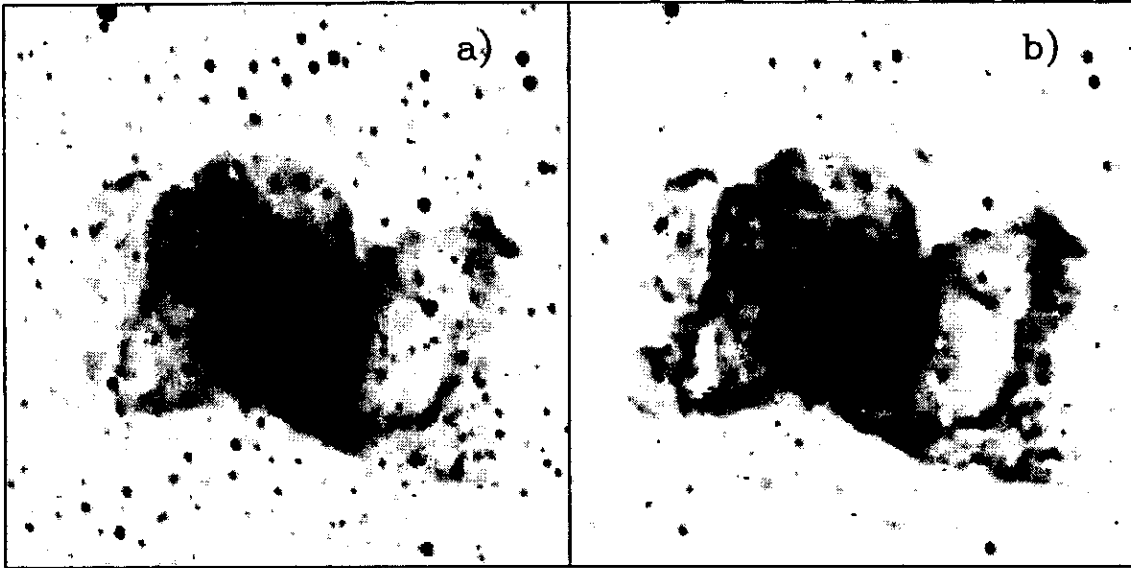
FIGURA 8.1: Imágenes tomadas en los filtros de [N II] y Hα (a) y b) respectivamente) de NGC 6445 en el telescopio de 2.1 m del OAN en San Pedro Mártir.

generalmente es la interacción de un viento rápido con un viento lento que fue eyectado con anterioridad. Es la simetría de este viento rápido la que puede estar determinando la morfología de las estructuras que vemos como choques de proa. Por ejemplo, si tenemos un viento rápido que es mucho más denso en el ecuador que en los polos, nos encontraremos con una estructura bipolar cuya colimación (que podemos determinar a través del cociente de los ejes mayor y menor de los lóbulos bipolares) estará en función del perfil de densidad. Se ha acudido a diferentes fenómenos físicos para explicar estos perfiles de densidad, desde rotación estelar o campos magnéticos estelares (García-Segura 1997) hasta la presencia de sistemas binarios (Reyes-Ruiz et al 1999, Soker & Livio 1989). Este esquema había sido bastante aceptado por diferentes autores, pero cada vez hay más razones para pensar que este mecanismo no explica satisfactoriamente muchas morfologías observadas en las NP.

8.2 Eyección colimada en M 2-48

En el catálogo de nebulosas planetarias galácticas del hemisferio norte de Manchado et al. (1996) encontramos imágenes en los filtros Hα, [N II] y [O III] de la NP M2-48 (PN G 062.4-00.2; $\alpha_{2000} = 19 : 50 : 28, \delta_{2000} = +25 : 54 : 28$). Esta NP está clasificada como
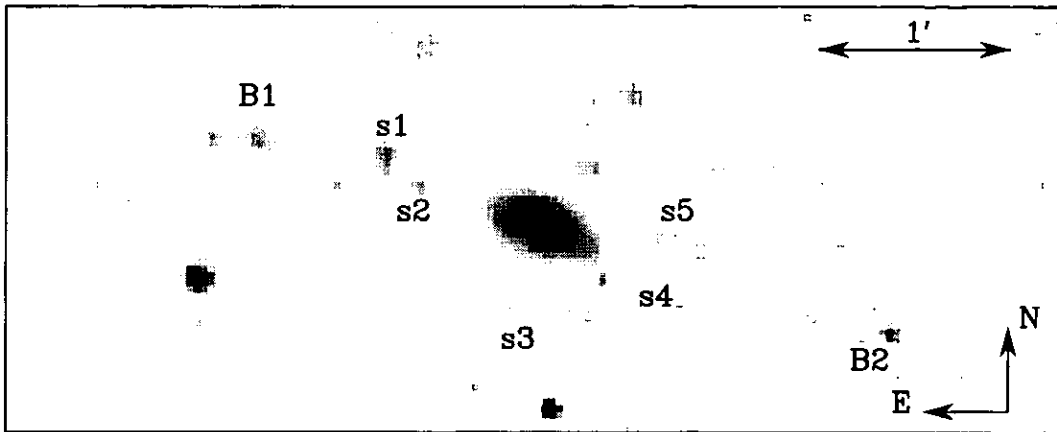
FIGURA 8.2: Imagen en [N II] de M 2-48, en la que podemos apreciar los nudos brillantes alrededor del núcleo bipolar (s1-s5) y los choques de proa simétricos a ambos lados del mismo (B1 y B2).

bipolar y se encuentra muy cerca del plano galáctico. En la imagen en [N II] del catálogo se puede apreciar una estructura con aspecto de choque de proa a $\approx 20''$ al N y $\approx 1'$ al E del núcleo bipolar. Esta estructura despertó nuestro interés y decidimos incluir al objeto dentro de una campaña de observación en el telescopio de 2.1 m del OAN en San Pedro Mártir (Baja California, México).

Sorprendentemente encontramos que, además de estar constituida por un núcleo bipolar, esta NP consta de una "cáscara" externa a este núcleo, y a unos $2'$ aparecen dos estructuras con morfología de choques de proa, B1 y B2, (ver figura 8.2, la nomenclatura seguida es la que se describe en Vázquez et al. 2000, ver siguiente capítulo) situadas simétricamente respecto del núcleo. Una serie de nudos de material ionizado parecen estar trazando la "cáscara" alrededor del núcleo bipolar, s1-s5. Un detalle interesante es que esta "cáscara" no es concéntrica con el núcleo bipolar. Una primera explicación que proponemos para interpretar este fenómeno es que es debido al movimiento propio de la estrella central, de manera que desde el momento en que se generó la cáscara (que podría ser en la etapa AGB) y la bipolaridad, la estrella hubiera cambiado en posición desde el centro de la "cáscara" hasta el centro del núcleo bipolar. Un pequeño cálculo utilizando datos típicos de las velocidades de expansión encontrados en estas cáscaras ($v_{exp} \approx 10$ km s^{-1}, Kwok 1993), nos da como resultado una velocidad de la estrella central del orden de 5 km s^{-1}, que parece ser un valor razonable. Otra posible explicación es que el medio en el que se eyectó el viento de la AGB que da lugar a la "cáscara" tuviera una estratificación en

la densidad (con la densidad disminuyendo de N a S). Esta explicación seía consistente con el hecho de que B1 esté más próximo al centro de la "cáscara" y más intenso que la contraparte, B2.

También podría ser que la velocidad de eyección del material no sea isotrópica, pero entonces tendríamos que pensar en algún mecanismo físico que generara esa anisotropía. De esta forma, encontramos varias explicaciones sencillas y razonables para que los lóbulos bipolares y la "cáscara" estén descentrados.

Uno de los nudos brillantes de material ionizado, s1 (ver figura 8.2), parece tener morfología de choque de proa. Nosotros estamos proponiendo que este nudo pueda ser el resutado de la interacción de una eyección colimada de material con la "cáscara" en expansión. Para verificar esta hipótesis es importante determinar la edad cinemática tanto de la "cáscara" como de los choques de proa. Si suponemos una velocidad típica de expansión de la "cáscara" de unos 10 km s^{-1}, podemos estimar su edad cinemática, $\tau_{cascara} \approx 3 \left[\frac{d}{kpc} \right] \times 10^4$ años. Esta edad es la que uno esperaría de un remanente de la etapa AGB. De la misma forma, podemos estimar la edad cinemática de los choques de proa B1 y B2, suponiendo una velocidad típica de los chorros de unos 100 km s^{-1}, obteniendo $\tau_{B1} \approx 5.7 \left[\frac{d}{kpc} \right] \times 10^3$ años. Es decir, con este cálculo sencillo podemos deducir que la eyección del chorro es un fenómeno mucho más reciente. De esta forma, parece plausible la interpretación de que el nudo brillante sea una interacción del chorro colimado y la "cáscara" en expansión.

Otro detalle al que debemos prestar atención es el hecho de que si trazamos una línea que una a los choques de proa B1 y B2, ésta no es paralela al eje de los lóbulos bipolares. Esto puede ser el reflejo de que, por un lado, ambos fenómenos se generaron en distintos instantes, y por otro, que el eje de simetría ha cambiado entre ambos eventos.

Presentamos en el siguiente capítulo las observaciones de esta NP, así como un análisis de las estructuras encontradas y una discusión acerca de la historia evolutiva de esta NP.

Capítulo 9

Bow-shocks and possible Jet-shell interaction in the Planetary Nebula M 2-48

R. Vázquez[1], L. López-Martín[2], L. F. Miranda[3], C. Esteban[4], J. M. Torrelles[5], L. Arias[2] & A. C. Raga[2]

[1]*Instituto de Astronomía, UNAM, 22860 Ensenada, B. C., México*

[2]*Instituto de Astronomía, UNAM, 04510 Cd. Universitaria, D. F., México*

[3]*Instituto de Astrofísica de Andalucía, CSIC, 18008 Granada, Spain*

[4]*Instituto de Astrofísica de Canarias, 38200 La Laguna (Tenerife), Spain*

[5]*Institut d'Estudis Espacials de Catalunya and Instituto de Ciencias del Espacio (CSIC), 08034 Barcelona, Spain*

9.1 Abstract

Deep narrow band CCD images in the Hα, [OIII] λ5007 Å, [NII] λ6584 Å, and [SII] λ6717 + 31 Å emission lines have been obtained for the planetary nebula M 2-48. The discovery of a pair of symmetric low-excitation bow-shocks, separated by 4′, and forming a highly collimated bipolar outflow, is presented. The bow-shocks are emitting in [OIII] and present

the ionization structure expected from working surfaces of collimated jets, pointing out that these structures are tracing regions with shocked gas at high velocities ($> 100\,km\,s^{-1}$). In addition, an internal bipolar outflow ($60'' \times 30''$) and an apparent off-center semi-circular shell (size $\approx 110''$) are also detected. An enhancement of low-excitation line emission is observed in the shell along the outflow axis. This result can be interpreted in terms of a jet-shell interaction.

keywords : ISM : jets and outflows – planetary nebulae: individual: M 2-48

9.2   Introduction

In the last few years, observations of Planetary Nebulae (PNe) have shown new morphologies shaped by microstructures. These observations have modified our knowledge on the formation and evolution of the PNe (e.g. Miranda & Solf 1992; Balick et al. 1994; see López 1997 and Miranda 1999 for reviews). M 2-48 (PN G 062.4-00.2); α_{2000}=19:50:28, δ_{2000}=+25:54:28) is a bipolar ($60'' \times 30''$) Planetary Nebula (PN), whose morphology seems to contain such microstructures. In fact, in the IAC Catalog of PNe (Manchado et al. 1996), we note the presence of a remarkable structure located at a distance of $\approx 60''$ from the central star and oriented almost along the major axis of the nebula (PA$\sim 70^o$). Although this structure is faint, it looks like a bow-shock with the concave side facing the central star. This structure, which is clearly observed in [NII], is weaker in Hα, and apparently absent in [OIII], suggests the existence of a collimated outflow . The possible presence of a bow-shock in M 2-48 presents great interest. Collimated outflow components in PNe appear as compact knots or elongated filaments (e.g., López, Meaburn & Palmer 1993; Miranda 1995; Corradi et al. 1996; Hajian et al. 1997; Guerrero, Vázquez & López 1999), but bow-shocks are very rare, and only some cases have been recognized by means of spectroscopic observations (e.g., Schwarz 1992; Solf 1994; López et al. 1997).

In this paper we show deep CCD narrow-band images in the light of Hα, [NII], [OIII], and [SII], carried out in order to study in detail the nebular structure and, in particular that of the bow-shock. Our data reveal new aspects of M 2-48 among which the detection of an extended and highly collimated nebular structure, the presence of bow-shocks and the possible interaction of this collimated structure with a circular shell, are the most outstanding results.

9.3 Observations and results

A first set of deep narrow-band images of M 2-48, in the light of Hα (15 Å HPBW), [OIII] λ5007 Å (25 Å HPBW) and [NII] λ6584 Å (19 Å HPBW) were obtained in 1998 July 9, with the 2.2-m telescope at Calar Alto Observatory[1], using the Calar Alto Faint Object Spectrograph (CAFOS). A Loral CCD with 2048 × 2048, 15 μm (0.33 arcsec) square pixels was the detector. Exposure times were 1800 s in each filter. 'Seeing' varied between 1.3 and 1.5 arcsec during the observations. Images were reduced in the standard manner using IRAF and they are shown in Fig. 9.1. The small boxes show contour plots of the internal structure as seen in each filter.

A second set of images in the light of Hα (20 Å HPBW), [OIII] λ5007 Å (10 Å HPBW), [NII] λ6584 Å (10 Å HPBW) and [SII] λ6724 Å (20 Å HPBW) were obtained in 1999 May 20 and 22, with the 2.1-m UNAM telescope at the San Pedro Mártir Observatory[2], using the UNAM Scanning Fabry-Pèrot Interferometer (PUMA; Rosado et al. 1995) in its direct image mode. Exposure times ranged from 600 to 1500 s. A Tektronix CCD with 1024 × 1024, 24 μm (0.6 arcsec) square pixels, was used in the binning modes 1, 2, and 4. In this case, 'seeing' varied from 1 to 1.5 arcsec during the observations. Combinations of images in all these modes, giving a 4-binned final image for each filter (2.4 arcsec per pixel), are presented in the image mosaic of Fig. 9.2. In these images, the field was partially star-cleaned, in order to better show the nebular structures. Stars were not removed if they were inmersed in, or close to, nebular emission regions. A contour map of the [NII] image is shown in Fig. 9.3 in which some of the most important morphological features are labeled.

The images in Figs. 9.1 and 9.2 reveal two bow-shock-like structures, labeled B1 and s1 (Fig. 9.3), towards the northeastern side of the main nebula (central region). s1 corresponds to the feature observed in the IAC Catalog (see below), whereas B1 has been detected in these images for the first time. B1 is located near the major axis of the main nebula at an angular distance of ≈ 2′ from the central star. Remarkably, it is detected not only in Hα and [NII], but also in [OIII] and [SII]. In all filters, the two "wings" of the bow-shock B1 can clearly be distinguished as well as an enhancement of the emission at the apex. Towards the shouthwestern side, a counterpart of B1, labeled B2, can be recognized in the Hα, [NII] and marginally in [OIII] by the presence of faint emission "wings". Unfortunately, a bright star at the position of the expected apex of B2 prevents a complete view of this feature. The images also show that B1 and B2 are not isolated features but they are connected

---

[1]The Calar Alto Observatory is operated by the Max-Planck-Institut für Astronomie (Heidelberg) and the Spanish Comisión Nacional de Astronomía.

[2]The Observatorio Astronómico Nacional (OAN) is operated at the Sierra de San Pedro Mártir (México), by the Instituto de Astronomía, UNAM.
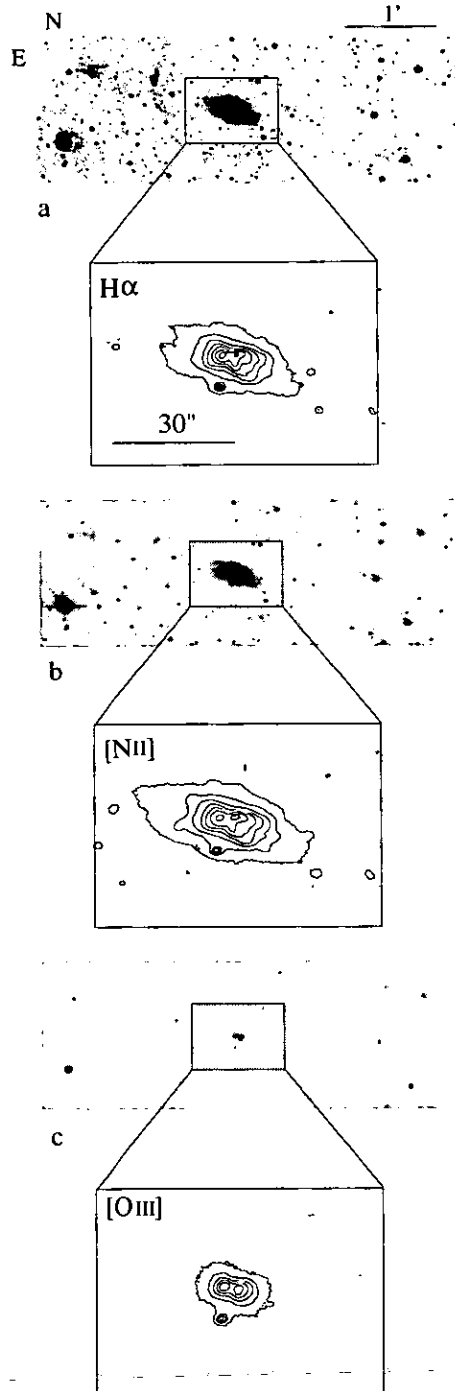
Figura 9.1: CCD images taken in the Calar Alto Observatory and contour plots from its central region taken in the light of: $H\alpha$ (a), [NII] $\lambda6584$ Å (b), and [OIII] $\lambda5007$ Å (c). Levels in contour plots correspond to differences of $\log \sqrt{2}$ in the relative intensity. North is up, and East is to the left.
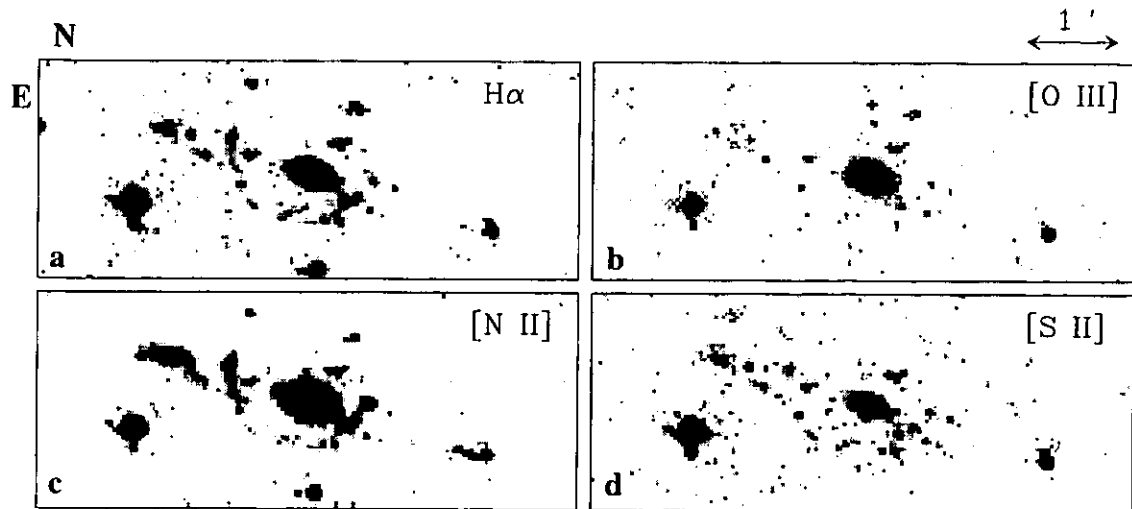
FIGURA 9.2: 4-binned images of M 2-48 in: Hα (a), [OIII] λ5007 (b), [NII] λ6584 (c), and [SII] λ6717 + 31 (d). North is up, and East is to the left.

to the main nebula by faint emission detected in Hα, [SII] and [NII]. In fact, this faint emission and B1–B2 trace two narrow and extended lobes, each with a collimation degree of $120''/30'' = 4$.

The feature s1 is located at $\approx 1'$ from the center and does not appear to have a counterpart towards the southwest. It corresponds to the isolated bow-shock-like structure observed in the images by Manchado et al. (1996). However, Fig. 9.2 shows that s1 is a part of a group of small emission clumps (s2, s3, s4, and s5, Fig. 9.3) and fainter nebular arcs whose spatial disposition traces an apparent off-center semi-circular shell of $\approx 110''$ in diameter. This feature is observed in Hα and [NII] and could be present in [SII], though very faint. In Fig. 9.3 we show an eye-fitting of this shell.

Finally, the main, internal structure of M 2-48 is a bipolar shell, $60'' \times 30''$ in size, consisting of two lobes separated by a faint region. The lobes appear to be open and connected with the extended and highly collimated lobes defined by B1–B2.

9.4 Discussion

Our deep images of M 2-48 have revealed the existence of three main structural components in this nebula: a pair symmetric bow-shocks located at the apex of two highly collimated bipolar lobes, an off-center semi-circular shell, and an internal bipolar structure.

The images suggest that B1 and B2 are of low-excitation. This is confirmed by the [NII] $\lambda6583$/Hα line intensity ratio of $\simeq 3$ obtained by Acker et al. (1992) for the bipolar shell and the relative intensity of the nebular components. In particular, a very strong [NII] emission in B1 and B2, compared with Hα, can be inferred from the images. In this respect, B1 and B2 present the low-excitation typically observed in collimated components in PNe (see references above). However, [OIII] emission is also detected, indicating that B1 and B2 correspond to high-velocity shocked regions ($V_s > 100\,\mathrm{km\,s^{-1}}$; Hartigan, Raymond & Hartmann 1987). Moreover, B1 is noticeably wider (perpendicular to the flow axis) in [OIII] than in [SII] and even in Hα. In addition, the "wings" of B1 are shorter (along the outflow axis) in [OIII] than in the other low-excitation emission (e.g. [SII]). These results agree with the ionization structure in a bow-shock in which one expects a high-excitation region around the apex surrounding a low-excitation region and a decrease of the excitation at large distances from the apex. From these comments we suggest that B1 and probably also B2 trace the working surfaces of highly collimated, high velocity bipolar jets.

The morphology of M 2-48 closely resembles that in other bipolar PNe such as M 1-16 (Schwarz 1992), He 3-1475 (Bobrowsky et al. 1995; Riera et al. 1995), or the features A1–A2 in KjPn 8 (López, Vázquez & Rodríguez 1995; López et al. 1997). In all these cases, high-dispersion spectroscopy indicate the presence of highly collimated outflows involving high-velocity shocks ($V_s > 200\,\mathrm{km\,s^{-1}}$). In particular, the bow-shocks A1–A2 in KjPn 8 also present enhanced [OIII] emission (López et al. 1995).

Another singular characteristic of M 2-4 is the presence of an apparent off-center semi-circular shell.

The images show that this shell is also of low-excitation. Moreover, enhancement of low-excitation emission is observed in the shell mainly along the major nebular axis and in regions apparently coinciding with the highly collimated lobes (Fig. 9.3). This suggests an interaction between the jet and the shell with s1, s2, s4, and s5 representing the contact zones and gives further support to that this apparent shell should be a real structure. Evidence for interaction between collimated outflows and shells has also been reported towards other PNe, such as NGC 6572 (Miranda et al. 1999), NGC 4361 (Vázquez et al. 1999) and NGC 6891 (Guerrero et al. 1999).

We propose a scenario in which the formation of the jets in M 2-48 was produced in a subsequent event, after the shell was expelled. Assuming the shell is a real structure, its larger radius, compared to the size of the main nebula, suggests that it could be related with mass loss through a slow wind in the AGB stage of the progenitor. Rough estimates for the kinematic age of the semi-circular shell and B1-B2 can be obtained. In the case of the shell, we assume an expansion velocity of $v_{shell} \sim 10\,\mathrm{km\,s^{-1}}$ which is typical of an AGB wind. The resulting kinematic age, $\tau_{shell} \simeq 3 \left[\frac{d}{\mathrm{kpc}}\right] \times 10^4\,\mathrm{yr}$ (where d is the distance in kpc)
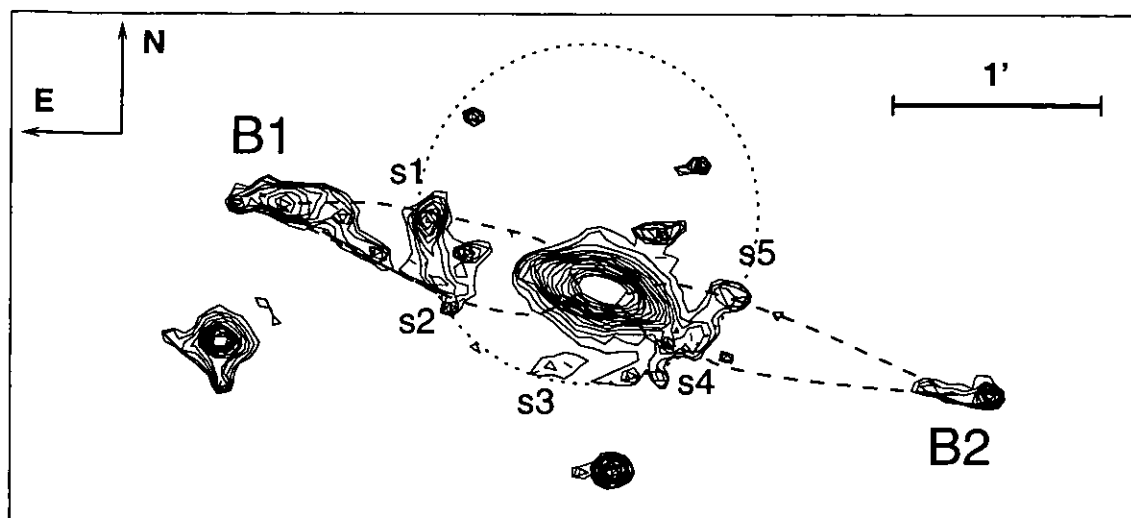
FIGURA 9.3: Contour plot of the [NII] emission of M 2-48. The main morphological features are labeled, and the structures are marked with dashed lines (the two lobes and the off-center semi-circular shell). The map has logarithmic levels separated each one by log 2. North is up, and East is to the left.

is the one expected for the remnant envelope of a AGB progenitor. This is a consequence of having set the velocity wind to a typical value for AGB stars. In the case of the jets, we assume that the ejection axis is perpendicular to the line-of-sight with a velocity $v_{jet} \geq 100\,\mathrm{km\,s^{-1}}$. Thus, the corresponding kinematic age is $\tau_{jet} \leq 5.7\left[\frac{d}{\mathrm{kpc}}\right] \times 10^3\,\mathrm{yr}$. A comparison between both kinematic ages suggest that if the semi-circular shell indeed represent the remnant envelope of an AGB progenitor then the ejection of the highly collimated outflow should be a much more recent event. In these circumstances, a jet-shell interaction appears plausible. For the inner bipolar shell no estimates of kinematic ages can be done. The possible relationships between the bipolar shell and the other nebular components, as well as their kinematics (specially for the apparent semi-circular shell), should be investigated by means of high resolution, spatially resolved spectroscopy.

9.5 Conclusions

Narrow band CCD images towards the PN M 2-48 were obtained, which reveal a pair of symmetric bow-shocks separated by $4'$ and probably related to a bipolar jet ejection. The bow-shocks exhibit the ionization structure expected if they trace the working surface

of highly collimated jets. An apparent off-center semi-circular shell (size $\approx 110''$) is also detected surrounding the internal bipolar shell of the object. There is an enhancement of low-excitation emissions in this structure along the major nebular axis. This result can be interpreted in terms of a jet-shell interaction.

References

[1] Acker, A., Ochsenbein, F., Stenholm, B., Tyłenda, R., Marcout, J. & Schohn, C., 1992, Strasbourg-ESO Catalogue of Galactic Planetary Nebulae, ESO, München

[2] Balick, B., Perinotto, M., Maccioni, A., Terzian, Y. & Hajian, A., 1994, ApJ 424, 800

[3] Bobrowsky, M., Zijlstra, A. A., Grebel, E. K., Tinney, C. G., Te Lintel Hekkert, P., Van de Steene, G. C., Likkel, L. & Bedding, T. R., 1995, ApJ 446, L89

[4] Corradi, R. L. M., Manso, R., Mampaso, A. & Schwarz, H. E., 1996, A&A 313, 913

[5] Guerrero, M. A., Miranda, L. F., Manchado, A. & Vázquez, R., 2000, MNRAS 313, 1

[6] Guerrero, M. A., Vázquez, R. & López, J. A. 1999, AJ 117, 967

[7] Hajian, A., Balick, B., Terzian, Y. & Perinotto, M., 1997, ApJ 487, 304

[8] Hartigan, P., Raymond, J. & Hartmann, L., 1987, ApJ 316, 323

[9] López, J. A. 1997, Jets and BRETs in Planetary Nebulae. In: Lamers H.J.G.L.M., Habing H.J. (eds.) Proc. IAU Symp. 180, Planetary Nebulae. Kluwer, Dordretch, p. 197

[10] López, J. A., Meaburn, J., Bryce M. & Rodríguez, L. F., 1997, ApJ 475, 705

[11] López, J. A., Meaburn, J. & Palmer, J., 1993, ApJ 415, L135

[12] López, J. A., Vázquez, R. & Rodríguez, L. F., 1995, ApJ 455, L63

[13] Manchado, A., Guerrero, M. A., Stanghellini, L. & Serra-Ricart, M., 1996, The IAC Morphological Catalog of Northern Galactic Planetary Nebulae, IAC, La Laguna

[14] Miranda, L. F., 1995, A&A 304, 531

[15] Miranda, L. F., 1999, Jets and Disks in Young Planetary Nebulae. In: Guenther E.W., Stecklum B., Klose S. (eds.) Optical and Infrared Spectroscopy of Circunstellar Matter. ASP Conf. Ser. Vol. 188, p. 257

[16] Miranda, L. F.& Solf, J., 1992, A&A 260, 397

[17] Miranda, L. F., Vázquez, R., Corradi, L. R. M., Guerrero, M. A., López, J. A. & Torrelles, J. M., 1999, ApJ 520, 714

[18] Riera, A., García-Lario, P., Manchado, A., Pottasch, S. R.& Raga, A. C., 1995, A&A 302, 137

[19] Rosado, M., Langarica, R., Cobos, F., Tinoco, S., Garfias, F., Tejada, C., Gutiérrez, L. & Le Coarer, E., 1995, Rev. Mex. Astron. Astrofis. Ser. Conf. 3, 263

[20] Schwarz, H. E., 1992, A&A 264, L1

[21] Solf ,J., 1994, A&A 282, 567

[22] Vázquez, R., López, J. A., Miranda, L. F., Torrelles, J. M. & Mcaburn, J., 1999, MNRAS 308, 939

Capítulo 10

Análisis cinemático de la nebulosa planetaria M 2-48

10.1   Estructura cinemática de la nebulosa planetaria M 2-48

En el capítulo 9 vimos que la NP M 2-48 tiene estructura externa al núcleo bipolar. A través de las imágenes directas en los filtros de Hα, [N II], [S II] y [O III] descubrimos que alrededor de éste núcleo bipolar tiene una serie de nudos brillantes que parecen trazar una "cáscara" circular. Uno de estos nudos (denominado s1 en Vázquez et al. 2000, a partir de aquí artículo I, ver figuras 8.2 y 9.3) tiene morfología similar a la de un choque a proa, y nosotros lo interpretamos como la interacción de la eyección colimada con esta "cáscara".

También observamos que a unos 2' del núcleo, simétricamente dispuestos, aparecen dos estructuras con morfología de choque de proa que interpretamos como una eyección colimada (B1 y B2 en el artículo I).

En el capítulo 8 vimos que podíamos estimar la edad cinemática de algunas de estas componentes suponiendo ciertos valores típicos de las velocidades tanto de expansión de la "cáscara" como del chorro. Con estas hipótesis pudimos deducir que la eyección del chorro es mucho más reciente que la "cáscara", estableciendo de esta forma, una secuencia de eventos en la nebulosa. A través de este tipo de análisis tratamos de reproducir la "historia" de las nebulosas, y de esta forma, conocer mejor cual es la evolución de este tipo de objetos.

Como podemos ver, para poder tener una mejor interpretación de los diferentes fenómenos ocurridos en esta nebulosa planetaria, es necesario tener información cinemática de las diferentes componentes, tanto para poder confirmar su naturaleza, como para poder analizar con más detalle su evolución. Para ello, se obtuvo espectroscopía de alta resolución con
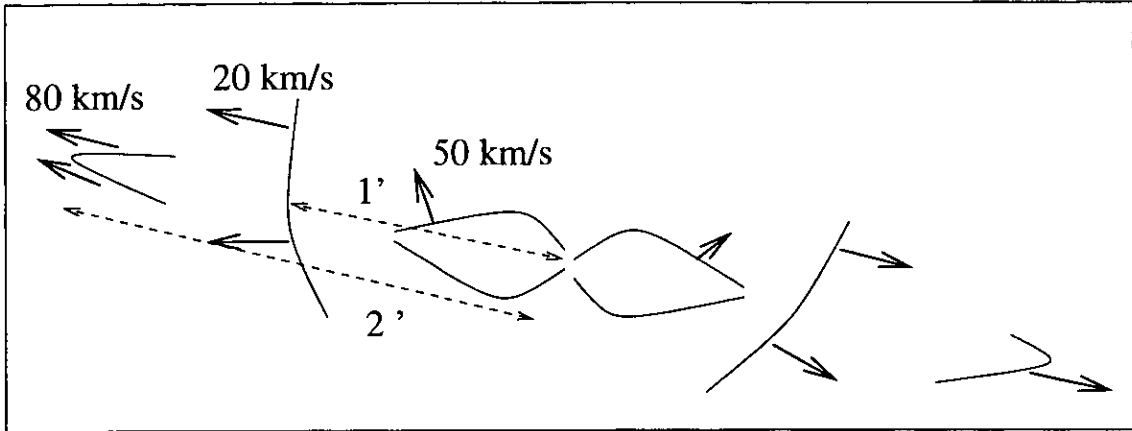
FIGURA 10.1: Diagrama esquemático de la NP M 2-48 con la velocidad radial heliocéntrica de sus principales componentes.

el MES en el telescopio de 2.1 m del OAN en San Pedro Mártir (Baja California, México). J. A. López y Jhon Meaburn obtuvieron espectros de rendija larga en siete posiciones (ver figura 11.3), que cubren los lóbulos bipolares, los nudos brillantes y los choques de proa.

Del resultado de los datos espectroscópicos encontramos las velocidades radiales de las distintas componentes de la nebulosa (ver figura 10.1). En primer lugar, se establece la presencia de un núcleo bipolar con una velocidad radial heliocéntrica de expansión de ≈ 50 km s^{-1} (ver figura 11.5). De esta forma podemos estimar la edad cinemática de este núcleo bipolar obteniéndose $\tau_{bipolar} \approx 3 \left[\frac{d}{kpc}\right] \times 10^3$ años. Si tomamos la distancia estimada por Cahn & Kaler 1971 de 1.6 kpc a la nebulosa planetaria, obtenemos una edad cinemática de los lóbulos bipolares de 4800 años.

Se encuentra que los nudos brillantes que rodean al núcleo bipolar tienen una velocidad radial de expansión de ≈ 20 km s^{-1}, y no encontramos emisión a esta velocidad entre ellos. Esto nos hace pensar que más que una "cáscara", como se había pensado en un principio, se trata de dos arcos en expansión lenta alejándose del núcleo bipolar. Además, pensamos que no se trata de una cáscara esférica de material en expansión porque en ese caso esperaríamos ver un círculo completo de material ionizado. Con esta velocidad podemos estimar la edad cinemática de estos arcos, $\tau_{arcos} \approx 2.4 \times 10^4$ años. Esta edad cinemática sigue siendo consistente con pensar en que estos arcos son un remanente de la etapa AGB. En este punto tenemos que tener cuidado pues no estamos teniendo en cuenta los efectos de proyección sobre las velocidades.

Encontramos también la velocidad radial del choque de proa B1 (ver figura 11.7), ≈ 80

km s^{-1}. Conocida esta velocidad radial podemos estimar la edad cinemática de este choque de proa, para el cual se obtiene un valor de $\tau_{B1} \approx 11.4 \times 10^3$ años.

Si analizamos las edades cinemáticas obtenidas anteriormente podemos establecer una serie de cosas. En primer lugar, que efectivamente el chorro es un evento mucho más reciente que los arcos, por lo que la propuesta de que el nudo s1 sea una interacción entre ellos parece bastante plausible. En segundo lugar, que la eyección colimada que dió lugar a los choques de proa fue anterior a la formación de los lóbulos bipolares. De esta forma podemos establecer una secuencia temporal de eventos en la nebulosa.

Si unimos el hecho de que la eyección del material colimado que da lugar a los choques de proa y de que la eyección que da lugar a la bipolaridad se produjeron en diferentes instantes y que, además, los ejes de ambas eyecciones no coinciden (ver Figuras 11.5 y 11.11), podemos pensar que nos encontramos ante el caso de un BRET (Bipolar Rotating Episodic Jet, ver López et al 1995).

Todo el análisis anterior se ha realizado en base a las velocidades radiales obenidas de los espectros. Ahora bien, desconocemos la orientación de estas estructuras con respecto al plano del cielo. Para poder determinar esta orientación hemos usado un modelo "3/2-D" para poder predecir los diagramas posición-velocidad de los choques de proa. Utilizamos un modelo "3/2-D" de choque de proa, y para calcular la emisión de Hα suponemos una dependencia con la velocidad de choque de la forma (Raga & Noriega-Crespo 1993) :

$$I_{\mathrm{H}\alpha} \propto (v_{shock})^{\alpha_{\mathrm{H}\alpha}} . \tag{10.1}$$

Estos autores encuentran que hay tres regímenes que corresponden a tres intervalos distintos de la velocidad del choque. Los choques de proa B1 y s1 se encuentran en dos regímenes distintos, los coeficientes respectivos $\alpha_{\mathrm{H}\alpha}$ son 2.04 y 3.49. Además debemos tener en cuenta la forma del choque de proa. Para el caso de los choques de proa de M 2-48, una parábola parece ajustar bastante bien a la morfología observada.

Del resultado de la comparación del diagrama posición velocidad observado y predicho por nuestros modelos obtenemos que el eje del choque de proa B1 se encuentra a un ángulo de $\approx -10^o$ con respecto del plano del cielo, y que s1 se encuentra a $\approx 10^o$. Este resultado nos dice que el objeto se encuentra muy cerca del plano del cielo, por lo que las velocidades radiales pueden llegar a verse aumentadas hasta en un factor casi de 5 para obtener las velocidades reales de las componentes.

Este hecho modifica las edades cinemáticas anteriormente calculadas peron o afecta a las edades relativas de los diferentes eventos ocurridos en la nebulosa.

En el siguiente capítulo damos una descripción más detallada de las observaciones realizadas, así como un análisis más profundo de la cinemática de las diferentes componentes

y una discusión acerca de la evolucíon del objeto, situándolo dentro del contexto de la evolución de las nebulosas planetarias.

Capítulo 11

Unveiling the structure of the planetary nebula M 2-48

L. López-Martín[1] C. Esteban[2], R. Vázquez[3]
A. C. Raga[1], L. F. Miranda[3], J. M. Torrelles[4]
L. Olguín[1] & J. Meaburn[5]

[1]*Instituto de Astronomía, UNAM, Ap. 70-264, 04510 D. F., México*
[2]*Instituto de Astrofísica de Canarias, 38200 La Laguna (Tenerife), Spain*
[3]*Instituto de Astronomía, UNAM, 22860, Ensenada, B. C., México*
[4]*Institut d'Estudis Espacials de Catalunya and Instituto de Ciencias del Espacio (CSIC), 08034 Barcelona, Spain*

in preparation

11.1 Abstract

The kinematic structure of the main features of the planetary nebula (PN) M 2-48, as well as their physical conditions, are revealed from high and low-dispersion spectroscopy. The nebula is formed by three main structures, namely, a bipolar central region (CR), a set of knots tracing two arcs surrounding the central region, and two symmetric bow-shocks. The central region shows a kinematic structure corresponding to a bipolar shell, with an expansion velocity of $\simeq 50\,\mathrm{km\,s^{-1}}$. The arcs appear to be expanding at $\simeq 20\,\mathrm{km\,s^{-1}}$, except in

the regions aligned with the bow-shocks, which are interpreted as jet-shell interaction zones at $\simeq 100\,\mathrm{km\,s^{-1}}$. Finally, the bow-shocks have uncorrected velocities of $\simeq 80\,\mathrm{km\,s^{-1}}$. An inclination angle of 10° with respect to the plane of the sky is estimated using simple bows-hock models. The physical conditions ($T_e \simeq 10^4\,\mathrm{K}$, $N_e \simeq 1000\,\mathrm{cm^{-3}}$ CR; $N_e \simeq 100\,\mathrm{cm^{-3}}$ other features) of the main features of the nebula, and the chemical abundances of the central region, are obtained, showing that M 2-48 is a Type I PN. With all these elements, a discussion about the possible formation scenario for this nebula and its importance in the context of outflow-shell interactions is presented.

Key words:ISM: jets and outflows — echelle spectroscopy — Hydrodynamics — Shock waves — planetary nebulae : individual: M 2-48

11.2   Introduction

The concept of what a planetay nebula is, has changed appreciably in the past few years. Observations of planetary nebulae (PNe) show non-spherical morphologies, including microstructures within the shells and highly collimated, high velocity jet-like components (Miranda & Solf 1992, López et al. 1995, López et al 1997, Bryce et al. 1997, O'Connor et al. 2000, Vázquez et al. 2000). The origin of such outflows remains as an important unsolved question, even when firm contributions in theoretical models have been made (e.g. Różyczka & Franco 1996, García Segura 1997, García-Segura et al. 2000, Reyes-Ruíz & López 2000).

M 2-48 is a PN which presents a pair of symmetric low-excitation bow-shocks, forming a highly collimated bipolar outflow (Vázquez et al. 2000, hereafter Paper I). Several knots in the sorroundings of the nebula were interpreted as a shell by these authors, and the high emission zones of the shell, aligned with the outflow, were related with a possible interaction between the bipolar outflow and the shell, giving to this nebula a time sequence of events.

In order to analyze the kinematic structure, physical conditions and chemical abundances of M 2-48, spatially resolved high and low dispersion spectroscopy has been obtained towards this PN. The results are discussed in the following sections.

11.3   Observations and Results

Low dispersion (LD) spectroscopy was obtained in 1999, July 18, 19 and 20, with the B&Ch spectrometer combined with the f/7.5 focus in the 2.1-m OAN telescope at the Sierra de San Pedro Mártir, B. C., Mexico . A 300 lines/mm grating was used with a Tektronix CCD 1024 × 1024 pixel, 24 μm square pixels (0.3 arcsec) as the detector. The resulting
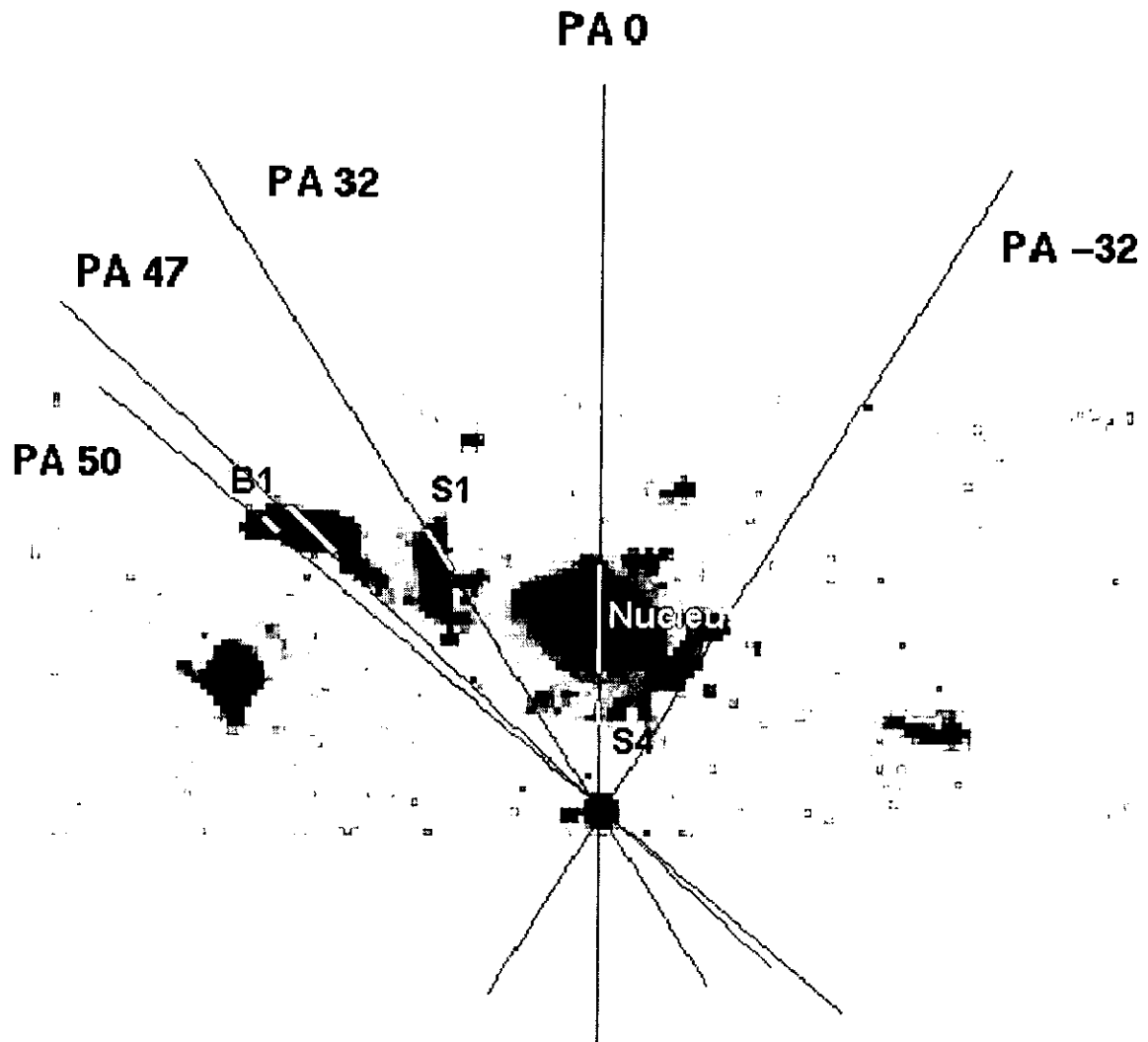
FIGURA 11.1: Hα CCD image of M2-48 taken from Vázquez et al. (2000). The individual regions whose low-resolution spectrum is studied in this paper are indicated
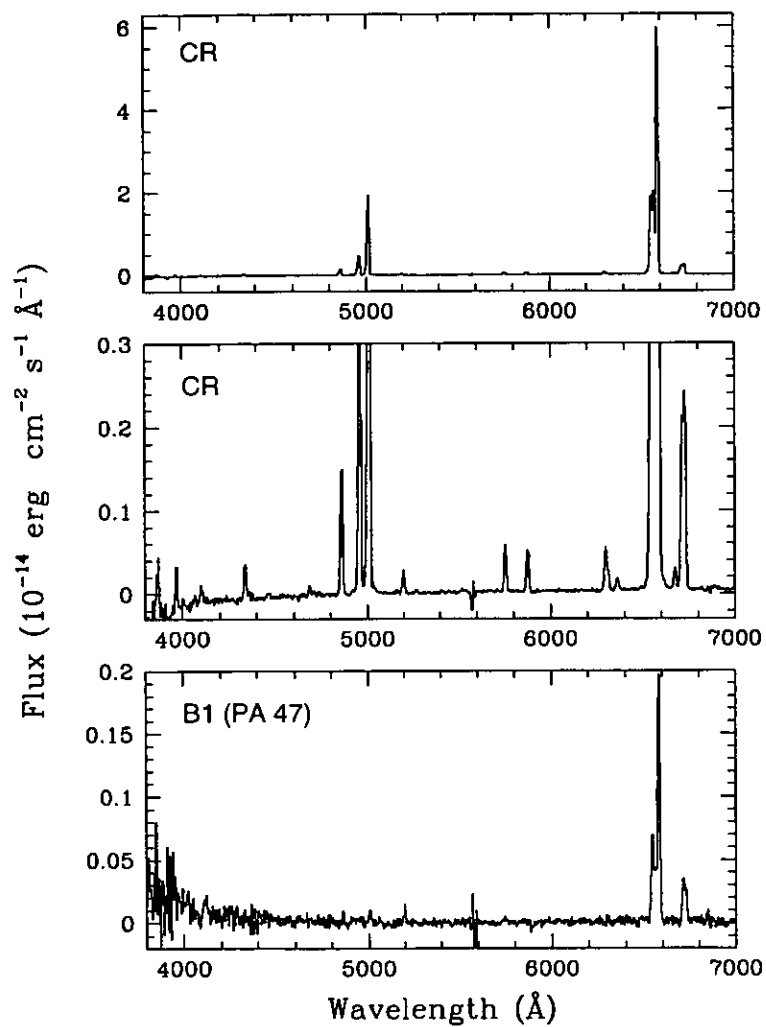
FIGURA 11.2: Optical spectra of two different regions of M 2-48. Top: full scale spectrum of the central region (CR). Middle: expanded scale spectrum of CR showing faint lines. Botom: full scale spectrum of region B1 (PA 47°)
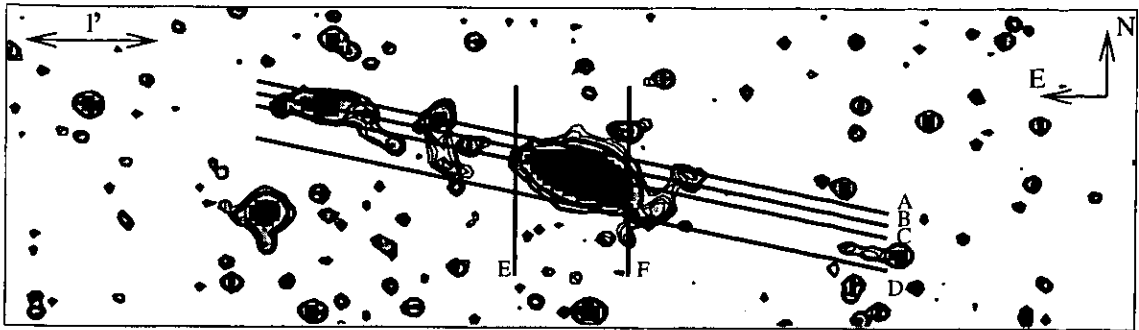
FIGURA 11.3: The long-slit positions slits A-F are marked against a gray-scale representation and contour levels of the [N II] emission of M 2-48.

spectra cover a wavelength range from 3400 to 7500 Å, with a 12 Å spectral resolution. A 220 μm ($\equiv$ 2.9 arcsec) slit width was used. Two exposures of 900 s were taken for each PA. Table 11.1 shows the log of the observations and the region, along the slit, where each 2D image was co-added in order to extract an unidimensional spectrum. Figure 11.1 presents the slit positions overthe Hα emissionimage taken from Paper I. The spectral images were trimmed, bias-substracted, flat-fielded and sky-substracted with standard techniques using IRAF. Flux calibration was performed using sensitivity functions derived from the standard star HD 192281. A panel with some of the unidimensional spectra obtained for different regions is shown in Figure 11.2.

The high-dispersion (HD) spectroscopy was obtained in 1999, June 29 and 30, with the Manchester Echelle Spectrometer (MES; Meaburn et al. 1984) combined with the f/7.9 focus in the 2.1-m OAN telescope. This spectrometer has no cross-dispersion. A 90 Å bandwith filter was used in order to isolate the 87th order, which contains the emission lines Hα and [N II]λλ6548, 6584.

A Tektronix CCD with 1024×1024, 24μm (0.3 arcsec) square pixels was the detector. Two times binning was employed in both spatial and spectral dimensions. The "seeing" varied between 1 and 2 arcsec during the observations. In Figure 11.3, the slit positions A-F are shown against a gray-scale/contour map of a [N II] 6584 image of M 2-48. The 150μm wide ($\equiv$ 10 km s^{-1}) slit was oriented East-West (A-D) and North-South (E-F). Exposure times of 1800 s were carried out for each slit position. The spectra were wavelength calibrated with a Th-Ar lamp to an accuracy of ± 1 km s^{-1}.

An array of [N II] 6584Å position-velocity (PV) maps, formed by the HD spectra (slits A-D), is shown in Figure 11.4. These spectra reveal the complex kinematic structure of the main components of this PN, even finding some features which were not viewed in the
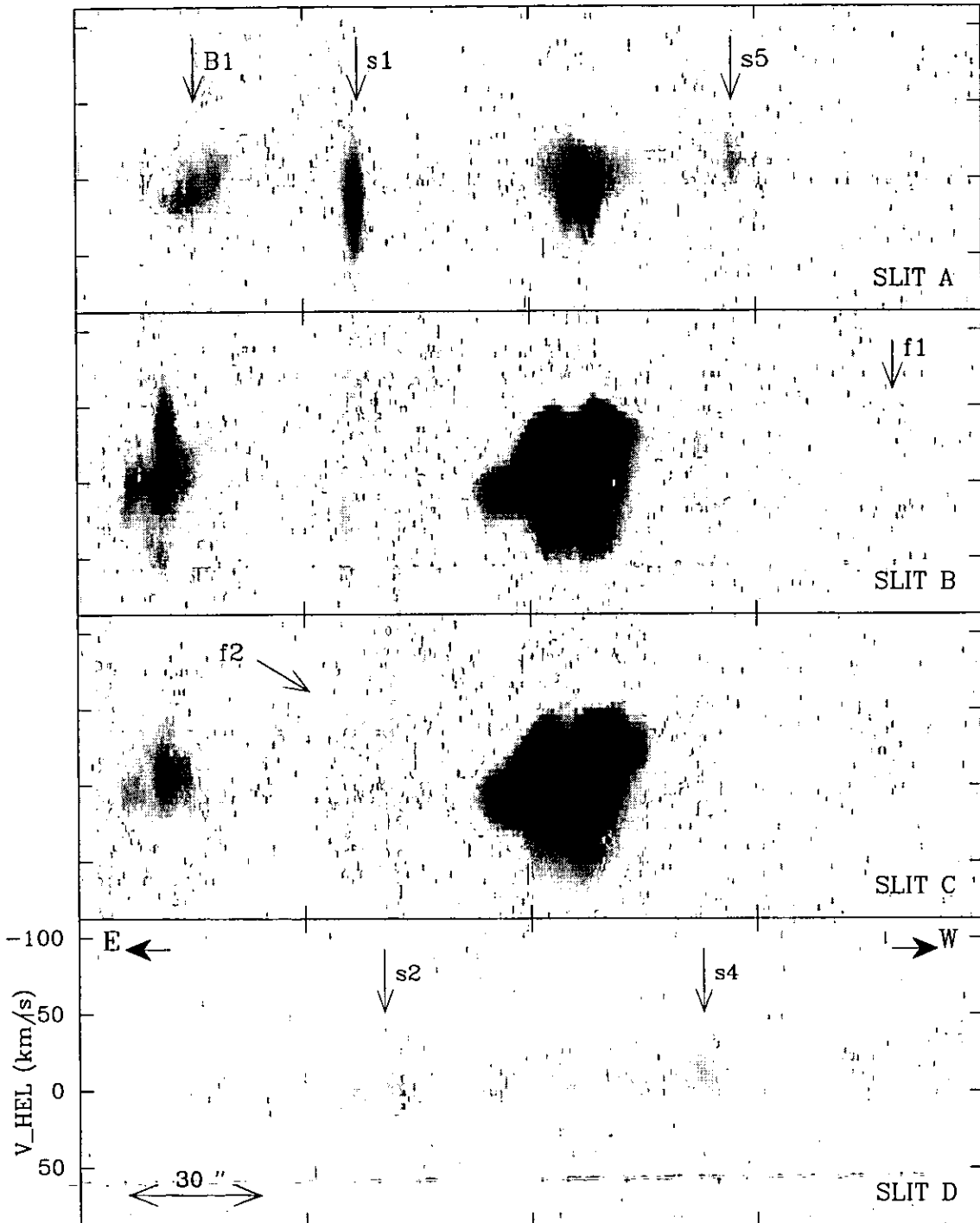
FIGURA 11.4: Gray-scale representation of the position-velocity arrays of [N II] 6584 Å
along slits A-D. The differents features are labeled following Vázquez et. al (2000).

[N II] direct images (Paper I).

In the slit A PV map, the features B1, s1, s5 (see Figure 11.6) and the central region are well indentified, whereas a new feature (f1) is detected in the slit B PV map. This feature is blueshifted and has a decreasing velocity towards the sistemic value with increasing distances from the source. A new feature (f2), spatially coincident with the arc traced by the knots located among s1 and s2 and with a clearly defined blueshift, is apparent in the slit C PV map. Finally, features s2 and s4 are detected close to the sistemic velocity, in the slit D PV map. Enlargements of the main features, using a logarithmic grayscale and contour plot, are presented in Figs. 11.5, 11.6 and 11.7.

11.4 Kinematics and Morphology

The general kinematic structure of the emission lines cannot be explained in terms of a simple perspective effect. The PV arrays of line profiles reveal the complex kinematics of this PN, including an inner bipolar core, two arcs in its surroundings, and the bow-shock B1 to the east of the nucleus.

In Figure 11.3 and in more detail in Figures 11.5 and 11.6 the bright bipolar nebular core appears to be composed of two bipolar lobes. The heliocentric velocity expansion of these bipolar lobes is ranges from ≈ -50 km s^{-1} to 50 km s^{-1}. We can estimate the kinematic age of this bipolar lobes, $\tau_{bipolar} \approx 3 \left[\frac{d}{kpc} \right] \times 10^3$ yr (where d is the distance in kpc).

11.4.1 Arcs and Jet-arc interaction

Several knots around the central bipolar region of M 2-48 have been reported in Paper I. These authors have interpreted these knots as a possible semicircular shell in expansion. We are proposing that they form two slow expanding arcs with heliocentric velocities ranging from ≈ -20 km s^{-1} to 20 km s^{-1}. The east arc is blueshifted and the west one redshifted. We propose that it is not a spherical expanding shell of material because in that case we would expect to observe a complete circular shell arround the bipolar nucleus.

It is possible to estimate the kinematic age of this arcs, $\tau_{arcs} \approx 1.5 \left[\frac{d}{kpc} \right] \times 10^4$ yr. This age is the one expected for a remnant envelope of a AGB progenitor.

Interestingly, we find a feature of high velocity that we are interpreting as an interaction of a high velocity ejection of material with the east arc (this feature was labelled s1 in Paper I), the heliocentric velocity of this feature is ≈ 100 km s^{-1}. This feature, s1, has the characteristics of a bow-shock. In order to study its orientation we compare the observations with a numerical model of this bow-shock. In order to estimate the orientation of the bow-shocks with the sky plane we have used a "3/2-D" model to predict the position-
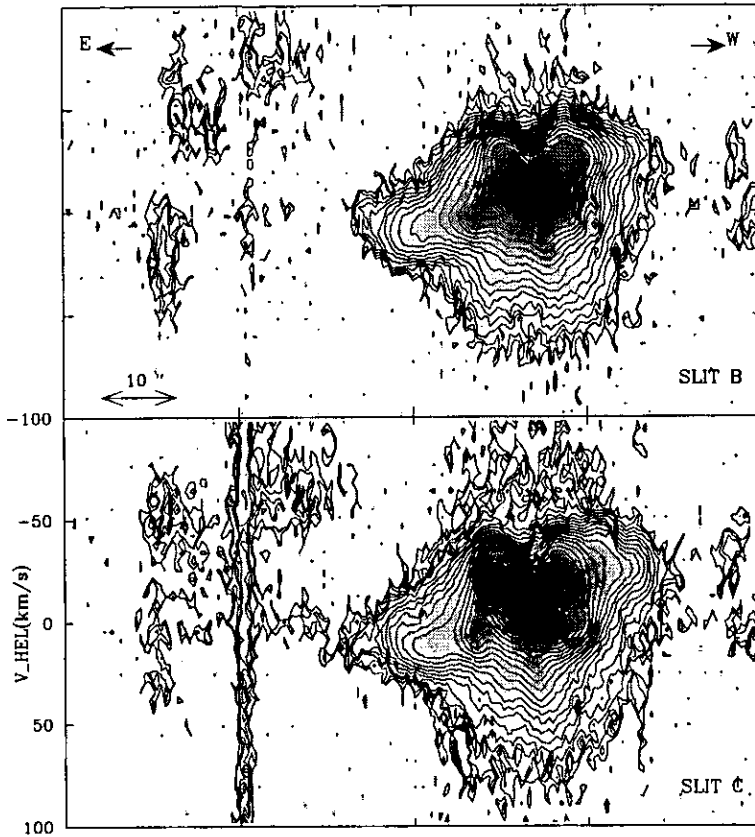
FIGURA 11.5: [N II] 6584 Å PV diagrams of the central region of M 2-48 (for slit positions B and C). The line profiles are shown with a greyscale and with logarithmic contours.

velocity diagram of a bow-shock at different angles with respect to the plane of the sky. In the limit of short cooling distances, the Hα emission can be aproximately modelled with plane-parallel shock calculations. Raga & Noriega-Crespo (1993) found that the Hα emission per unit time and area is approximately given by :

$$I_{H\alpha} \propto (v_{shock})^{\alpha_{H\alpha}} \ . \tag{11.1}$$

The input parameter is essentially the velocity of the shock. This can be estimated from the position-velocity diagrams obtained with the long-slit spectroscopy (Figures 11.4 and 11.7). Raga & Noriega-Crespo (1993) found that there are three values of $\alpha_{H\alpha}$ for differents shock velocitiy ranges. The values used for the bow-shocks B1 and s1 in our models are 2.04 and 3.49, respectivelly.

FIGURA 11.6: [N II] 6584 Å PV diagrams of the bipolar lobes of M 2-48 (for slit positions B and C). The line profiles are shown with a greyscale and with logarithmic contours.

Our model takes into account the shape of the bow-shock. If we assume that the jet is moving over z axis, the shape of the bow-shock can be given by :

$$r \propto z^p,$$ (11.2)

where p determines the aperture of the bow-shock. We find that $p = 2$ fits very well with the observed shape.

With these parameters we can calculate the Hα emission, and predict the position-velocity diagram at differents orientations with respect of the sky plane.

The better fits between the observations and the numerical model are shown in Figure 11.8. From this comparison we can establish that s1 is inclined at an angle $\approx 10^o$ with respect to the plane of the sky.

11.4.2 Bow-shocks B1 and B2

In the [N II] direct images (see Paper I and Figure 11.3), it is possible to see two symmetrical structures with a bow-shock morphology. The east one (B1) is brigther than the west one (B2) and is blueshifted with a heliocentric velocity of ≈ 80 km s^{-1}. The kinematic

Tabla 11.1: Summary of observations.

Region	P.A. (°)	Exposure time (s)	Slit length (arcsec)
CR	0	3600	25.9
S1	32	2400	11.5
S4	0	1800	8.6
B1	47	1800	20.2
B1	50	3000	4.8

information about this bow-shock is shown in Figure 11.7, where we can see the PV diagram in two differents regions of B1 covered by the slits B and C. We can estimate the kinematic age of this bow-shock, knowing the velocity and the distance of the central star, $\tau_{B1} \approx 7.1 \left[\frac{d}{kpc} \right] \times 10^3 \, yr$. We can estimate that B1 is inclined at an angle $\approx -10^o$ and s1 at $\approx 10^o$ with respect to the plane of the sky. This result suggests that the radial velocities of the object can be a factor of ≈ 5 greater than the heliocentric velocities observed in the PV diagrams.

11.4.3   Other features

In Figure 11.4 we can appreciate in the PV diagram of slit B a very weak feature labelled f1. This is a component with an heliocentric velocity of -50km s^{-1}, apparently symmetric to B1. We speculated that this feature could correspond to the western bowshock B2 (see Paper I). In the same Figure but in the PV diagram of slit C, it is possible to see a very strange feature, f2, with a constant heliocentric velocity of -50 km s^{-1}.
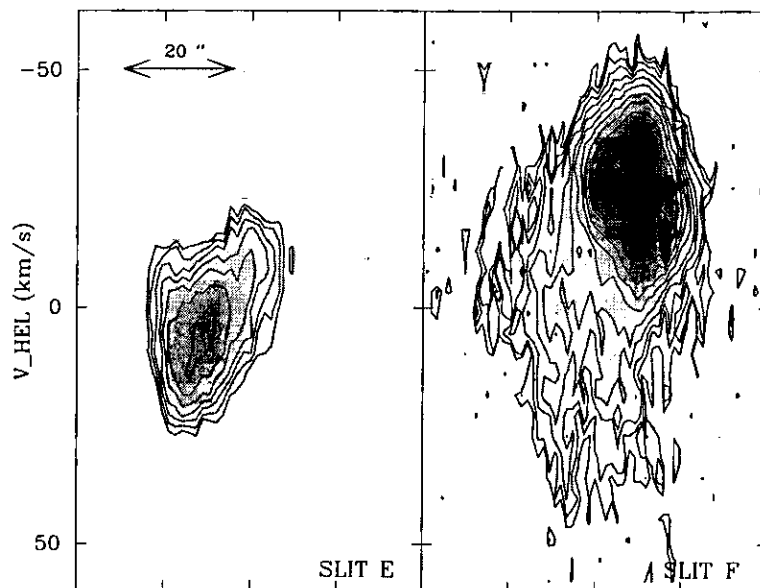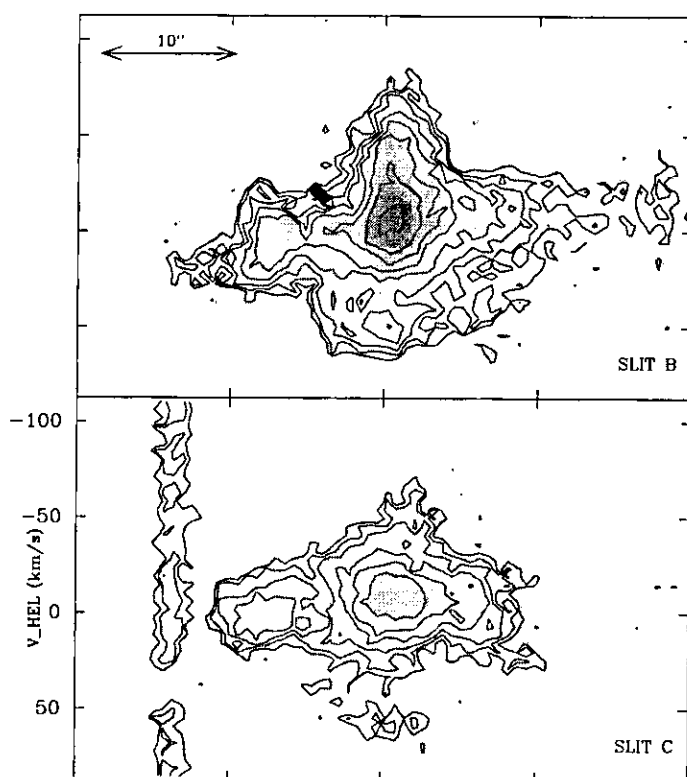
FIGURA 11.7: [N II] 6584 Å PV diagrams of the bow-shock B1 of M 2-48 (for slit positions B and C). The line profiles are shown with a greyscale and with logarithmic contours.
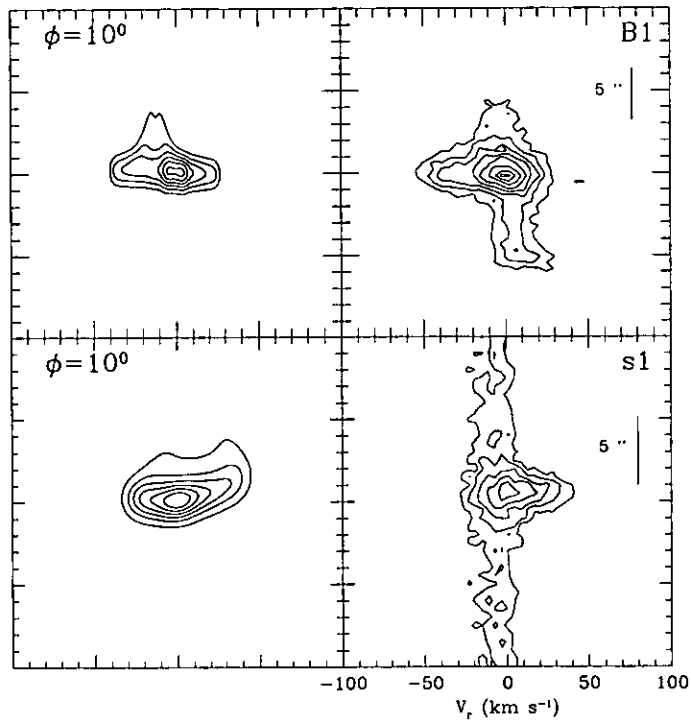
FIGURA 11.8: Comparison of the position-velocity diagram of the features B1 (top right) and s1 (bottom right) and "3/2-D bowshock model fits (top and bottom left, respectively).

TABLA 11.2: Dereddened line intensity ratios.

A - Bright regions

Line	$f(\lambda)$	CR	S1	B1(47°)
3870 He I+[Ne III]	+0.228	107	...	...
3969 H7+[Ne III]	+0.204	51	...	...
4007 [Fe III]	+0.195	9	...	...
4101 Hδ	+0.172	21	...	...
4340 Hγ	+0.129	50	...	...
4363 [O III]	+0.124	9	...	...
4471 He I	+0.095	8	...	...
4686 He II	+0.048	10	...	...
4711 [Ar IV]	+0.036	5	...	...
4740 [Ar IV]	+0.032	3	...	...
4861 Hβ	0.0	100	100	100
4959 [O III]	−0.023	278	...	...
5007 [O III]	−0.024	965	103	172
5152 [Fe III]	−0.064	2	...	...
5198 [N I]	−0.074	15	...	121
5270 [Fe III]	−0.087	2	...	...
5410 He II	−0.116	1	...	...
5755 [N II]	−0.191	16	32	...
5876 He I	−0.216	14	...	...
6300 [O I]+[S III]	−0.285	14	72	...
6364 [O I]	−0.294	4	34	...
6548 [N II]	−0.321	285	214	481
6563 Hα	−0.323	286	275	286
6584 [N II]	−0.326	860	622	1340
6678 He I	−0.338	4	...	...
6717 [S II]	−0.343	29	121	192
6731 [S II]	−0.345	35	95	139
7065 He I	−0.383	4	...	...
7135 [Ar III]	−0.391	25	...	...
7330 [O II]	−0.410	8	...	...
C(Hβ)		1.88	1.82	1.47
I(Hβ)[1]		171	6.0	2.1
N_e([SII])		1260	180	<100
T_e([O III])		10850	...	...
T_e([N II])		10700	20100	...

[1] in units of 10^{-14} erg cm^{-2} s^{-1}.

TABLA 11.3: Chemical abundances in the central region

$12+\log O^+/H^+$	7.85
$12+\log O^{++}/H^+$	8.43
$12+\log O/H$	8.55
$\log N^+/O^+$	+0.30
$12+\log Ne^{++}/H^+$	7.75
$12+\log S^+/^+$	6.16
$12+\log Ar^{++}/H^+$	6.30
$12+\log Ar^{3+}/H^+$	5.77
He^+/H^+ (4471)	0.127
He^+/H^+ (5876)	0.098
He^+/H^+ (6678)	0.096
He^+/H^+ (7065)	0.163
$<He^+/H^+>$	0.100
He^{++}/H^+	0.008
He/H	0.108

11.5   Line intensity ratios and chemical abundances

As it was indicated in section 11.3, five regions were selected from the slit positions observed with low resolution spectroscopy. In Figure 11.2 the flux calibrated spectra of two different zones are shown. The top and middle panels correspond to different scales (high and low intensities respectively) of the spectrum of the central region. The bottom panel corresponds to the spectrum of B1 (AP 47°).

The extinction coefficient, $C(H\beta)$, was derived for three regions: CR, S1 and B1 (AP 47°) from the comparison of observed and theoretical $H\alpha/H\beta$ ratios. We have used the calculations by Storey & Hummer (1995) assuming case B and an iteration procedure adopting finally the electron densities derived for each particular zone and the electron temperature obtained for CR (T_e=10800 K) for all of them. The reddening law of Seaton (1979) have been assumed. Dereddened line intensity ratios with respect to $H\beta$ as well as $C(H\beta)$ of these regions are presented in Table 11.2. The uncertainties in the line fluxes are of the order of 5% for the brightest lines and about 20-30% for the weakest ones. Emission line fluxes of blended lines as $H\alpha$+[NII] nebular lines and the [SII] doublet have
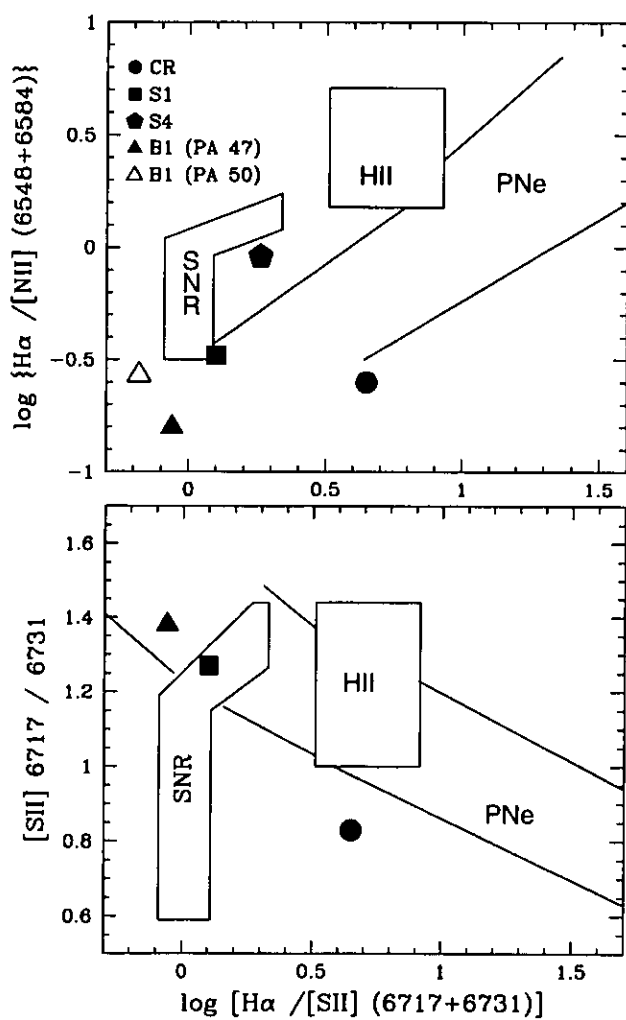
FIGURA 11.9: Diagnostic diagrams showing the emission line ratios of the different regions observed in M 2-48. Top: log Hα/[SII] vs. log Hα/[NII]. Bottom: log Hα/[SII] vs. the electron density indicator [SII] 6717/6731 (adapted from Sabbadin et al. 1977)

been obtained from Gaussian fitting of the line profiles using the Starlink DIPSO package (Howarth & Murray 1990). The dereddened Hβ flux of each region is also included in Table 11.2.

Electron densities and temperatures (see tabla 11.2) have been derived following standard methods of collisionally excited line ratios using the five-level program for the analysis of emission-line nebulae of Shaw & Dufour (1995). There seems to be a gradient in the electron density, which decreases towards the external zones. This is consistent with the expansion of stellar ejecta as the distance towards the nucleus increases. Electron temperatures derived from [OIII] and [NII] lines are almost coincident, indicating that there is not strong temperature stratification in the bright bipolar nebular core of the nebula. The temperature derived for S1 seems too high to be accounted for by pure radiative excitation, this suggest a possible contamination by shocks in this zone, which morphologically resembles a bow-shock (see section 11.4.1).

The spectra of the other two slit positions: S4 and B1 (AP 50°), are so faint that Hβ is not measured and therefore it is not possible to derive the extinction coefficient for these regions. The emission line ratios with respect Hβ and the uncorrected Hα flux for these regions are included in Table 11.2.

We have used several diagnostic diagrams to appreciate the dominant excitation mechanism prevalent in these regions. In figure 11.9 we show two diagrams involving the locus of several line ratios: Hα/[NII], Hα/[SII], and [SII] 6717/6731 for HII regions, PNe and supernova remnants (adapted from Sabbadin et al. 1977). These diagrams indicate clearly that CR is mainly radiatively excited. However, the positions of S1 and B1 are not so definite, in the sense that some shock contribution could be present. The fact that the position of B1 and S1 is just below the locus of the SNRs in Figure Xa could be due to the high N enrichment of the nebula (see below). In Figure 11.10we show a diagram adapted from Philips & Cuesta (1999) involving [OIII]/Hα and [SII]/Hα, this diagram includes the locus of observed emission line ratios for a large number of radiatively excited PNe and predictions of plane-parallel and bow-shock models by Hartigan et al. (1987) and Shull & McKee (1979). The position of the different regions of M 2-48 in this diagram confirms that CR is radiatively excited and that some shock excitation could be contributing to the spectra of S1 and B1. Assuming pure collisional excitation for these zones and comparing their line intensities with the models by Hartigan et al. (1987) we find the best agreement for models with shock velocities of 60 and 130 km s^{-1}, respectively.

Ionic abundances of the central region are shown in Table 11.2 and have been derived using the emission line ratios given in Table 11.2, the code of Shaw & Dufour (1990), and assuming T$_e$ = 10800 K and N$_e$ = 1260 cm^{-3}. To derive the He^{+}/H^{+} and He^{++}/H^{+} ratios we have used the effective recombination coefficients given by Péquignot et al. (1991) for
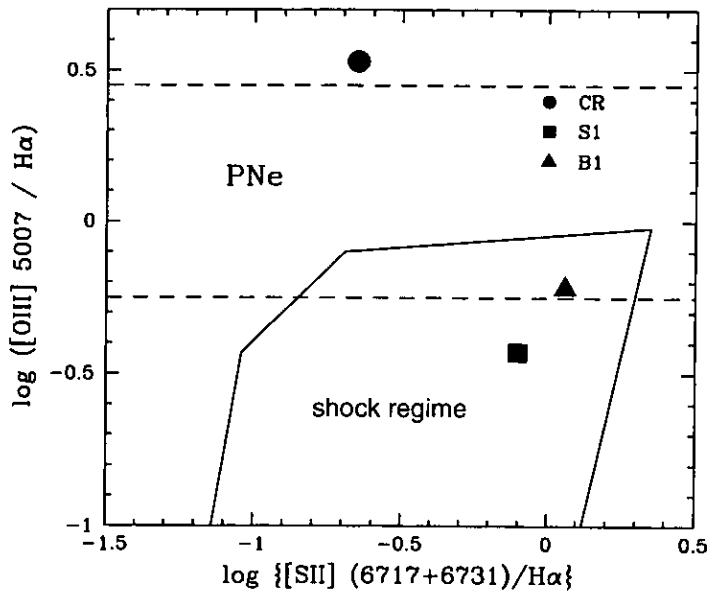
FIGURA   11.10: Diagnostic diagram representing log [SII]/Hα vs. log [OIII]/Hα of the different regions observed in M 2-48 (adapted from Philips & Cuesta 1999)
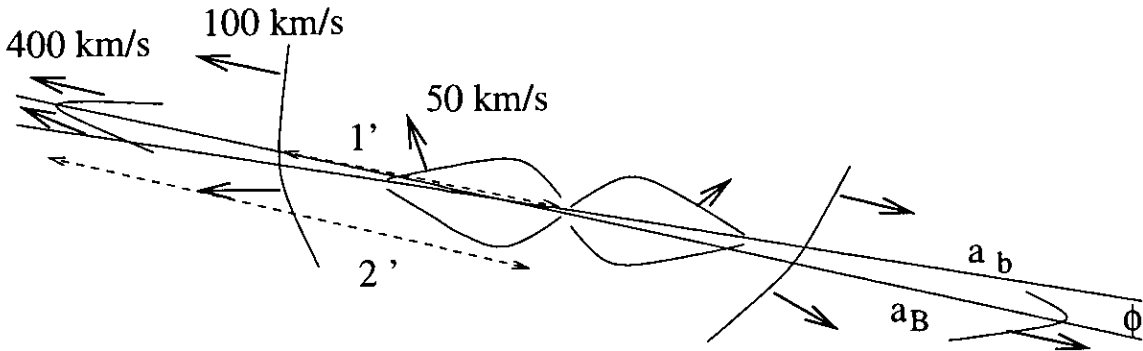
FIGURA 11.11: Structure of M 2-48 with velocities of the main components

all the lines involved. The He^+ abundance from each individual line has been corrected for collisional contribution following Kingdon & Ferland (1995). The finally adopted value of the He^+ abundance is the average of the values obtained for the different individual lines excluding HeI 7065 Å, which suffers for the largest collisional effects.

The total O abundance has been derived from the derived abundance of O^+ and O^{++} combined with the ionization correction factor (ICF) for the presence of O^{3+} proposed by Kingsburgh & Barlow (1994). The total He/H ratio have been obtained simply adding $<He^+/H^+>$ and He^{++}/H^+ ratios.

The log $N^+/O^+=+0.30$ obtained for the nebula clearly indicates that it is a nitrogen-enriched object. Taking into account the chemical classification proposed by Peimbert & Torres-Peimbert (1987) M 2-48 should be classified as a Type I PN (log $N/O \leq -0.30$ and/or He/H $\leq$ 0.125), although it is not a helium-rich object. The O/H ratio is slightly lower than the average of the Galactic Type I PNe (12+log O/H = 8.65, Kingsburgh & Barlow 1994).

11.6   Discussion

Our understanding of the evolution of planetary nebulae has been influenced in the last years by the detection of high-velocity, collimated outflows in these objects. The detection of the bow-shock B1 in M 2-48 is one more case of this kind of outflows. From the kinematic information of the main components of this planetary nebula we have establish a sequence of three differents events, so this object could be add to the list of the nebulae with an episodic, multiple ejection event.

Taking into account the orientation of this bow-shock respect to the sky plane, we can estimate a velocity of 450 km s^{-1}. Interestingly, the line that lies between B1 and B2 (axis

a_B in Figure 11.11) it is not coincident with the axis of symmetry of the bipolar lobes (axis a_b in Figure 11.11). If we also take into account the difference between the kinematical ages of these two ejections, we propose that M 2-48 could have a BRET.

11.7 Conclusions

The bipolar PN M2-48 is studied in this paper via high-resolution long-slit spectroscopy and models of bow-shocks.

- The long-slit spectroscopy reveals a bright central bipolar region with heliocentric velocity of expansion of 50 kms^{-1}.

- We propose that the knots around the bipolar core are forming two slow expanding arcs.

- We interpret the structure s1 as an interaction of an outflow with the east arc.

- We detect a bow-shock, B1, at $\approx 2'$ of the bipolar core. The symmetrical counterpart is only marginally detected.

- Several other features can be seen in the PV diagrams. The complex kinematic behaviour of this object can only be explained in terms of a complex scenario involving several different components.

References

[1] Bryce, M., López, J. A., Holloway, A. J. & Meaburn, J. 1997, ApJ, 487, L161

[2] Cahn, J. H.& Kaler, J. B. 1971, ApJS, 22, 319

[3] García-Segura, G., 1997, ApJ, 489, L189

[4] Hartigan P., Raymond J., Hartmann L., 1987, ApJ, 316, 323

[5] Howarth I.D., Murray J. 1990, SERC Starlink User Note No. 50

[6] Kingdon J.B., Ferland G.J., 1995, ApJ, 442, 714

[7] Kingsburgh R.L., Barlow M.J., 1994, MNRAS, 271, 257

[8] López, J. A., Meaburn, J., Bryce, M & Rodríguez, L. F. 1997, ApJ, 475, 705

[9] López, J. A., Vázquez, R. & Rodríguez, L. F. 1995, ApJ, 455, L63

[10] Meaburn , J., Blundell, B., Carling, R., Gregory, D. E., Keir, D. E. & Wynne, C. G. 1984, MNRAS, 210, 463

[11] Miranda, L. F. & Solf, J. 1992, A&A, 260, 397

[12] O'Connor, J. A., Redman, M. P., Holloway, A. J., Bryce, M., López, J. A. & Meaburn, J. 2000, ApJ, 531, 336

[13] Peimbert M., Torres-Peimbert S., 1987, RMxAA, 14, 540

[14] Péquignot D., Petitjean P., Boisson C., 1991, A&A, 251, 680

[15] Philips J.P., Cuesta L., 1999, AJ, 118, 2919

[16] Raga, A. C. & Noriega-Crespo, A. 1993, RMxAA, 25, 149

[17] Sabbadin F., Minello S., Bianchini A., 1977, A&A 60, 147

[18] Seaton M.J., 1979, MNRAS, 187, 73

[19] Shaw R.A., Dufour R.J., 1995, PASP 107, 896

[20] Shull J.M., McKee C.F., 1979, ApJ 227, 131

[21] Storey P.J., Hummer D.G., 1995, MNRAS, 272, 41

[22] Vázquez, R., López-Martín, L., Miranda, L. F., Esteban, C., Torrelles, J. M., Arias,
      L. & Raga, A. C. 2000, A&A, 357, 1031

Parte IV

Conclusiones

Capítulo 12

Conclusiones

12.1 Introducción

En esta tesis se han analizado problemas relacionados con los fenómenos que pueden causar simetrías, asimetrías y pequeñas estructuras en nebulosas fotoionizadas, así como las eyecciones colimadas que observamos en estas nebulosas. Se ha tratado de entender tanto cual es el origen de ellas como las implicaciones en la morfología y evolución de estos objetos. Este capítulo resume los principales resultados del trabajo, y también se presentan las cuestiones que han quedado abiertas para un estudio futuro.

Desde hace mucho tiempo se han observado en las nebulosas fotoionizadas diversos tipos de estructuras que sugieren, por un lado, que el material no tiene densidad homogénea, y por otro, que hay mecanismos que generan diversos tipos de simetrías (y en muchos casos asimetrías) en las morfologías de estos objetos.

A través del estudio de los nudos cometarios de la nebulosa de la Hélice, así como de la nebulosa planetaria M 2-48 y el objeto Herbig-Haro HH 444 hemos tratado de profundizar en el entendimietno de la formación y evolución de estas estructuras. En las siguientes secciones se resumen los resultados principales que se han obtenido con este trabajo.

12.2 Nudos Cometarios en la nebulosa de la Hélice

Este trabajo propone básicamente que la emisión observada en diversos filtros centrados en longitudes de onda de las líneas de emisión características de las nebulosas planetarias puede ser explicada en términos de dos mecanismos : uno, la fotoionización directa de las cabezas cometarias debida a la radiación estelar incidente, y dos, la fotoionización del material neutro que queda en la sombra de la radiación de la fuente central debida al campo

de radiación difuso nebular. Este mecanismo descarta la idea de que esta emisión pueda
ser gas ionizado arrancado de la cabeza y arrastrado en forma similar al mecanismo de
producción de las colas de los cometas que observamos en el sistema solar.

En el trabajo proponemos un modelo analítico para las cabezas cometarias en donde
suponemos que la emisión procede de un flujo que es fotoevaporado de la superficie del
nudo neutro. Comparando nuestras predicciones con la emisión en la línea de Hα obtenida
por el telescopio espacial *Hubble* podemos calcular el flujo de fotones estelares ionizantes
en las posiciones de diferentes nudos. El valor obtenido para la producción de fotones
ionizantes con este modelo es consistente con otras determinaciones de la luminosidad
de fotones ionizantes de la estrella central. En este trabajo también podemos estimar un
tamaño promedio para los nudos cometarios, $< R_h > = (0.68 \pm 0.07)''$, encontrando además
que no existe ningún tipo de correlación entre el tamaño de estos nudos y su distancia a
la estrella central. Esta posible correlación nos podría dar alguna idea sobre el origen de
los nudos. Es necesario decir que nuestra muestra puede estar sesgada, pues utilizamos 26
nudos (un número pequeño comparado con el total de los que se estima tiene esta nebulosa),
y además se eligieron por ser brillantes y estar aislados para evitar efectos de interacción
con otros nudos que se encuentren próximos. Nuestro modelo de fotoevaporación también
puede predecir las masas de los nudos que son muy consistentes con las masas derivadas
observacionalmente.

En el trabajo también presentamos un modelo analítico en el que las colas cometarias
son el flujo que es fotoevaporado de la región de sombra cilíndrica (a la que no le llega
la radiación estelar ionizante de la fuente central), neutra, que se encuentra detrás de los
glóbulos neutros. Este flujo es fotoevaporado debido a la incidencia del campo de radiación
ionizante difuso nebular. De la misma forma que para las cabezas el modelo permite
predecir y comparar con las observaciones la emisión de las colas para poder cuantificar el
flujo de fotones ionizantes del campo difuso en las posiciones de los nudos.

El modelo permite entonces calcular el cociente de los flujos ionizantes tanto directo
como difuso como función de la distancia a la estrella central. Comparando estos valores de
los cocientes con modelos sencillos del campo difuso ionizante se puede extraer información
de la geometría de la nebulosa. Se llega a la conclusión de que el campo difuso está en los
valores intermedios que corresponden a una geometría esférica y a una de cáscara.

12.3   Chorro neutro embebido en una región H II

En los últimos años se han estado encontrando evidencias observacionales de la existencia de
chorros Herbig-Haro (HH) embebidos en regiones H II. Una vez establecida la existencia
de estos objetos, uno se puede preguntar de manera natural cuáles son las analogías y

diferencias entre los procesos físicos que se están dando en este tipo de objetos y los chorros "normales" HH, en donde sólamente observamos la emisión de una pequeña zona que es ionizada colisionalmente. Este trabajo presenta modelos analíticos y numéricos de un chorro inicialmente neutro que emerge dentro de una nebulosa fotoionizada. El chorro empieza a ionizarse debido a la radiación de la estrella que ioniza la nebulosa. Analizamos los efectos del paso del frente de ionización a través del chorro, y encontramos que la dinámica del gas es muy diferente dependiendo de la naturaleza del frente de ionización. El paso de un frente de ionización rápido tipo-R prácticamente no tiene efectos sobre la dinámica del gas en su paso por el chorro neutro, mientras que el paso de un frente de ionización más lento, tipo-D, sí tiene efectos importantes sobre la estructura y la dinámica del chorro.

Con los parámetros que se encuentran para el objeto HH 444, un chorro que emerge de la estrella variable V 510 Orionis, podemos deducir que el frente de ionización que pasa a través de él es de tipo-R. De esta manera el chorro se irá ionizando progresivamente, y podremos observar regiones más internas del chorro a mayores distancias de la estrella. Si existe algún perfil de velocidad en el material que está emergiendo de la estrella, éste debe ser observado con los perfiles de velocidad a diferentes distancias de la estrella. Para poder verificar la existencia o no de este tipo de perfiles de velocidad se hace necesario un análisis cinemático de este chorro.

12.4 Análisis cinemático del chorro HH 444

Como se vió en el capítulo ??, en los datos espectroscópicos del chorro HH 444 podemos apreciar un gradiente de velocidad al ir aumentando la distancia a la fuente central. Interpretamos este gradiente como un perfil de velocidad en la sección del chorro. Para poder determinar cuál es el perfil de velocidad que mejor reproduce este gradiente observado realizamos unos cálculos numéricos utilizando el codigo tridimensional hidrodinámico "yguazú". De la comparación de los diagramas posición-velocidad observados y los predichos por las simulaciones numéricas encontramos que una velocidad en el centro del chorro de 275 km s^{-1}, con una disminución cuadrática hasta el borde, reproduce bien el gradiente observado.

Ahora bien, encontramos que hay una disminución de la intensidad en Hα al ir alejándonos de la fuente central, y esto es justamente lo contrario de lo que uno esperaría en la ionización gradual de un cilindro de material que se mueve alejándose de la fuente central. Proponemos que este fenómeno es debido a una disminución en la densidad causada por un ángulo de apertura inicial no nulo del haz del chorro.

Si observamos el diagrama posición velocidad de la base del chorro HH 444 vemos que tiene una serie de nudos alineados a lo largo de la dirección de eyección. Nuestra propuesta

es que una variabilidad sinusoidal en la velocidad de eyección del material origina estos nudos. Otra vez comparando las observaciones con las predicciones de las simulaciones numéricas determinamos un período de variabilidad de 100 años, con una amplitud de la variabilidad del 30%.

12.5 Eyecciones colimadas en la nebulosa planetaria M 2-48

Motivados por el interés de encontrar de flujos colimados en nebulosas planetarias, se incluyó en una campaña de observación a la NP M 2-48. Esta NP resultó ser un buen candidato debido a la presencia de una estructura con aspecto de choque de proa situada aproximadamente a 1′ al NE del núcleo bipolar (s1 en Vázquez et al. 2000).

Las observaciones fueron realizadas en el telescopio de 2.1 m del OAN en San Pedro Mártir (Baja California, México) con el PUMA en su modo de imagen directa. El resultado de estas imágenes directas fue el descubrimiento de varias estructuras. En primer lugar se encontró que la estructura s1 no estaba aislada sino que forma parte de una serie de nudos brillantes que parecen formar una cáscara alrededor del núcleo bipolar. Además, se encontraron dos estructuras a unos 2′ simétricas respecto a este núcleo con clara morfología de choque de proa (B1 y B2 en Vázquez et al. 2000). Propusimos que estos choques de proa son originados por un flujo altamente colimado, y además que s1 puede ser el resultado de la interación de este flujo con material eyectado en la etapa AGB.

Resulta necesario hacer un análisis cinemático de estas estructras para poder corroborar nuestras hipótesis. En la siguiente sección listamos las conclusiones obtenidas de este estudio cinemático de la NP M 2-48.

12.6 Análisis cinemático de M 2-48

La nebulosa planetaria M 2-48 ha sido estudiada utilizando espectroscopía de alta resolución y modelos de choques de proa.

La espectroscopía de alta resolución revela la presencia de una región central bipolar con velocidad heliocéntrica de expansión de 50 km s^{-1}. Proponemos que los nudos brillantes que rodean a esta región central bipolar están formando parte de dos arcos en expansión lenta que son un remanente de la etapa AGB. Interpretamos la estructura s1 (ver Vázquez et al. 2000) como una interacción del flujo colimado con uno de estos arcos en expansión.

Se detecta un choque de proa, B1 (ver Vázquez et al. 2000), a unos 2′ al E del núcleo bipolar. La contraparte simétrica de este choque de proa está solo marginalmente detectada. No podemos explicar el complejo comportamiento cinemático de esta nebulosa

planetaria en términos de un esquema sencillo, sino que debemos pensar en una secuencia de eventos que dan lugar a las distintas componentes.

Con las velocidades heliocéntricas obtenidas de la espectroscopía podemos estimar las edades de las diferentes componentes de la nebulosa, y de esta forma, podemos derivar una secuencia temporal de los eventos. Las componentes con mayor edad cinemática son los arcos, que como dijimos, consideramos que son un remanente de la etapa AGB. Después tendría lugar la eyección colimada que da lugar a la formación de los choques de proa. En el paso de este flujo colimado por la posición de los arcos encontramos una traza de su interacción, el nudo s1. Y finalmente, tendría lugar la formación de los lóbulos bipolares. Un detalle interesante es que la línea que une los dos choques de proa no es paralela al eje de simetría de los lóbulos bipolares. Este podría ser un indicio de que estamos ante un BRET. Es decir, que se han producido dos eyecciones colimadas en diferentes instantes y que en el transcurso entre estos dos eventos, el eje de simetría ha variado.

12.7 Trabajo a futuro

En este trabajo de tesis hemos analizado estructuras dentro de nebulosas fotoionizadas, centrándonos en tres objetos: la nebulosa planetaria de la Hélice (NGC 7293), el objeto Herbig-Haro HH 444 y la nebulosa planetaria M 2-48. Evidentemente es necesario analizar una muestra mucho más amplia de objetos, buscando tanto las pequeñas estructuras como los flujos colimados. Este trabajo se podría dividir en dos etapas: en primer lugar, obtener imágenes directas en los filtros usuales de líneas de emisión de la máxima cantidad de objetos posible para reconocer este tipo de estructuras y unirlos a la lista de objetos donde estas estructuras ya han sido encontradas. En segundo lugar, hacer un estudio cinemático detallado de estas estructuras para extraer el máximo de información posible. El apoyo de la comparación con modelos analíticos sencillos y con simulaciones numéricas para los distintos objetos nos ayudará a conocer parámetros nebulares y de las condiciones de la eyección de los flujos colimados.

References

[1] Acker, A., Ochsenbein, F., Stenholm, B., Tylenda, R., Marcout, J. & Schohn, C. 1992, *Strasbourg-ESO Catalogue of Galactic PlanetaryNebulae*, ESO, München

[2] Balick, B., Alexander, J., Hajian, A., Terzian, Y., Perinotto, M. & Patriarchi, P. 1998, *FLIERs and other microstructures in planetary nebulae, IV. Images of elliptical PNs from the Hubble Space Telescope.*, AJ, **116**, 360

[3] Balick, B., Perinotto, M., Maccioni, A., Terzian, Y. & Hajian, A. 1994, *FLIERs and other microstructures in planetary nebulae, II*, ApJ, **424**, 800

[4] Bertoldi, R. & McKee, C. 1990, *The photoevaporation of interstellar clouds. II - Equilibrium cometary clouds*, ApJ, **354**, 735

[5] Bobrowsky, M., Zijlstra, A. A., Grebel, E. K., Tinney, C. G., Te Lintel Hekkert, P., Van de Steene, G. C., Likkel, L. & Bedding, T. R. 1995, *He 3-1475 and its jets*, ApJ, **446**, L89

[6] Böhm, K. H., Raga, A. C. & Solf, J., 1986, *High resolution spectroscopy og Herbig-Haro objects and its interpretation*, IrAJ, **17**, 279

[7] Breitschwerdt, D. & Kahn, F. D. 1990, *Dynamical evolution of planetary nebulae. II - Ionization of shells in planetary nebulae and the formation of low-ionization knots*, M.N.R.A.S., **244**, 521

[8] Bryce, M., López, J. A., Holloway, A. J. & Meaburn, J. 1997, *A Bipolar, Knotty Outflow above 500 Kilometers per Second from the Engraved Hourglass Planetary Nebula M yCn 18*, ApJ, **487**, L161

[9] Burkert, A. & O'Dell, C. R. 1998, *The structure of cometary knots in the Helix nebula*, ApJ, **503**, 792

[39] López, J. A. 1997, *Jets and BRETs in planetary nebulae*, in: Lamers, H. J. G. L. M. & Habing, H. J. (eds) Proc. IAU Symp. 180, Planetary Nebulae. Kluwer, Dordretch, p. 197

[40] López, J. A., Meaburn, J., Bryce, M. & Rodríguez, L. F. 1997, *The kinematics of extensive bipolar lobes and symmetric knots of the planetary nebula KjPn 8 (PK 112-001)*, ApJ, **475**, 705

[41] López, J. A., Vázquez, R. & Rodríguez, L. F. 1995, *The discovery of a bipolar, rotating, episodic jet (BRET) in the planetary nebula KjPn 8*, ApJ, **455**, L63

[42] López, J. A., Meaburn, J. & Palmer, J. 1993, *Kinematical evidence for a rotating, episodic jet in the planetary nebula Fleming 1*, ApJ, **415**, L135

[43] López-Martín, L., Raga, A. C., López, J. A. & Meaburn, J. 2000, *Observations of jets in H II regions (HH 444)*, RMxAC, **9**, 230

[44] López-Martín, L., Raga, A. C., Mellema, G. & Henney, W. J. & Cantó. J. 2001, *Photoevaporating flows from the comatery knots of the Helix nabula (NGC 7293)*, ApJ, in press (10-2-2001)

[45] López-Martín, L., Raga, A. C., López, J. A. & Meaburn, J. 2000, *The structure and kinematics of the HH 444 photoionized jet in the σ Orionis region*, in preparation

[46] López-Martín, L. et al. 2000, *Unvealing the structure of the planetary nebula M 2-48 : Kinematics and physical conditions*, in preparation

[47] López-Martín, L., Raga, A. C., Mellema, G. & Henney, W. J. 1999, *Photoevaporated flow of the cometary knots in NGC 7293*, in: Guenther, E. W., Stecklum, B. & Klose, S. (eds) Optical and Infrared Spectroscopy of Circunstellar Matter. ASP Conf. Ser. Vol. 188, p. 39

[48] Manchado, A., Guerrero, M. A., Stanghellini, L. & Serra-Ricart, M. 1996, *The IAC Morphological Catalog of Northern Galactic Planetary Nebulae*, IAC, La Laguna

[49] Meaburn, J., Clayton, C. A., Bryce, M. & Walsh, J. R. 1996, *The global motions of the cometary knots in the Helix planetary nebula (NGC 7293)*, MNRAS, **281**, L57

[50] Meaburn, J., Clayton, C. A., Bryce, M., Walsh, J. R., Holloway, A. J. & Steffen, W. 1998, *The nature of cometary knots in the Helix planetary nebula (NGC 7293)* MNRAS, **294**, 201

[51] Meaburn, J., Walsh, J. R., Clegg, R. E. S., Walton, N. A., Taylor, D. & Berry, D. S. 1992, *Dust in the neutral globules of the Helix nabula, NGC 7293*, MNRAS, **255**, 177

[52] Meaburn, J., Blundell, B., Carling, R., Gregory, D. E., Keir, D. E. & Wynne, C. G. 1984, , MNRAS, **210**, 463

[53] Meaburn, J. & White, N. J. 1982, *Expanding shells within the Helix nebula (NGC 7293)*, Ap&SS, **82**, 423

[54] Mellema, G., Raga, A. C., Cantó, J., Lundqvist, P., Balick, B., Steffen, W. & Noriega-Crespo, A. 1998, *Photo-evaporation of clumps in planetary nebulae*, A&A, **331**, 335

[55] Miranda, L. F., Vázquez, R., Corradi, R. L. M., Guerrero, M. A., López, J. A. & Torrelles, J. M. 1999, *Detection of collimated outflows in the planetary nebula NGC 6572 shaping its nebular shell*, ApJ, **520**, 741

[56] Miranda, L. F., Guerrero, M. A. & Torrelles, J. M. 1999, *Multiwavelength imaging and long-slit spectroscopy of the planetary nebula NGC 6884 : The discovery of a fast precesing, bipolar collimated outflow*, AJ, **117**, 1421

[57] Miranda, L. F. 1999, *Jets and disks in young planetary nebulae*, in: Guenther, E. W., Stecklum, B. & Klose, S. (eds) Optical and Infrared Spectroscopy of Circunstellar Matter. ASP Conf. Ser. Vol. 188, p. 257

[58] Miranda, L. F. 1995, *The spatio-kinematical structure of the compact planetary nebulae Hu 2-1*, A&A, **304**, 531

[59] Miranda, L. F. & Solf, J. 1992, *Long-slit spectroscopy of the planetary nebulae NGC 6543 - Collimated bipolar ejections from a precessing central source?*, A&A, **260**, 397

[60] Miranda, L. F., Vázquez, R., Corradi, R. L. M., Guerrero, M. A., López, J. A. & Torrelles, J. M. 1999, *Detection of collimated bipolar outflows in the planetary nebulae NGC 6572 shaping its nebular shell*, ApJ, **520**, 714

[61] O'Connor, J. A., Redman, M. P., Holloway, A. J., Bryce, M., López, J. A. & Meaburn, J. 2000, *The Hypersonic, Bipolar, Knotty Outflow from the Engraved Hourglass Planetary Nebula MYCN 18*, ApJ, **531**, 336

[62] O'Dell, C. R. & Bally, 2000, *Outflows, jets and shocks in the Orion nebula*, RMxAC, **9**, 194

[63] O'Dell, C. R. 1998, *Imaging and spectroscopy of the Helix nebula: The ring is actually a disk*, AJ, **116**, 1346

[64] O'Dell, C. R. 1998, *Observational properties of the Orion nebula proplyds*, AJ, **115**, 263

[65] O'Dell, C. R. & Doi, T. 1999, *Calibration of Hubble Space Telescope WFPC2 Emission-Line Filters*, PASP, **111**, 1316

[66] O'Dell, C. R., Hartigan, P., Bally, J. & Morse, J. A. 1997, *High velocity features in the Orion nebula*, AJ, **114**, 2016

[67] O'Dell, C. R. & Handron, D. 1996, *Cometary knots in the Helix nebula*, AJ, **96**, 23

[68] O'Dell, C. R. & Burkert, A. 1997, *The nature of cometary knots in the Helix nebula as determined by HST images*, in IAU Symp. 180, Planetary Nebulae, ed. H. Habing (Dordretch : Reidel), p. 332

[69] Oort, J. H. & Spitzer, L. 1955, *Acceleration of interstellar clouds by O-type stars*, ApJ, **121**, 6

[70] Osterbrock, D. E. 1989, *Astrophysics of Gaseous Nebulae and Active Galactic Nuclei* (Mill Valley : University Science Books)

[71] Peimbert M., Torres-Peimbert S., 1987, *Chemical composition of type I planetary nebulae - Collisional excitation effects on He I line intensities*, RMxAA, **14**, 540

[72] Péquignot D., Petitjean P., Boisson C., 1991, *Total and effective radiative recombination coefficients*, A&A, **251**, 680

[73] Phillips J.P., Cuesta L., 1999, *Density and Excitation Mapping of M2-9*, AJ, **118**, 2919

[74] Raga, A. C., López-Martín, L., Binette, L., López, J. A., Cantó, J., Arthur, S. J., Mellema, G., Steffen, W. & Ferruit, P. 2000, *The emergence of a neutral Herbig-Haro jet into a photoionized nebula*, M.N.R.A.S., **314**, 681

[75] Raga, A. C., López-Martín, L., López, J. A. & Meaburn, J. 2000, *The theory of photoionized jets*, RMxAC, **9**, 191

[76] Raga, A. C., Mellema, G., Arthur, S. J., Binette, L., Ferruit, P. & Steffen, W. 1999, *3D transfer of the diffuse ionizing radiation in interstellar medium flows and the preionization of a Herbig-Haro working surface*, RMxAA, **35**, 123

[77] Raga, A. C. & Noriega-Crespo, A. 1993, *The jet/environment density ratio of stellar jets*, RMxAA, **25**, 149

[78] Rauch, T. 1997, *Implication of light metals (Li-Ca) on NLTE model atmospheres of compact hot stars*, A&A, **320**, 237

[79] Reipurth, B., Bally, J., Fesen, R. A. & Devine, D. 1998, *Protostellar jets irradiated by massive stars*, Nature, **396**, 343

[80] Reyes-Ruiz, M. & López, J. A. 1999, *Accretion disks in pre-planetary nebulae*, ApJ, **524**, 952

[81] Riera, A., García-Lario, P., Manchado, A., Pottasch, S. R. & Raga, A. C. 1995, *IRAS 17423-1755: a massive post-AGB star evolving into the planetary nebulae stage?*, A&A, **302**, 137

[82] Rosado, M., Langarica, R., Cobos, F., Tinoco, S., Garfias, F., Tejada, C., Gutiérrez, L., Le Coarer, E. 1995, *The UNAM Scanning Fabry-Perot Interferometer (puma) for the Study of the Interstellar Medium*, RMxAC, **3**, 263

[83] Rosado, M., Esteban, C., Lefloch, B., Cernicharo, J. & Garciía, R. J. 1999, *The kinematics of the HH 399 jet in the Trifid nebula*, AJ, **118**, 2962

[84] Różyczka, M. & Franco, J. 1996, *Toroidal Magnetic Fields and the evolution of wind-driven nebulae*, ApJ, **469**, L130

[85] Sabbadin F., Minello S., Bianchini A., 1977,*Sharpless 176 : a large, nearby planetary nebula*, A&A, **60**, 147

[86] Sahai, R., Hines, D. C., Kastner, J. H., Weintraub, D. A., Trauger, J. T., Rieke, M. R., Thompson, R. I. & Schneider, G., 1998, *The structure of the prototype bipolar protoplanetary nebula CRL 2688 (Egg nebula): Broadband, polarimetric, and H_2 line imaging with NICMOS on the Hubble SPace Telescope*, ApJ, **492**, L163

[87] Sahai, R., Trauger, J. T., Watson, A. M., Stapelfeldt, K. R., Hester, J. J., Burrows, C. J., Ballister, G. E., Clarke, J. T., Crisp, D., Evans, R. W., Gallagher III, J. S., Griffiths, R. E., Hoessel, J. G., Holtzman, J. A., Mould, J. R., Scowen, P. A. & Westphal, J. A. 1998, *Imaging of the Egg nebula (CRL 2688) with WFPC2/HST: A history of AGB/POST-AGB giant branch mass loss*, ApJ, **493**, 301

[88] Schwarz, H. E. 1992, *M 1-16 - Multiple shocked outflows from an evolved object*, A&A, **264**, L1

[89] Seaton M.J., 1979,*Interstellar extinction in the UV*, MNRAS,**187**, 73

[90] Shaw R.A., Dufour R.J., 1995,*Software for the Analysis of Emission Line Nebulae*, PASP, **107**, 896

[91] Shull J.M., McKee C.F., 1979,*Theoretical models of interstellar shocks. I - Radiative transfer and UV precursors*, ApJ,**227**, 131

[92] Soker, N. & Livio, M. 1989, *Interacting wings and the shaping of planetary nebulae*, ApJ, **339**, 268

[93] Solf, J. 1994, *Long-slit spectroscopy study of the bipolar reflection nebula M 1-92: Detection of compact Herbig-Haro condensations in the lobes*, A&A, **282**, 567

[94] Solf, J., Böhm, K. H. & Raga, A. C., 1986, *Kinematical and hydrodynamical study of the HH 32 complex*, ApJ, **305**, 795

[95] Stanghellini, L., Corradi, R. L. M. & Schwarz, H. E., 1993, *The correlations between planetary nebula morphology and central star evolution*, A&A, **279**, 521

[96] Storey P.J., Hummer D.G., 1995,*Recombination line intensities for hydrogenic ions- IV. Total recombination coefficients and machine-readable tables for Z=1 to 8*, MNRAS,**272**, 41

[97] Tweedy, R. W. & Kwitter, K. B. 1996, *An atlas of ancient planetary nebulae and their interaction within interstellar medium*, ApJS, **107**, 255

[98] Vázquez, R., López-Martín, L., Miranda, L. F., Esteban, C., Torrelles, J. M., Arias, L. & Raga, A.C. 2000, *Bow-shocks and possible jet-shell interaction in the planetary nebula M 2-48*, A&A, **357**, 1031

[99] Vázquez, R., López, J. A., Miranda, L. F., Torrelles, J. M. & Meaburn, J. 1999, *The kinematics of NGC 4361, a Population II planetary nebulae with a bipolar outflow*, MNRAS, **308**, 939

[100] Vorontsov-Velyaminov, B. A. 1968, *Filaments of the Helix nebula*, in Planetary Ne- bulae: IAU Symposium 34, eds. D. E. Osterbrock & C. R. O'Dell (Dordrecht:Reidel), p. 256

[101] Walder, R. & Folini, D. 1998, *Knots, filaments, and turbulence in radiative shocks*, A&A, **330**, L21

[102] Young, K., Cox, P., Huggins, P. J., Forveille, T. & Bachiller, R. 1999, *The molecular envelope of the Helix*, ApJ, **522**, 387

[103] Young, K., Cox, P., Huggins, P. J., Forveille, T. & Bachiller, R. 1997, *Neutral atomic carbon in the globules of the Helix nebula*, ApJ, **482**, L101

[104] Zucker, D. B. & Soker, N. 1993, *The morphology and interaction with the interstellar medium of the planetary nebulae IC 4593*, ApJ, **408**, 579

Apéndice A

Glosario de Abreviaturas

- **AGB** Rama asintótica de las gigantes
- **BRET** Chorro episódico, rotante y bipolar
- **FI** Frente de ionización
- **FLIER** Región rápida de emisión de baja ionización
- **HH** Herbig-Haro
- **HST** Telescopio espacial Hubble
- **IRAF** *Image Reduction and Analysis Facility*
- **MES** Espectrómetro *echelle* de Manchester
- **NC** Nudo Cometario
- **NP** Nebulosa Planetaria
- **OAN** Observatorio Astronómico Nacional
- **PV** Posición-velocidad
- **RT** Rayleigh-Taylor
- **SP** Simetría puntual
- **UNAM** Universidad Nacional Autónoma de México
- **YSO** Objetos estelares jóvenes